ALMA MATER STUDIORUM · UNIVERSITÀ DI BOLOGNA

Covalent modification of graphene oxide: water remediation and carbocatalysis

Presentata da: Sebastiano Mantovani

Coordinatore Dottorato:
Matteo Calvaresi

Supervisore
Manuela Melucci
Co-Supervisore
Matteo Calvaresi

Esame finale anno 2024

Contents

1. Abstract

The main objective of this thesis is the application of new materials derived from the functionalization of graphene oxide in the fields of water remediation and CO_2 utilization.

Chapter 4.1 reports the synthesis and characterization of the graphene oxide modified with branched cationic polyethyleneimine (GOPEI) material. This polymer was then functionalized with a thiophene-based fluorescent dye to better monitor its purification through UV-vis spectroscopy. This process also allowed for a better understanding of the mechanisms underlying purification by microfiltration. By studying adsorption isotherms and formulating theoretical models, the kinetics, efficiency, and adsorption mechanism of GOPEI towards two water pollutants, arsenic and lead, were discussed.

Chapter 4.2 presents the study of the adsorption properties of a family of graphene oxide-based composites, covalently modified with three amino acids: L-Lysine, L-glutamic acid, and L-methionine (GO-Lys, GO-Glu, and GO-Met). Along with synthesis, the purification protocol was also improved to be faster and more efficient than previously reported, and their complete characterization was performed through XPS analysis. Finally, these materials were used as adsorbents towards a mixture of selected contaminants including pharmaceuticals, polymer additives, and dyes. Their performance towards these pollutants was evaluated through adsorption isotherms and dedicated molecular dynamics simulations.

Finally, in Chapter 4.3, a new synthesis of a graphene oxide-arginine composite (GO-Arg) and its utilization in carbon capture and utilization processes was reported. In the first part, the efficacy of this composite in CO_2 fixation through the selective opening of epoxides to cyclic carbonates was demonstrated. The reported protocol was found to be applicable to a wide range of substrates (fifteen examples), and its reusability was tested for up to 5 cycles. In the second part, the application of this material in an ICCC (Integrated CO_2 Capture and Conversion) process was focused on. It was shown that the material is capable of capturing CO_2 from both high-purity atmospheres and low-concentration mixtures (such as the atmosphere) and converting it when exposed to dedicated reaction conditions (i.e., synthesis of cyclic carbonates). The entire process was thoroughly studied and rationalized through dedicated computational and spectroscopic analyses (XPS, BET, TGA, etc.).

1

2. Introduction

2.1 Graphene Oxide

Graphene oxide **(GO)** is a remarkable two-dimensional (2D) material obtained by introducing multiple oxygen functionalities into the original graphene structure. These oxygen atoms form covalent bonds with carbon atoms, transitioning them from the sp^2-hybridized state to the sp^3-hybridized state. In GO, the number of carbon atoms bonded to oxygen surpasses the count of intact sp^2-hybridized carbon atoms. As a result, GO exhibits distinct characteristics that set it apart from its parent graphene counterpart.

Prior to the discovery of graphene in the 2004, the initial documentation of graphene oxide formation dates back to 1855 when Brodie published a concise note in French within the pages of Annales de Chimie [1]. In this paper, Brodie successfully oxidized graphite by introducing concentrated sulfuric acid to a mixture of graphite and $KClO_3$. The subsequent addition of water caused the solid to disintegrate and significantly increase in volume. When the dried product was calcinated, it yielded graphite that was tainted with sulfates and chlorates. Towards the end of his concise paper, Brodie briefly mentioned nitric acid and bichromate as alternative oxidizing agents.

In 1859, Brodie further elucidated the preparation technique, known today as the "Brodie method," involving the reaction of graphite with potassium chlorate in fuming nitric acid. This comprehensive account of the compound's composition and chemical properties, titled "On the atomic weight of graphite", was presented in the Philosophical Transactions of the Royal Society of London [2]. Interestingly, the titles of both papers did not provide any indication of a novel carbon compound and Brodie did not reference his first work in the his second paper. In 1865, Gottschalk reproduced and verified Brodie's findings, introducing the term "graphitic acid" for the first time in his publication [3].
GO gained significant attention after Berthelot's 1870 publication [4], which provided new insight on Brodie's GO preparation method as a means to different forms of graphitic carbon.

Since then, numerous attempts have been made to substitute the employed reagents, such as fuming nitric acid, concentrated sulfuric acid, and potassium chlorate, with safer

and more practical oxidizing agents [5] [6] [7]. Despite numerous approaches, currently only two methods hold significance: the techniques outlined by Staudenmaier [8] and Hummers and Offeman [9], respectively. Hummers and Offeman successfully implemented permanganate as an oxidant for the production of GO. Their method involved suspending powdered graphite flakes and solid sodium nitrate in concentrated sulfuric acid, followed by the gradual addition of permanganate, water and lastly hydrogen peroxide to eliminate the unreacted permanganate.

In the course of GO research history, the composition of GO has been determined through combustion analysis to assess the carbon and hydrogen contents. The oxygen content was then derived by subtracting the sum from 100%. However, it was widely acknowledged that complete reduction was challenging even under rigorous conditions (e.g., temperatures up to 800 °C). To obtain an accurate C/O ratio, adjustments had to be made to account for the residual ash resulting from combustion. Another significant challenge in determining the precise C/O ratio arises from the presence of residual hydration water in the sample, which necessitates careful drying methods to minimize the risk of deterioration.

Brodie's original findings indicated a carbon content of 60% and a hydrogen content range of 1.75-1.91%. Over the course of GO research, samples prepared using this method have exhibited relatively consistent carbon and hydrogen contents. These values have remained relatively stable throughout a deep investigation of GO. Hummers and Offeman reported a carbon content of 47% for their product and a carbon content of 52% for the sample prepared according to the "Staudenmaier method".
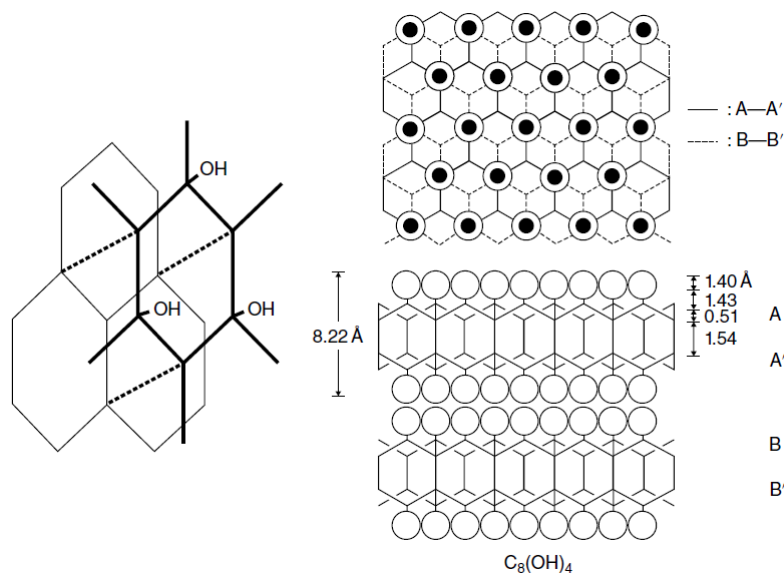

Figure 2.1: The structural models of Thiele (left [10]) and Nakajima et al. (right [11]).

3

In 1930, Thiele proposed a structural model for GO based on his analytical findings [10]. He suggested that oxygen was bonded to the carbon framework in the form of hydroxyl (-OH) groups. Given the honeycomb arrangement of carbon atoms, Thiele formulated a sum formula of $C_6O_3H_3$. To align with this sum formula, Thiele postulated that the -OH functional groups were covalently attached to every other carbon atom on both sides of a carbon bilayer, which were interconnected by covalent C-C bonds (Fig. 2.1, left).

Almost 60 years after Thiele, Nakajima et al. presented a very similar structural model of GO (Fig. 2.1, right), without giving any reference to Thiele's paper [11] [12]. In these articles, the authors proposed an alternative sum formula ($C_8(OH)_4$) instead of the previously suggested $C_6(OH)_3$. Their model drew inspiration from the resemblance of X-ray diffraction (XRD) data to those of a carbon fluoride compound sharing the same composition. However, neither of these models garnered significant attention within the research community.

In 1928, a new chapter in GO research began when Hofmann took the lead [13] [14], later joined by Frenzel in 1930 [7]. They utilized powder X-ray diffraction (XRD) to delve into the properties of GO. Building upon their investigations and chemical insights, Hofmann and his team proposed the first widely accepted structural model for GO. The construction of the model began with the following considerations. Each carbon hexagon could have at maximum all three double bonds replaced by oxygen atoms, forming epoxide units that bridged two adjacent carbon atoms. However, given the commonly observed C/O ratio of 3, it was evident that some double bonds remained unoxidized in the structure. This evidence was considered as a hint for the presence of epoxide functions in GO. In 1947, Ruess published a paper highlighting how GO exhibits less reactivity compared to organic epoxides. For instance, it does not undergo the typical ring-opening reactions observed with ammonia, HBr, or HCl, which results in the formation of vicinal hydroxyamines or halogenohydroxides. Additionally, Ruess raised doubts about the notion that hydroxyl groups could be formed through hydrolysis of the epoxide functions. Building upon these chemical arguments and re-evaluating the X-ray diffraction (XRD) data of both Hofmann et al. and his own, Ruess presented a new structural model. In this model, he proposed a reconsideration of the covalent bonding between hydroxyl groups and the carbon framework of GO (Fig. 2.2).
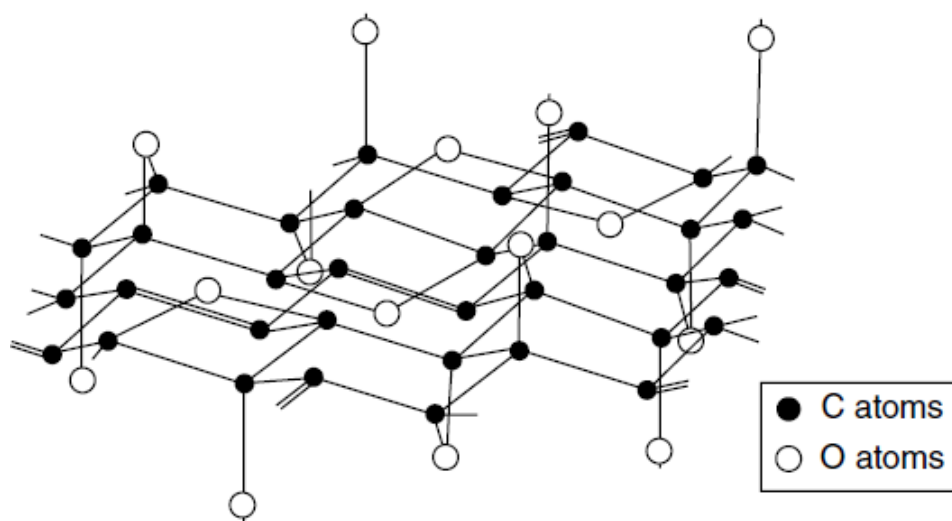
Figure 2.2: The structural GO model according to Ruess.

A new phase of GO research started in 1989-1991, when Mermoux et al. applied magic angle spinning nuclear magnetic resonance (MAS NMR) to ^{13}C. The ^{13}C NMR spectrum displayed three prominent signals at chemical shifts of 60, 70, and approximately 130 ppm. In their analysis, Mermoux et al. attributed these three signals to ether functions, alcohol functions, and aromatic or conjugated double bonds, respectively. Consequently, they changed the previously proposed structural model. While Mermoux and Chabre initially assigned the 60 ppm signal to epoxide functions in their first publication [15], they later combined epoxide (1,2-ether) and 1,3-ether functions in their subsequent paper [16] and considered their findings as supporting Hofmann et al.'s and Ruess's models. In the revised model, it was proposed that a portion of the epoxide groups in GO were substituted by tertiary hydroxyl groups. These two functional groups were distributed somewhat randomly across both sides of the carbon grid. The signal at 130 ppm in the NMR spectrum could be attributed to aromatic carbon atoms, indicating the presence of patches of aromatic rings of varying sizes scattered among the oxygen-containing regions. These aromatic regions, along with the epoxide groups, contribute to maintaining the carbon grid in an almost flat configuration. However, slight deviations from flatness may arise due to the presence of sp^3-hybridized carbon atoms carrying the OH groups. More information about the history of this material, its structure and reactivity can be found in the book "Graphene Oxide" published by A. M. Dimiev and S. Eigler in 2017 [17].

To this date the most recognized structure is the Lerf–Klinowski model [18], in which GO presents different reactive oxygen-bearing functional groups, such as hydroxyl functions and epoxide groups on the basal plane, while carboxyl, carbonyl, phenol, lactone and quinone groups are mainly localized at the edges. Fig.2.3 illustrates a sketch representation

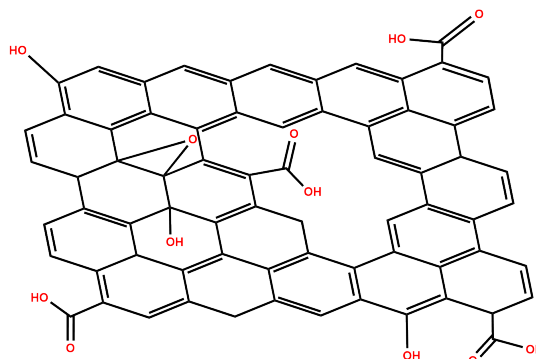of the commonly accepted structure that is widely employed today.

Figure 2.3: Representative chemical structure of a GO nanosheet.

Graphene oxide remained a mere laboratory curiosity [19] until the groundbreaking discovery of graphene by Geim and Novoselov [20]. Following this remarkable breakthrough, the simple reduction of graphene oxide emerged as an economical approach to obtain graphene layers. This concept ignited a surge of research focused on GO, and its exploration continues to thrive until the present day.

2.2 Chemical modification of Graphene Oxide

Chemical modification of GO has emerged as a pivotal strategy with the potential to revolutionize material properties, consequently opening up a plethora of innovative applications. This transformative approach spans across a multitude of fields, with notable contributions in groundbreaking advancements in nanomedicine [21], sustainable energy solutions [22], advanced polymer composites [23], ultra-sensitive sensing technologies [24], cutting-edge filtration systems [25], catalytic processes, and environmental remediation [26].

The various oxygen-based groups found in GO, including hydroxyls, epoxides, and carboxylic acids, offer numerous options for modifying GO. In theory, established organic chemistry methods should work to target these different functional groups. However, when dealing with GO, it is not as straightforward. It was observed that it is not always just one specific functional group reacting but a mixture of them. This complexity, further enhanced by the heterogeneous nature of GO, calls for a thorough discussion of GO's chemistry and reactivity.

2.2.1 Functionalization of Epoxide groups

The majority of functional groups located on the basal plane of a typical sheet of GO are hydroxyl and epoxy groups. The epoxy can be functionalized through a nucleophilic ring-opening reaction (Scheme 2.1). The opening of the epoxy ring can be done with amino terminated molecules [27], thiols [28] and the azide anion (N^{3-}) [29].

One striking advantage of this approach is its remarkable ease of implementation, even at room temperature and in aqueous environment. Consequently, this method has garnered considerable attention and acclaim for its potential to enable large-scale production of functionalized graphene materials.
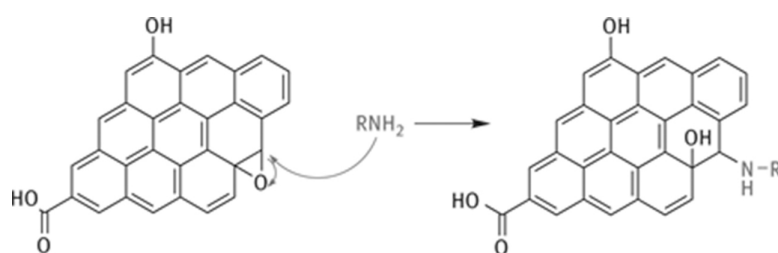
Scheme 2.1: Mechanism of the opening of epoxide with a nucleophile.

Vacchi et al. reported the study of a reaction between GO and amine functions occurring via ring opening of the epoxides using magic angle spinning (MAS) solid-state NMR [27]. They observed that the reaction between GO and tert-butyloxycarbonyl (BOC) mono-protected triethylene glycol (TEG) diamine predominantly involves the epoxy functional groups via ring-opening reactions, rather than the carboxylic acids, which are present in relatively small quantities. The ^{13}C-NMR and ^{1}H–^{13}C correlation spectra reported showed that, after functionalization, the peak of the epoxy groups (60 ppm) was decreased in intensity (Fig. 2.4).
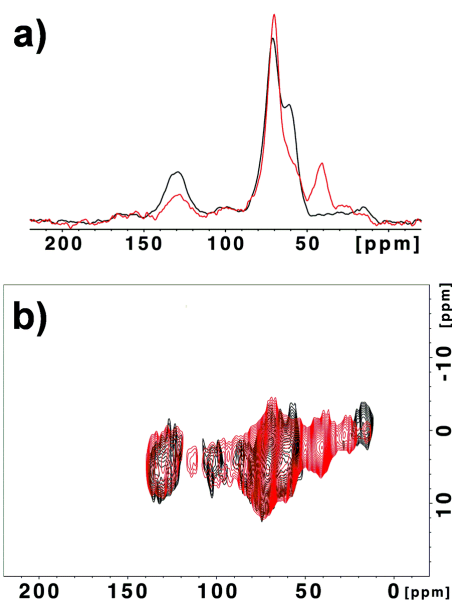
Figure 2.4: ^{13}C-NMR **(a)** and ^{1}H–^{13}C correlation **(b)** spectra of before (black) and after (red) functionalization with Boc mono-protected triethylene glycol (TEG) diamine.

Hsiao et al. studied the covalent functionalization of graphene with Poly(oxyalkylene) amines maleic acids (MA-POA2000) by two different methods [30]. The first method involved typical free radical grafting while the second was the direct reaction of molecules with the epoxy groups on graphene (Scheme 2.2). The materials obtained with the two different methods were characterized by transmission electron microscopy (TEM), X-Ray Photoelectron Spectroscopy (XPS), Raman spectroscopy and Thermo gravimetric Analysis (TGA). With the characterization they demonstrated that the functionalization of graphene oxide through epoxy ring opening can produce a functionalized graphene with good solvability in, and compatibility with, an organic solvent. Compared to the free-radical grafting method, after direct covalent functionalization, the second method provides greater thermal stability for the material.
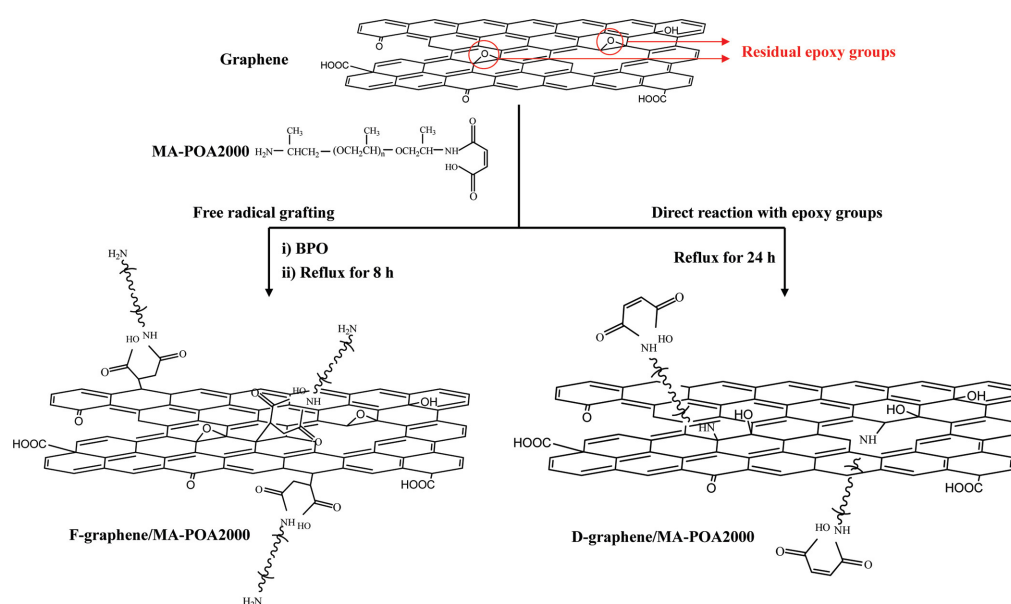
Scheme 2.2: The Preparation of F-Graphene/MA-POA2000 and D-Graphene/MA-POA2000. Figure taken from [30].

Yang et al reported a facile method to obtain polydisperse chemically-converted graphene (p-CCG) sheets that were covalently functionalized with ionic liquid [31]. The results from characterizations indicated that the ionic liquid units were coupled to the surface of the graphene nanosheets successfully, and that exfoliation of the layered graphene was successful (Scheme 2.3).
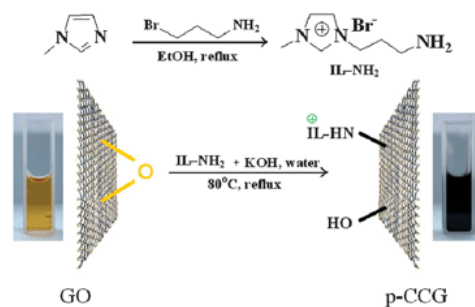
Scheme 2.3: Illustration of the preparation of p-CCG. Figure taken from [31].

Additionally, the p-CCG nanosheets, without any assistance from polymeric or surfactant stabilizers, could be dispersed well in water, DMF, and DMSO, due to an enhanced solubility and electrostatic inter-sheet repulsion provided by the ionic liquid units. They reported that dispersions of p-CCG were stable for more than three months.

9

2.2.2 Functionalization of Carboxylic Acids

The carboxylic acids of GO are located mainly at the edges. These functional groups can react with amines to form amides or with alcohols and phenols to form esters. The amidation reaction on the carboxylic acid groups of GO can be performed in harsh or mild conditions (Scheme 2.4). In the first case, an activating agent can be used, such as thionyl or oxalyl chloride, to achieve an acyl chloride that can later react with an amine or an alcohol to yield an amide or an ester.
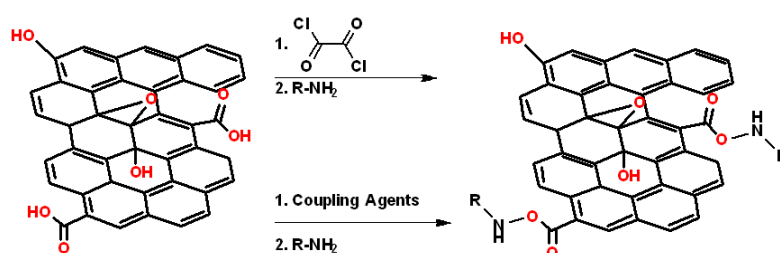
Scheme 2.4. Representative sketch of the amidation reaction.

In the second case, several coupling agents could be employed, like N,N'- dicyclohexyl-carbodiimide (DCC) or 1-ethyl-3-(3-dimethylaminopropyl)carbodiimide (EDC), hydroxy-benzotriazole (HOBt) and 2-(7-aza-1H-benzotriazole-1-yl)- 1, 1, 3, 3-tetramethyluronium hexafluorophosphate (HATU). The difference between the two strategies lies in the selectivity of the methods of choice. Thionyl or oxalyl chlorides are not selective and they could react with the hydroxyl groups too, causing side reactions.

Zhang et al. reported the graphene–C_{60} hybrid material via a simple coupling reaction between GO and pyrrolidine fullerene [32]. GO was activated by $SOCl_2$ to achive the corresponding acyl-chloride functionalized GO. Subsequently, the hybrid was obtained through a condensation reaction between pyrrolidine fullerene and the acyl-chloride functionalized GO (Scheme 2.5). Through XPS and thermo-gravimetric analysis they were able to confirm the functionalization. Based on the atomic ratio of C to N determined by XPS in the graphene-C_{60}, they estimated that, for every 130 atoms in the graphene–C_{60}, one molecule of C_{60} is present.
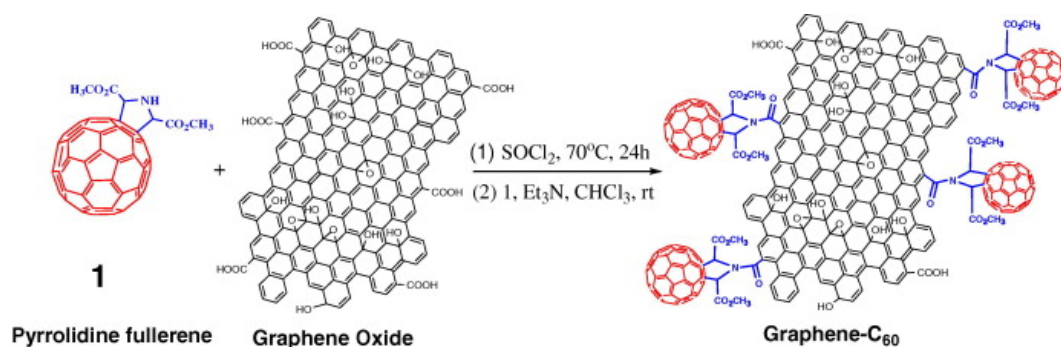
Scheme 2.5: Synthesis procedure of the graphene–C$_{60}$ hybrid material. Reproduced from [32].

Xu et al. proposed the first *organic-solution-processable* functionalized-graphene (SPF-Graphene) hybrid material with 5-4(aminophenyl)-10, 15, 20-triphenyl porphyrin (called TPP-NHCO-SPFGraphene), and its photophysical properties including optical-limiting properties [33]. This nanohybrid was obtained by binding GO with the porphyrin via an amide bond. The reaction was carried out using an amine-functionalized porphyrin (TPP-NH$_2$) and GO, previously activated with thionyl chloride, in DMF. The hybrid was characterized by atomic force microscopy (AFM), TGA, X-ray diffraction (XRD), and UV-vis spectroscopy. The grafting of porphyr in material was confirmed by FTIR spectroscopy. In the spectrum of TPP-NHCO-SPFGraphene the peak at 1730 cm^{-1} almost disappears, and a new broad band emerges at 1640 cm^{-1}, which corresponds to the C=O characteristic stretching band of the amide group.

With fluorescence spectroscopy they observed a 56% quenching of fluorescence by TPP-NHCO-SPFGraphene compared to the pristine TPP-NH$_2$. This decrease in luminescence was then ascribed to a charge transfer from the photoexcited singlet state TPP-NH$_2$ to the graphene moiety. Since the material demonstrated efficient energy transfer, they subsequently investigated its optical limiting performance with a measure of Z-scan. They found out that TPP-NHCO-SPFGraphene demonstrates much better optical limiting properties compared with the benchmark material (C$_{60}$), the control sample, and the individual components.

Liu et al. reported functionalized nanographene oxide (NGO) with branched polyethylene glycol (PEG) to obtain a biocompatible NGO-PEG conjugate stable in various biological solutions, and used them for attaching hydrophobic aromatic molecules non covalently via $\pi - \pi$ stacking [34]. The resulting complex exhibited excellent water solubility while maintaining its high cancer cell killing potency similar to that of the free topoisomerase inhibitor molecules in organic solvents. The efficacy of complex was far higher than that FDA-approved water soluble prodrug used for the treatment of colon cancer.

2.2.3 Functionalization of Hydroxyl groups

Although hydroxy groups are not particularly reactive nucleophiles or electrophiles, they can still participate in many chemical reactions. The most common method to functionalize GO through the hydroxy functions is silanization (Scheme 2.6), which involves the reaction with organosilanes to form covalent Si–O bonds. This reaction is widely used to functionalize mineral components, such as glass and metal oxide surfaces, with many applications in coatings and material science.
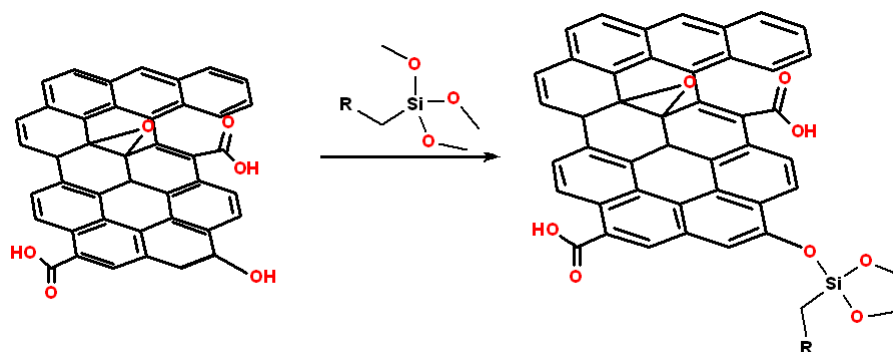
Scheme 2.6: Representative sketch of the silanation reaction.

Jie Xu et al. reported one-step synthesis of ionic liquid (i.e. 1-(trimethoxysilyl)propyl-3-methylimidazolium chloride) immobilized GO (GO-[SmIm]X) via the reaction of GO and functionalized imidazolium-based ionic liquid [35]. GO materials were directly grafted with functionalized imidazolium-based ionic liquid with different halides via the covalent condensation between alcoholic C-OH of GO and alkoxyl groups of oxysilanes in ionic liquids. The materials were tested as potential catalyst for the solvent free cycloaddition of CO_2 with propylene oxide (PO). They demonstrated these, under optimal reaction conditions with this materials, the PO yields obtained was 95.9%. They also reported that various cycloaddition reactions using other cyclic epoxides could be selectively catalysed by GO-[SmIm]X.

Carpio et al. presented a study evaluating for the first time the antimicrobial activity of GO silanized with N-(trimethoxysilylpropyl) ethylenediamine triacetic acid (GO–EDTA) against Gram-negative and Gram-positive bacteria, as well as its cytotoxicity to human corneal epithelial cell line hTCEpi [36]. Most importantly, they reported that GO–EDTA did not present any cytotoxicity to human corneal epithelial cells as more than 99% of the cells were still alive after exposure to the nanomaterials for 24 h. This work also evaluated the material adsorption capacity for two heavy metals, Cu^{2+} and Pb^{2+} at different concentrations, varying pH and contact time. Lastly, they also evaluated the maximum adsorption capacity of the GO–EDTA toward these heavy metals.

Other reactions can also be used for the derivatization of the hydroxy functions of GO. For instance, boronic acids are highly reactive towards 1,2-diols and 1,3-diols (Scheme 2.7). This reaction occurs under slightly alkaline conditions and forms cyclic boronic esters [37]. Alternatively, the reaction can be performed by heating (80–120 °C) to avoid using an alkaline solution, but might lead to partial reduction of GO [38] [39].
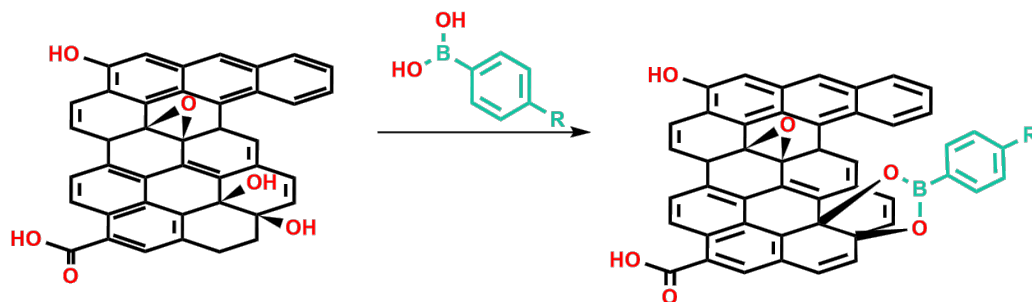
Scheme 2.7: Representative sketch of esterification with boronic acid derivatives.

2.3 Characterization of modified GO

2.3.1 Infrared Spectroscopy

The principles of infrared spectroscopy (IR) are well known, and thus they do not require a long introduction. IR spectroscopy is based on the fundamental properties of atoms joined by chemical bonds to absorb electromagnetic radiation in the 4000–400 cm^{-1} frequency region. In particular, attenuated total reflection fourier-transform infrared (ATR-FTIR) spectroscopy is probably the most available and the fastest method suitable for GO and modified GO characterization. The main advantage is the easy sampling preparation, as one needs only to firmly press soft GO paper against the crystal surface. Another advantage is the rapidity of analysis, that can be performed in just few minutes. The main disadvantage of ATR-FTIR spectroscopy is that it does not allow unambiguous assignment of absorption bands in the fingerprint region; only a few absorption bands can be assigned with a high level of confidence. Another disadvantage of ATR-FTIR is that it is almost purely qualitative.

As a platform bearing numerous functional groups, GO exhibits very rich and complex IR spectra as can be seen in Fig. 2.5. In the high wavenumber region (3600–2400 cm^{-1}), a broad absorption band is observed, primarily attributed to the stretching vibrations of O–H bonds. While it could theoretically arise from tertiary alcohols within GO or water molecules incorporated into the structure, it predominantly results from water molecules [40], with the contribution of alcohol hydroxyl groups being minor.

In the middle of the spectrum, two prominent absorption bands at around 1723 cm^{-1} and 1619 cm^{-1} are characteristic of GO FTIR spectra. These bands consistently appear

in GO spectra across different samples. Their precise positions may vary slightly between studies due to instrumentation differences. They typically fall within the ranges of 1719–1734 cm^{-1} for the first peak and 1615–1626 cm^{-1} for the second peak. The 1723 cm^{-1} band is definitively associated with the stretching vibrations of carbonyl groups, often related to carboxylic functional groups but possibly originating from other carbonyl groups like ketones and aldehydes. In any case, consensus exists that this band primarily arises from C=O bond stretching vibrations.
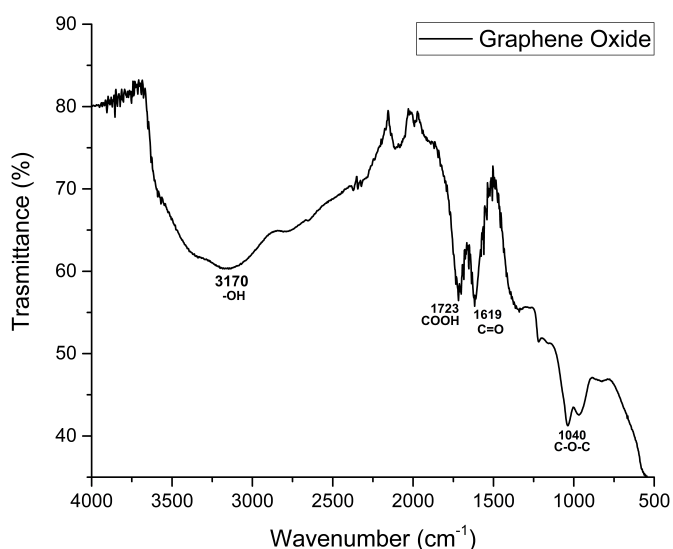
Figure 2.5: ATR-FTIR spectra of pristine Graphene Oxide.

2.3.2 Thermogravimetric Analysis

Thermogravimetric analysis (TGA) is a valuable technique for determining the quantity of functional groups by measuring weight loss with increasing temperature. Several factors contribute to this weight loss, and these factors vary depending on the specific compound being analyzed. The thermal profile of GO (Fig. 2.6) shows three different regions of weight loss in the temperature range considered. In the lower temperature range, specifically below 100 °C, the observed decrease in weight can be attributed to the removal of physically adsorbed water molecules. Moving into the range between 140 °C and 260 °C, the weight loss can be ascribed to the thermal decomposition of oxygenated functional groups. At higher temperature, typically above 450 °C, the weight loss can be ascribed to the oxidative pyrolysis of carbon framework [41] [42]. Graphene exhibits remarkable stability at high temperatures, making the weight loss in the functionalized sample a direct indicator

14

of the quantity of introduced functional groups. In contrast, when analyzing functionalized GO, the weight loss in this temperature range is due to both unreacted oxygenated groups and the covalently introduced molecules. Consequently, to determine the quantity of introduced molecules, one must calculate the difference in weight loss between GO and functionalized GO.
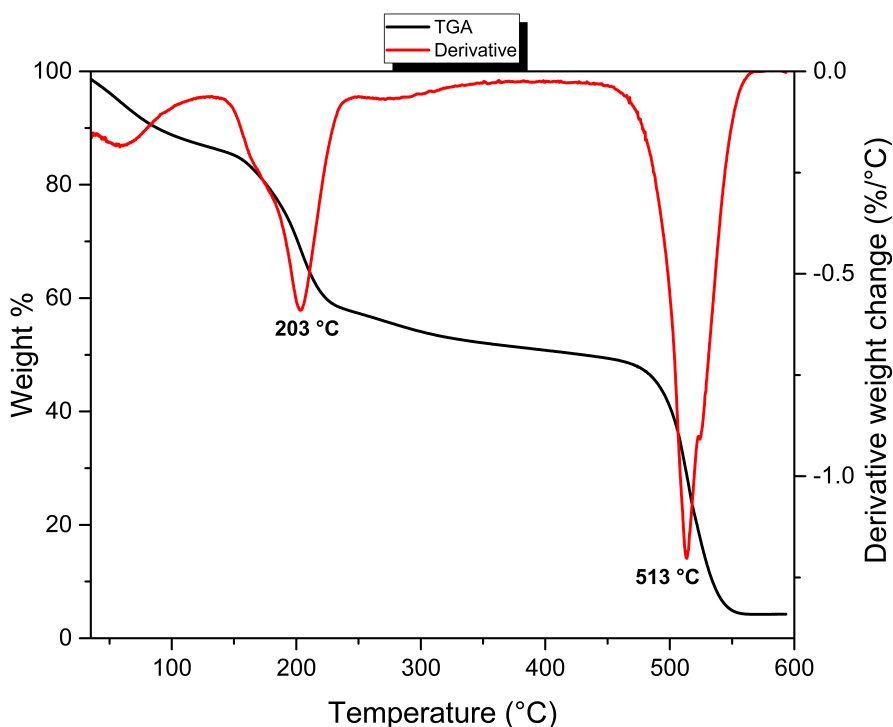
Figure 2.6: Thermogravimetric analysis of Graphene Oxide (10°C/min in air).

2.3.3 Scanning Electron Microscopy

Each individual, GO or modified GO, flake is essentially a two-dimensional nanoparticle, which poses a challenge for optical microscopy due to their minuscule size. If the flakes sizes are in the micrometric range, they can be resoluted using a optical microscopy but smaller flakes are beyond the resolving capability of optical microscopes. However, electron microscopy techniques step in to bridge this resolution gap, enabling the capture of high-resolution images that unveil the structural details of GO flakes. Unlike spectroscopy techniques, which often analyze bulk samples and may not provide a granular view, microscopy methods offer the remarkable advantage of delivering comprehensive data about the morphology of a single GO flake. The high-resolution images obtained through microscopy methods offer insights into the size, shape, and other structural features of GO

flakes, contributing significantly to the comprehensive study and utilization of these nano-materials.

Scanning Electron Microscopy (SEM) is an imaging technique that operates by detecting and collecting secondary electrons emitted when specimen atoms are excited by an incident electron beam. In the realm of GO analysis, SEM stands out as one of the most reliable and robust microscopy methods. Its functionality allows for the rapid scanning of large surface areas of a specimen that includes tens and even hundreds of different GO flakes on the same image.

High-quality GO images can be obtained with magnifications varying from 500 through 100.000. When GO flakes are deposited on a substrate (usually SiO_2 thermally grown on Si and Si with native SiO_x), and, by analysing an elevated number of images, it is possible to do flake thickness statistics of graphene materials. Meanwhile, the transparency of graphene sheets gives indications about the thickness of the graphene samples. More specifically, by examining the edges and grayscale coloration of the SEM image, it becomes possible to count the number of layers [43].
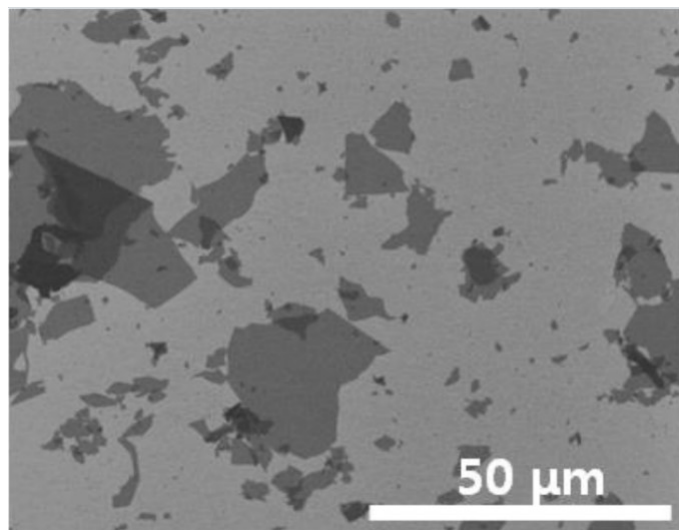
Figure 2.7: SEM images of spin-coated GO film. Figure taken from [44].

2.3.4 X-Ray Photoelectron Spectroscopy

Photoelectron spectroscopy (PES) is one of the most established methods for determining the elemental composition and the chemical state of solid surfaces and thin films. In particular, X-Ray Photoelectron Spectroscopy (XPS), which exploits X-Ray photons to excite electrons from the core levels of the atoms of a solid into the vacuum, is capable of probing the electronic structure of matter with elemental sensitivity and chemical state specificity.

XPS stands as a uniquely powerful analytical method, offering distinct advantages over other techniques like FTIR. What sets this technique apart is its ability to provide both the elemental content of the sample and its quantity.

XPS spectra are generated by exposing a material to a beam of X-rays and then measuring the intensity and kinetic energy of the photo electrons (photoelectrons) emitted by the sample in response to this irradiation. The working principle of the method is based on the law of conservation of energy, written as:

$$\hbar\omega = E_{kin} + \phi + E_{bind} \tag{2.1}$$

Here $\hbar\omega$ is the energy of the incident photons of X-ray radiation, E_{kin} is the kinetic energy of released electrons and E_{bind} is the binding energy (ionization energy) measured in electronvolts (eV). ϕ is the work function of the material and represents the minimum energy required to remove an electron from the solid; it can be seen as an energy barrier that electrons need to overcome in order to escape from the surface into the vacuum. From here, the binding energy can be express as:

$$E_{bind} = \hbar\omega - E_{kin} - \phi \tag{2.2}$$
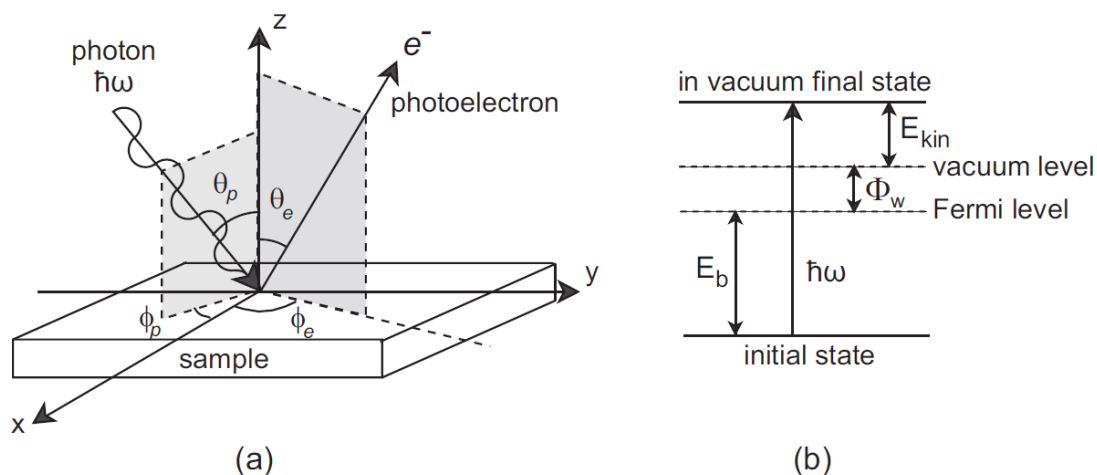
Figure 2.8: Schematic view of the photoemission process: (a) a photon of energy $\hbar\omega$ impinges on a solid surface, and after absorption of the photon an electron is emitted in a given direction; (b) corresponding energy balance within the framework of a electron picture.

Depending on the tested material, usually the photoelectrons are emitted from a depth of several micrometers due to X-ray penetration. However, only the photoelectrons coming from the first 3-7 nm have not lost energy by interacting with other nuclei or electrons, and thus Equation 2.1 is valid, allowing them to be identified as core transitions. Photoelectrons emitted from greater depths lose energy and only contribute to the background

of the spectrum. XPS is a very sensitive tool to determine the entity and quantity of the elements present in the sample.

Regarding GO, XPS not only offers data on the elemental composition but also reveals the type and proportion of functional groups present. When it comes to GO, the most significant insights can be derived from the C_{1s} spectrum, which elucidates various carbon atom states within the sample.

In the freshly cleaved highly oriented pyrolitic graphite (HOPG), no oxygen or defect is present (inset Fig 2.9) and only C_{1s} signal is detectable, at 284.5 eV corresponding to the sp^2 C–C (Fig. 2.9). This peak is not symmetrical, the asymmetry arises from a intrinsic interaction due to band structure of the material. In the HOPG, where valence and conduction bands overlap, interactions with the valence band lead to photoelectrons loose kinetic energy to promote other electrons to higher energy levels within the same band (intra-band transitions). As there is no band-gap, these photoelectrons can lose kinetic energy through a continuos distribution and no discrete transition, resulting in C_{1s} signal that exhibit distortions relative to the intrinsic line-shape, typically described by an Duniac-Sunic or asymmetric Voigt curve [45]. Moreover, the defects present in the lattice, typically C sp^3, present a chemical shift (usually between 0.5 and 1.0 eV) with a peak centred around 285.6 eV, witch is usually modelled with a symmetric Voigt [46] [47].
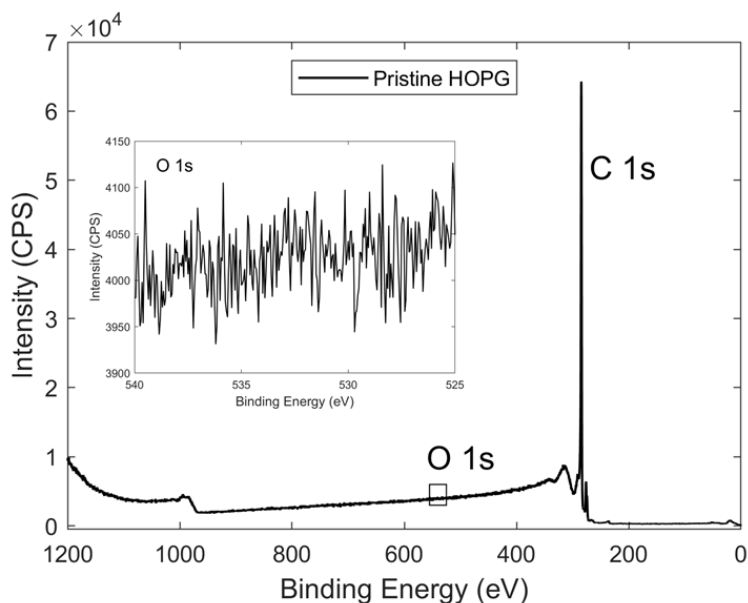
Figure 2.9: Wide spectrum of highly oriented pyrolytic graphite. Inset: zoom-in the range of O_{1s} peak.

In GO the C_{1s} peaks are more complex, as the material present graphenic sp^2 regions,

18

defects and various functional groups (Fig. 2.10). This variety of carbons can generate C_{1s} peaks with different chemical shifts compared to peak centred around 284.5 eV corresponding to the Csp^2. While it is not possible to experimentally differentiate every single component, since the resolution of a standard XPS spectrometer is around 0.9 eV, it is possible to quantify their contribute by performing a deconvolution of the C_{1s} peak.
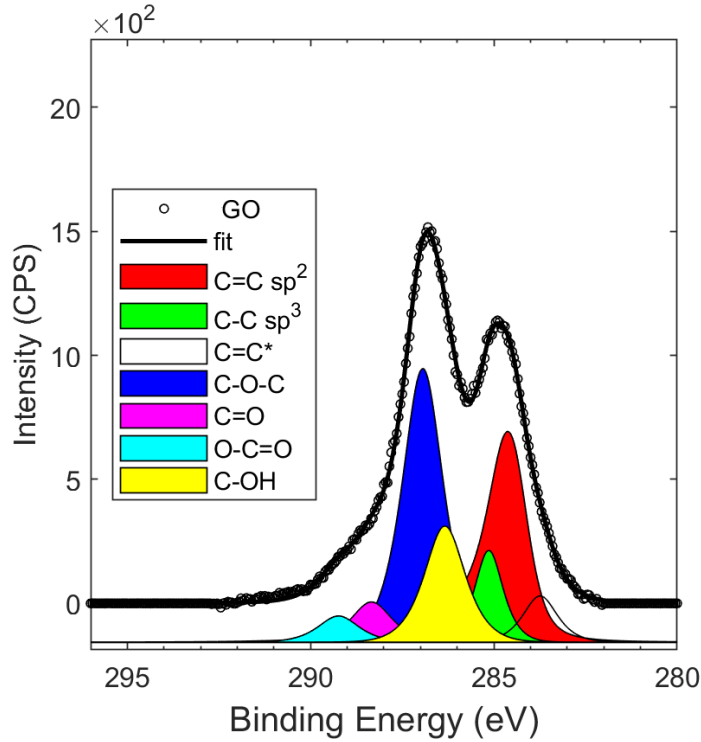
Figure 2.10: The C_{1s} spectrum for GO. The black line is the actual experimental spectrum. The coloured peaks are the component used in the deconvolution.

The peaks position of each functional group are not universally shared, but a wide variety of attribution can be found in literature [48] [49] and in XPS data based from know compound [50]. For the work reported in this thesis, the peaks position considered, based on literature data [47], were: aromatic carbon (Csp^2,2 284.4 eV), aliphatic carbon (Csp^3, 285.0 eV), hydroxyl ($C-OH$, 286 eV), epoxy ($C-O-C$, 286.7 eV), carbonyl ($C=O$, 288.0 eV) and carboxyl ($O-C=O$, 289.1 eV). An additional component for the deconvolution has been considered, the component called $C=C^*$ (283.6 eV). All carbon atoms in the lattice surrounding a single carbon vacancy undergo chemical shifts toward lower binding energy with respect to the Csp^2 peak, i.e., each missing carbon atom causes chemical shift of 12 near-by atoms ranging the first to the third in-plane nearest neighbours [51].

19

It is worth noting that although these deconvolutions could be accurate, they remain largely speculative. There is a virtually unlimited range of potential methods to deconvolute the integral spectra. The critical question is the extent to which we can rely on this data. One assertion can be made with certainty: the C_{1s} XPS spectrum effectively reflects the overall oxidation state of both GO and modified GO. In this regard, XPS is arguably the most efficient and precise method among all the spectroscopic techniques.
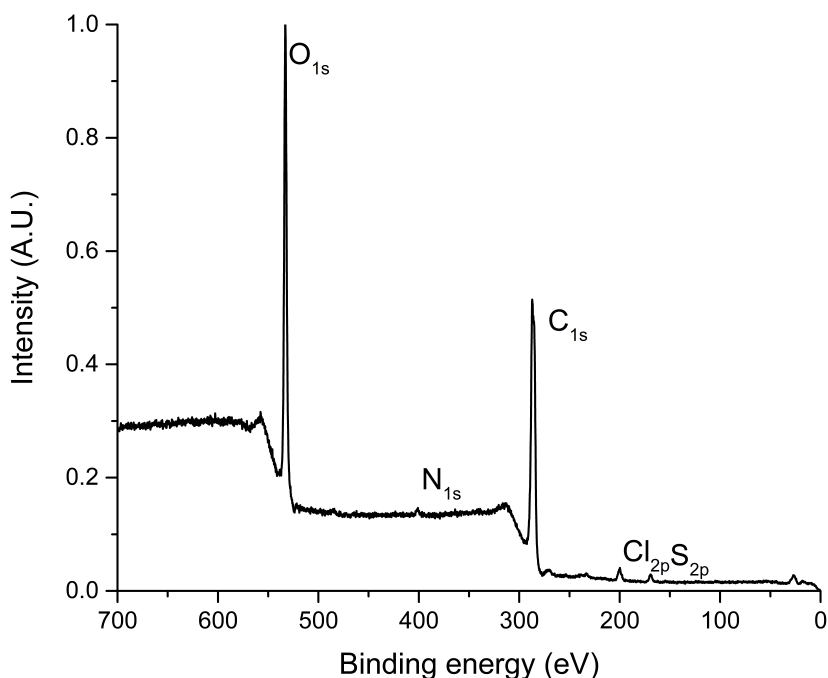
Figure 2.11: Wide spectrum for Graphene Oxide (purchased from LayerOne, batch number S-126/36).

Aside the C_{1s} peak, the typical GO spectrum present another prominent peak, the peak of O_{1s}, centred around 532 eV. A wide range spectrum of GO is reported in Fig. 2.11. As can be seen in Tab.2.1, pristine GO is mainly composed of 98% carbon and oxygen atoms, while the remaining 2% are traces of chlorine, sulphur and nitrogen. These elements are not chemically bound to the structure of graphene oxide but rather the remaining side products of its industrial production.

To correctly quantify the quantity of a defined element in a sample, the Relative Sensitivity Factor (RSF) needs to be taken in consideration. The RSFs are element-specific and they depends on the ionization cross-section, the inelastic mean free path and the analyser transmission function. Furthermore, for simplicity the RSF of C_{1s} is taken as 1 (reference)

	C_{1s}	O_{1s}	N_{1s}	S_{2p}	Cl_{2p}
Binding Energy (eV)	287	532	402	169	199
Graphene Oxide	67.2%	30.3 %	0.7%	0.7%	1.0%

Table 2.1: Atomic composition of graphene oxide.

and all the others are calculated accordingly. The RSF used for this thesis are reported below in Tab. 2.2.

Element	R.S.F.
C_{1s}	1
O_{1s}	2.85
N_{1s}	1.77
Cl_{2p}	2.36
S_{2p}	1.74
Na_{1s}	7.99
Ca_{2p}	5.13
Si_{2p}	0.865

Table 2.2: Relative Sensitivity Factor used for this work.

The quantification of an element can be easily done by using the following formula:

$$Atomic\ content\ \% = \frac{\frac{A_N}{RSF_N}}{\sum^i \frac{A_{Ni}}{RSF_{Ni}}} \tag{2.3}$$

Where A_N is the peak area for the N element considered, RSF_N is the relative sensitivity factor for that element and $\sum^i A_{Ni}$ is the sum of all the peaks area of the elements present in the sample.
Another useful chemical information that can be extrapolated from an XPS analysis is the O/C ratio. This parameter is very important when an accurate classification and comparison between different graphene based material is needed [52] [53].

2.4 Application of modified GO

2.4.1 Water purification

In the last few decades, contamination of water sources has become more frequent all over the world. A wide spectrum of contaminants, spanning from pharmaceuticals, to personal care products, plastics, additives, and more, poses a significant challenge for conventional water treatment methods. These pollutants, some of which are scarcely addressed by current technologies, present a concerning issue, potentially even affecting the quality of drinking water. To compound this dilemma further, our environment faces a relentless influx of over 30,000 chemicals daily. Regrettably, the long-term effects and toxicity of most of these substances remain largely unknown, casting a shadow over their potential impact on ecosystems. These chemicals steadily make their way into the market and subsequently, either directly or indirectly, find their way into our precious water resources. This presents a pressing concern for the sustainability of our water supply and the health of our ecosystems. Drinking water contamination is a major concern to be rapidly faced with the development of new, low cost, sustainable and high-performance materials and technologies.

In December 2020, the European Union adopted the recast Drinking Water Directive and the Directive entered into force in January 2021 [54]. This new law introduces new limits and new contaminants to be monitored and removed. This new directive calls for an urgent development of new technology for detection, early warning, and remediation of those contaminants with proved eco- and human toxicity (such as perfluoroalkyl substances or bisphenol A).

Arsenic pollution in water is a worldwide problem and has been considered as one of the major pollutants in potable water [55]. The occurrences of arsenic at high concentrations in groundwater has been well documented in many countries such as Argentina, Bangladesh, China, India, Mexico, and Vietnam [56].

Nanomaterials, in particular graphene oxide, hold great promise in this field. Due to its high specific surface area and surface reactivity compared to conventional bulk materials nanoparticles, GO showed high potential in controlling heavy metals, organic pollutants, and microorganism removal in drinking water [57].
Graphene oxide represents a scaffold with $\pi - \pi$ interactions, hydrophobic interactions as activated carbons but it also has polar chemical oxygen based groups promoting higher hydrophilicity, electrostatic interaction, higher processability in water. These interactions allow to capture organic molecules and ions from water. Interestingly, studies have shown that GO nanosheets exhibited comparable or better adsorption capacities than other car-

bon nanomaterials, such as carbon nanotubes, toward several contaminants in real operation environment, for example in the presence of normal organic matter. Thus, GO nanosheets are considered a valid alternative as adsorbent for removing organic contaminants from water in engineering applications.

One approach to quantify the efficiency of a given material toward a selected contaminant is to measure removal efficiency as a simple percentage (weight of molecules adsorbed/total weight of molecules in the original solution), measured at a specific concentration. This method, while it could be useful to some extent [58] and for a rapid comparison between two different materials, it does not take in consideration the different experimental conditions (adsorbent, pH, adsorbate, temperature, *etc.*) so it is not possible to make a direct confrontation [59]. An alternative approach measures the weight of contaminant adsorbed at equilibrium (qe, in mg/g) for different equilibrium concentrations of the adsorbate molecule in solution (ce, in mg/L). This data can be then used to model an isotherm of adsorption which can provide information of the maximum adsorption capacity, which is significant in the evaluation of the performance of the adsorbents.

Tuning the selectivity of GO based structures for arsenic removal is a current challenge. On this line, covalent chemical modification of the oxygen-based functionalities of GO could provide a powerful tool to address this issue. For example, enhanced adsorption of heavy metal ions such as Cu(II) and Pb(II), and organic dyes such as methylene blue, in water and wastewater have been reported for EDTA [60], sulphonated [61] and amino rich graphenes [62].

Dinda et al. designed a graphene based 2,6-diaminopyridine adsorbent (DAP–RGO) using surface functionalization of GO [63]. The functionalization was confirmed by FTIR spectroscopy, XPS analysis, TEM and EDX measurement and TGA. The characterization showed a relative hing content of nitrogen after the synthesis. Furthermore, the material was proven to be an efficient remover of Cr(VI) from acidic solutions.

Liu et al. reported a graphene-based thiacalix[4]arenetetrasulfonate nanocomposite (TCAS–rGO) using a convenient wet chemical strategy [64]. The TCAS–rGO nanocomposites were characterized by FTIR, Raman spectroscopy, XPS, scanning electron microscopy SEM, energy dispersive X-ray analysis (EDX), and TGA. They demonstrated that TCAS–rGO possesses excellent selective adsorption capacities for Pb(II) and Cd(II) compared to Na(I), K(I), Mg(II), and Sr(II). Lastly, adsorption behaviour of TCAS–rGO towards Pb(II) and Cd(II) from aqueous solutions was explored by adsorption kinetics, isotherm models, and thermodynamic parameters. The maximum adsorption capacities of the TCAS–rGO toward Pb(II) and Cd(II) were 230 mg/g and 128 mg/g, respectively.

23

2.4.2   Carbocatalysis

In contemporary catalytic technologies, heterogeneous catalysis is the preferred choice over homogeneous catalysis due to its enhanced economic viability and the easiness of separating and reusing heterogeneous catalysts. It is worth noting that the first industrial catalytic reaction, conducted in 1970, involved the oxidation of SO_2 to SO_3 with NO as a homogeneous catalyst. In the present day, over 95% of synthetic chemicals production methods incorporate at least one catalytic step. Catalysis has undeniably become a pivotal factor in the production of materials and chemicals.

For this purpose, catalysis utilizing heterogeneous nanomaterials have been developed, encompassing elements like Co, Au, Ni, Pd, and Pt, to facilitate numerous essential chemical reactions [65] [66]. These nanomaterial-based catalysts serve either as support platforms or as active sites for catalytic processes. Their remarkable feature, enables multiple catalytic reactions to take place simultaneously. However, the high production costs of these metal nanomaterials present a substantial challenge. Consequently, the most promising approach for future industrial process is the advancement of "metal-free" catalysis, a domain currently dominated by carbon-based materials. These materials include carbon black, activated carbon, fullerene, carbon nanotubes, nanodiamond, and graphene.
The rise of graphene in recent years has led to an increase in research reports investigating graphene-based materials for their potential as catalysts and support substances. With a remarkable theoretical surface area of 2630 m^2/g, graphene has attracted substantial attention as a promising heterogeneous catalyst. Nevertheless, in the majority of catalytic systems, pristine graphene has not been the primary focus; instead, researchers have predominantly explored its derivatives. These derivatives encompass graphite oxide (GiO), GO, and chemically or thermally reduced graphene oxide (rGO), collectively referred to as chemically modified graphene.

Graphene-based materials exhibit the capability to catalyse a diverse range of reactions. Some of these reactions display great promise, while others may exhibit lower activity compared to metal-based catalysts. Among these materials, GO stands out as highly active across a variety of reactions [67] [68], spanning from organic synthesis [69] [70] to polymerization reactions [71] [72], indicating its potential for broad catalytic applications.

3. Aim of the Work

The objective of this thesis is the development of new modified GO for the application in the filed of water remediation and carbon dioxide capture and riutilization.

In Chapter 4.1, the aim of the work is the synthesis and characterization of graphene oxide modified with branched polyethyleneimine (GOPEI) materials and its use as adsorbent for drinking water. The synthesis, characterization and its use as adsorbent for arsenic from drinking water is reported. PEI modification with a fluorescent thiophene based dye is also carried out to monitor the evolution of the purification by UV-vis and fluorescence analysis in order to achieve highly pure materials. GOPEI characterization through ATR-FTIR spectroscopy, XPS, SEM imaging and with measure of Zeta Potential is discussed. The material was tested as adsorbent for a mixture of arsenic from tap water. Kinetic of adsorption and adsorption efficiency are discussed together with the mechanism of adsorption established by adsorption isotherms experiments and theoretical models.

In Chapter 4.2, a family of GO nanosheets covalently modified with amino acids and the study on their adsorption properties toward a mixture of selected contaminants, including pharmaceuticals, additives, and dyes is reported. GO derivatives bearing L-Lysine, L-glutamic acid and L-methionine (GO-Lys, GO-Glu and GO-Met) were synthesized and purified with a scalable and fast synthetic and purification procedure, and their structure was studied by combined XPS and elemental analyses. Their properties were compared to unmodified GO, reduced GO (rGO), and to the reference sample GO-NaOH (a GO that was treated in the same condition as the others but without the amino acids). Each type of modified GO possesses a higher adsorption capacity toward bisphenol A (BPA), benzophenone-4 (BP4), and carbamazepine (CBZ) than standard GO and rGO. The maximum adsorption capacity (estimated from the adsorption isotherms) was strictly related to the amino acid loading. Accordingly, molecular dynamics simulations highlighted higher interaction energies for the modified GOs than unmodified GO, as a result of higher van der Waals and hydrophobic interactions between the contaminants and the amino acid side chains on the nanosheet surface.

In Chapter 4.3, we reported a new gram-scale synthesis of a GO-Arg composite. This material was then characterized and its use in the fixation of CO_2 for the chemoselective ring-opening of epoxides to cyclic carbonates was demonstrated. This protocol, once op-

timized, was found suitable for a wide scope (15 examples) and recoverability/reusability (up to 5 cycles) of the material was tested. Furthermore, with dedicated control experiments we were able to shed light on the activation modes exerted by GO-arginine during the ring opening/closing synthetic sequence.

In Chapter 4.3.2 we focused on the application of this material in an ICCC (Integrated CO_2 Capture and Conversion) process. It has been demonstrated that the material is able to capture CO_2 both from high purity atmospheres but also from low concentration mixtures (such as atmospheric one) and to convert it when exposed to dedicated reaction conditions (i.e. synthesis of cyclic carbonates). The entire process was completely studied and rationalized using dedicated computational, chemical physical, and spectroscopic analyses (XPS, BET, TGA, ect).

4. Results

4.1 Scalable synthesis and purification of functionalized graphene nanosheets for water remediation

Graphene oxide modified with branched cationic polyethyleneimine (GOPEI) [73], which exhibits remarkable chelating properties with various metal ions. GOPEI porous foams have demonstrated exceptional effectiveness in removing metal cations like Pb(II) from aqueous solutions, with uptake capacities significantly higher than traditional activated carbons [74]. Additionally, GOPEI-modified cellulose fibers have been used for the pre-concentration of trace arsenate and arsenite, which are of particular concern due to tighter regulations on drinking water quality [75].

To fully utilize modified GO for water purification at a large scale, a high availability of materials and consistent batch purity are essential to prevent secondary contamination. In this context, a novel approach involving microwave-assisted synthesis and microfiltration (MF) on commercial hollow fiber modules has been developed. This method enables rapid modification and efficient, reproducible purification of GO, addressing the need for reliable and stable performance in water treatment processes [76].
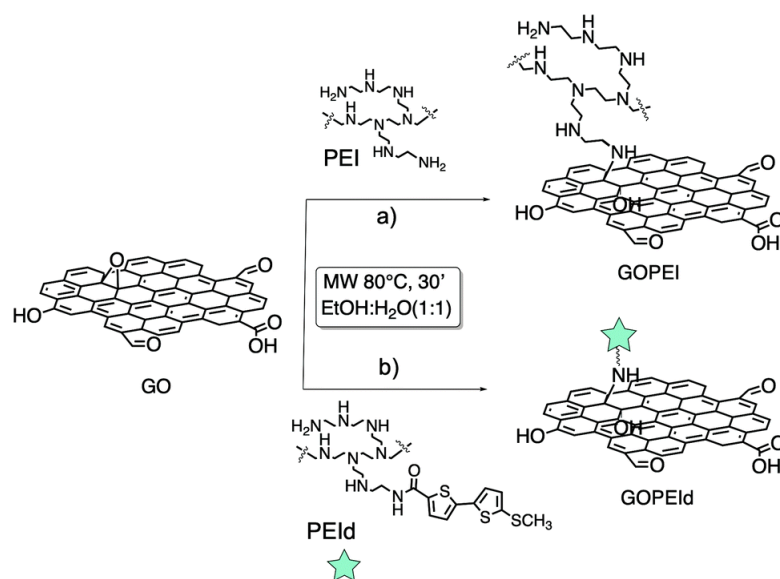
Scheme 4.1: Synthetic pathways to GOPEI and GOPEId.

The rationale behind the MF method relies on the peculiar structure of the module polymeric core, consisting of porous hollow fibers (Versatile PES, Medica SpA) with a cut-off value in the range of 100–200 nm. Due to such a cut-off value, the module can stop objects larger than the pore size while allowing the permeation of smaller species such as reaction side-products including unreacted molecules. Given its already highlighted performance in water treatment, GOPEI was selected as a case study. GO and PEI suspension in water–EtOH was irradiated with MW at 80 °C at a fixed power of 120 W for 30 minutes rather than refluxed for 24 hours under conventional heating as previously described. The same protocol was exploited to synthesize a fluorescent analogue (GOPEId) that is used to monitor the evolution of the purification in the following MF step (Scheme 4.1). To this aim, we used a blue emitting thiophene-based dye functionalized with a succinimidyl end group that spontaneously reacts with the amino moieties of the branched PEI (Fig.5.2, Chapter 5). Then, the crude material was purified by MF on commercial Versatile PESs hollow fiber modules (Plasmart, Medica SpA) in dead-end filtration modality (in-out), i.e. by forcing the solution to pass through the hollow fiber membrane section through a peristaltic pump (Fig. 4.1).
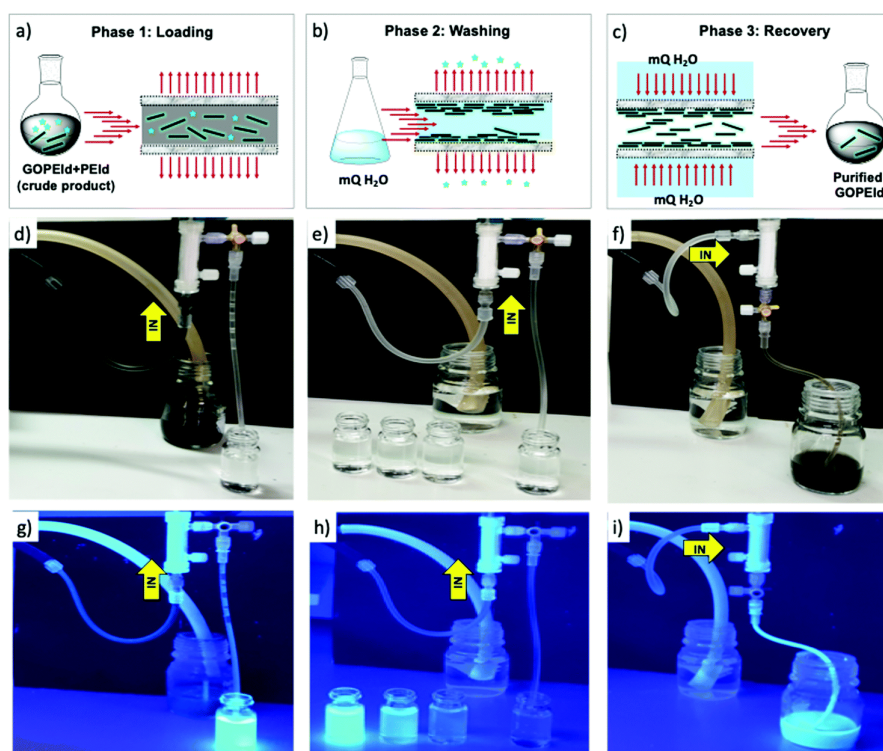
28

Figure 4.1: Sketch of the microfiltration procedure (Plasmart 25 cartridge, Medica spa) and images of the real set-up by using PEId to visually monitor the evolution of the purification. **(a)** Loading phase: the crude suspension is introduced into the hollow fibers passing each fiber from in to out, **(b)** washing phase: the immobilized GO sheets are washed with MilliQ water in the same flow direction (in-out) and **(c)** recovery phase: purified GOPEId is collected in the opposite flow direction (out-in). **(d–f)** Experimental set-up under normal light corresponding to each phase and **(g–i)** same experimental set-up under UV light (λ = 365 nm) showing the evolution of the fluorescence during each phase.

The suspension was introduced into the fiber lume and forced to exit by the outer surface after passing through the section. In this modality (called dead-end in-out mode), the GOPEI sheets could not pass through the fiber pore and remain staked on the inner fiber surface. This was demonstrated by the filtered solution which was clear (Fig. 4.1d). Once immobilized on the inner fiber wall, the GOPEI sheets were washed with ultra-pure water : EtOH solution, until no PEI (or PEId) was detected in the eluted water fractions (Fig. 4.1(e) and 4.1(h)). The monitoring of PEI in the washing water fractions was performed using UV-vis spectroscopy after complexation with copper salts (absorption peak of the Cu–PEI complex at 277 nm) according to already known protocols (Fig. 5.3) [77]. Moreover, for further confirmation we performed the same protocol on GOPEId. The eluted fractions showed intense blue fluorescence until all the unreacted PEId was separated (Fig. 4.1e and 4.1h). Besides the online fluorescence monitoring (Fig. 5.4a, Chapter

5) we performed UV-vis spectroscopy on the collected fractions (Fig. 5.4b, Chapter 5) and monitored the lowering of the absorbance peak of the PEId located at about 350 nm. Due to the separation intrinsically allowed by the microfiltration mechanism, we were able to collect all the unreacted PEI and estimate the degree of PEI loading by (i) complexation with copper, (ii) monitoring the PEId absorbance during elution and (iii) by the weight of the evaporated eluted fractions. According to both procedures, a loading of PEI of about 40% was achieved and about 2.5 L of water were required to purify 1 gram of crude GOPEI. The estimated loading was confirmed also by thermogravimetric analysis (Fig. 5.5, Chapter 5) and XPS. Finally, the washed GOPEI sheets were collected by flowing water in the direction opposite to that of the loading phase (Fig. 4.1c, f and 4.1i) and a total reaction yield of 63% in GOPEI was achieved.

The ATR-IR spectra of GOPEI (Fig. 5.6, Chapter 5) showed the typical fingerprint of GO and the appearance of PEI aliphatic chain peaks in the range of 2850-2960 cm^{-1}. XPS revealed the increase of nitrogen (N_{1s}) in GOPEI from 0.9% for GO to 10.4% for GOPEI, confirming the presence of PEI chains (Fig. 4.2a). Moreover, the amount of PEI could be roughly estimated considering that XPS showed about 10 atoms of N in every 100 atoms of GOPEI; the PEI has a C:N ratio of 2, thus, approximately 30% of atoms in GOPEI can be associated with PEI, in good accordance with post-microfiltration experiments and TGA.
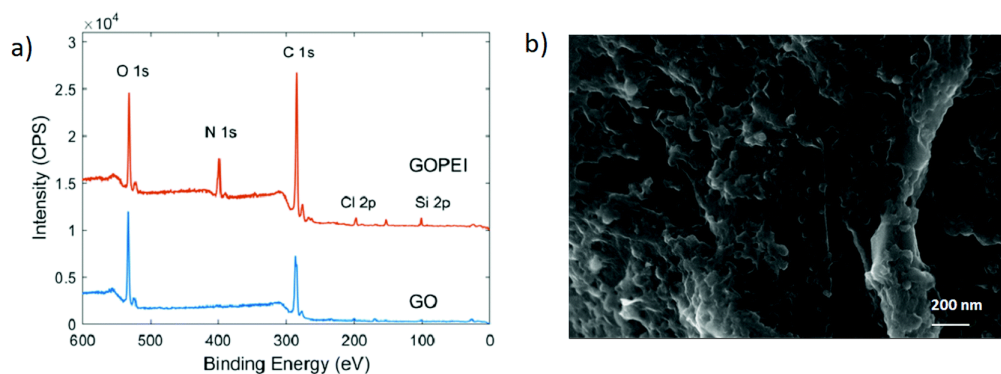
Figure 4.2: **(a)** XPS survey spectra of pristine GO and GOPEI and **(b)** SEM images of GOPEI (sol. 1 mg/L, sonicated for 25 min before deposition of silicon).

The representative morphologies of GOPEI are shown in Fig. 4.2b. GOPEI shows sheets resembling the mesoscopic structure of GO typical sheets, but with amorphous structures at the edge of the sheets probably due to the branched PEI chains. XRD of GOPEI sheets showed the loss of sharp reflection of GO patterns at 10.51 due to the (001) interlayer distance d = 0.84 nm (Fig. 5.7, Chapter 5). The successful grafting of PEI was also confirmed by ζ potential measurements. The negative surface charge of GO with (ζ potential = -23.2 mV) becomes positive after PEI grafting in GOPEI (ζ potential =+14.9 mV).

Microwave–microfiltered (MW–MF) prepared GOPEI was then used as a sorbent for arsenic and lead contaminants, simultaneously from spiked tap water (pH = 7 ± 0.5) at an environmentally relevant concentration (100 mg/L each). Fig. 4.3 shows the removal kinetics of the adsorption for GOPEI in comparison to GO. A 97.6% removal rate has been achieved using GO for Pb after only 10 min, due to its high affinity on the negatively charged surface at experimental pH (GO pHpzc is around 2) and As adsorption was only 10% at 10 min with a decreasing trend (1% at 24 h), due to the anionic form in which arsenate is present at circumneutral pH (Fig. 4.4a).
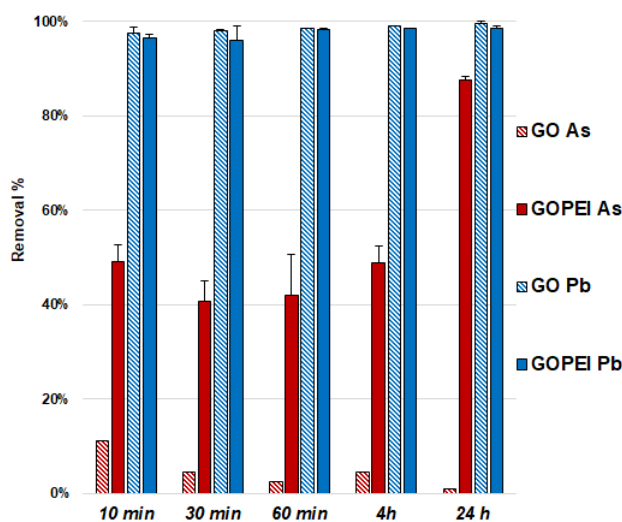
Figure 4.3: As and Pb adsorption kinetics at C_i = 100 μ/L (each), (pH = 7 ± 0). And solid/liquid ratio of 13 mg/30 mL.

PEI modification provided, at this pH, a shift towards more positive surface charges, mainly driven by the protonation of amino groups [78], therefore, we observed an increase in As adsorption up to 49.1% after 10 min (87.5% at 24 h) and simultaneous Pb removal reduction of only 1–2%. Thus, the advantage of GOPEI with respect to unmodified GO has clearly led to the possibility of being used for the removal of both lead and arsenic ions. Removal mechanisms of cationic heavy metals, such as Pb^{2+}, using GO are well studied and reported to depend on the great affinity towards oxygenated groups of the GO surface such as carboxyl, hydroxyl and carbonyl groups[79]. When PEI is added, electrostatic repulsion toward positively charged ions takes over, but there is always attraction towards carboxylic groups present on the graphene, they are not fully protonated above pH = 4,22 which could mediate the formation of polymer–metal complexes with the amino group lone pairs (Fig. 4.4b).
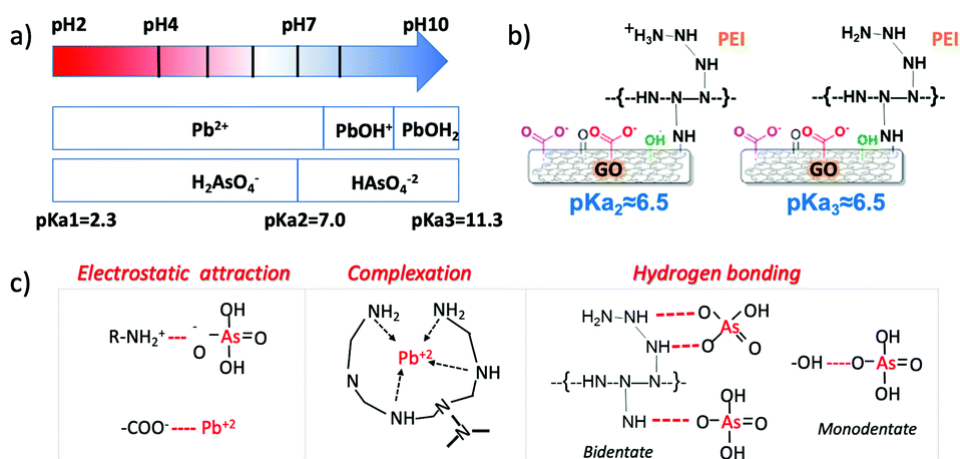
Figure 4.4: **(a)** Contaminant (As and Pb) dominant species in the pH range of interest for water treatment. **(b)** Functional group protonation at the pH close to that used in this work [78], pK_{a2} refers to deprotonation of carboxylic groups in red **(c)** summary of the removal mechanisms driving both As and Pb adsorption according to pH conditions.

Liu et al. stated that Pb adsorption onto fibrils conjugated with PEI was also attributed to the formation of a strong inner complex with the unquaternized N atoms of the amino groups in the PEI chains, especially at pH=4.5. Hence, in the case of Pb, synergetic effects of abundant functionalities in GO and complexation of polyamine are the drivers for adsorption (Fig. 4.4). On the other hand, amine protonated groups favour anionic adsorption, as reported for the case of Cr(VI). The anionic metal and metalloid adsorption mechanism onto PEI has been explained by both electrostatic adsorption and hydrogen bonding formation. A detailed overview of speciation of As and Pb, and functional group protonation/deprotonation versus pH is provided in Fig. 4.4 with suggested mechanisms for adsorption summarized in Fig. 4.4c, based on the observed data and in accordance with previously published papers.

4.2 Amino acid-driven adsorption of emerging contaminants in water by modified graphene oxide nanosheets

The full description of the isotherms of adsorption and the computational data can be found in the published version of this articles. Herein, my main focus is on the contribution I made to the publication.

Amino acid-modified GO has been proposed in recent years as a material with enhanced biocompatibility (methionine) [80], anticorrosion (lysine), lead adsorption [81], and antibiotic (methionine, cysteine) or dye adsorption [82] [83] properties. Nanocomposites of amino acid-GO have been also exploited for magnetic separation of proteins [84] (L-arginine, glutamic acid, phenylalanine, and cysteine), for the fabrication of membranes for direct methanol fuel cells [85] (aspartic acid) or as coatings of electrodes for biosensing applications (methionine) [86].
The synthesis of such modified GO has been generally carried out by amidation after GO carboxylic acid activation by 1-ethyl-3-(3-dimethylaminopropyl) carbodiimide (EDC) or thionyl chloride ($SOCl_2$), followed by reaction with the amino groups. Alternatively, epoxide ring opening reaction by the nucleophilic amino group of the amino acid has also been propose [87] [27].

On this line, aiming at advanced design strategies able to promote specific sorption properties, we report the synthesis of L-Lysine [88], L-glutamic acid and L-methionine-modified GOs [89] (GO-Lys, GO-Glu and GO-Met), their structural characterization, and the investigation on the role of the amino acid in the adsorption properties. The adsorption selectivity and efficiency of these materials toward a selection of contaminants of emerging environmental concern, as a mixture in tap water (including drugs and dyes, whose molecular structures are reported in Fig. 4.5), were investigated by combined kinetic/isotherm adsorption studies and molecular modelling.

33
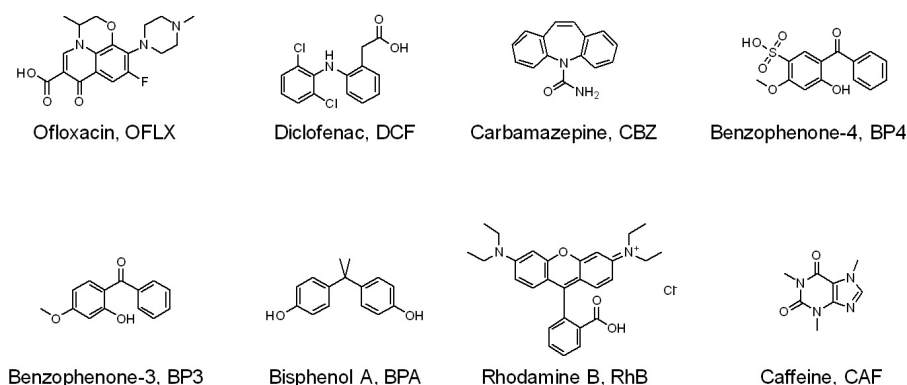
Figure 4.5: Molecular structures of selected emerging contaminants.

In particular, the adsorption mechanism and capacity toward three emerging water contaminants, i.e. bisphenol A (BPA), a plastic additive; carbamazepine (CBZ), an antiepileptic drug; and benzophenone-4 (BP4), a sunscreen ingredient, were deeply investigated. The three selected amino acids have side chains of similar length but strongly different chemical properties. Indeed they are characterized by different charges at neutral pH (Glu: negative, Met: neutral, Lys: positive) and by different pendant groups, i.e. carboxylic (Glu), thioether (Met) or amine (Lys), enabling different types of intermolecular interactions.
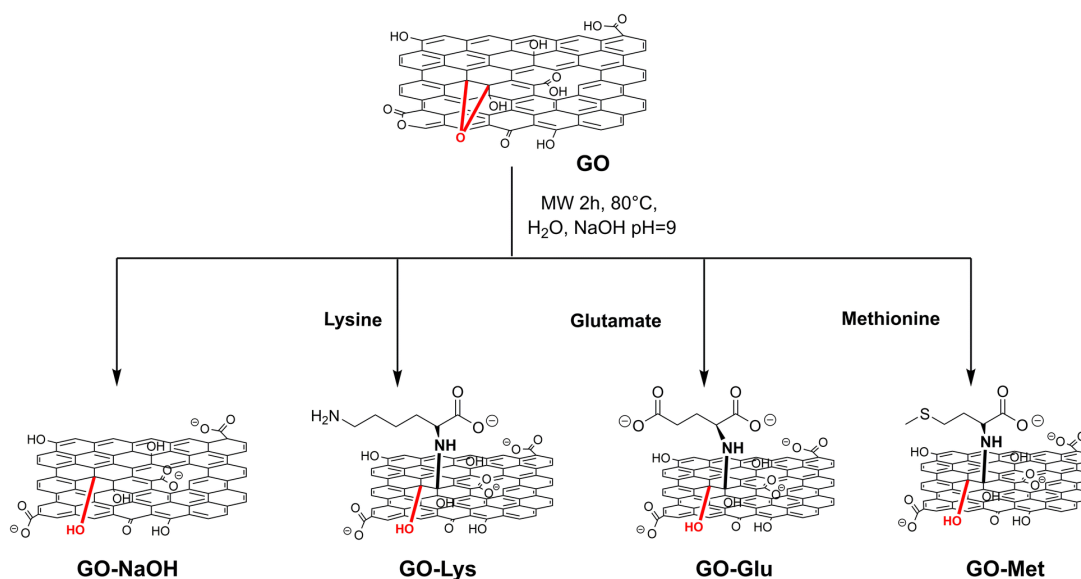
Scheme 4.2: Synthetic pathway to amino acid-modified GOs.

GO-Aminoacids were synthesized by microwave (MW)-activated amination (Scheme 4.2) and purified using a new convenient microfiltration (MF) protocol (Fig. 4.6) (details

in Chapter 5). The microfiltration was performed on commercial Versatile™PES modules (Plasmart 100, Medica Spa). Such modules have a filtering surface of about 0.1 m^2, and cut-off of 150 nm. The dead end in-out procedure (i.e. inlet by point 1 and out by point 3, 2/4 exits were closed), previously reported [88], was here improved by working in the loop-dead end modality, as shown in Fig. 4.6a and b. The crude suspension was flowed through the inner fiber lumen (inlet by point 1, out by points 3 and 4, and recirculation by point 4) and recirculated, while small molecules of size below the fiber pores pass by the fiber section (exit 3). Clean water was progressively added to the crude to purify the modified GO until a neutral pH was measured for the collected GO-Aminoacids solution. The total added volume of water was about 1.5 L/300 mg GO starting material for our procedure with respect to 2.3 L/300 mg required for conventional reiterated centrifugation-based purification. This microfiltration protocol allowed us to speed up the filtration by working at a higher flow rate (100 mL/min), with respect to the previously reported dead-end in-out microfiltration procedure, which works at a maximum of 20 mL/min. In addition, by working in the loop modality, we did not observe clogging of the pores of the membranes, as instead observed in the dead-end closed modality [88].
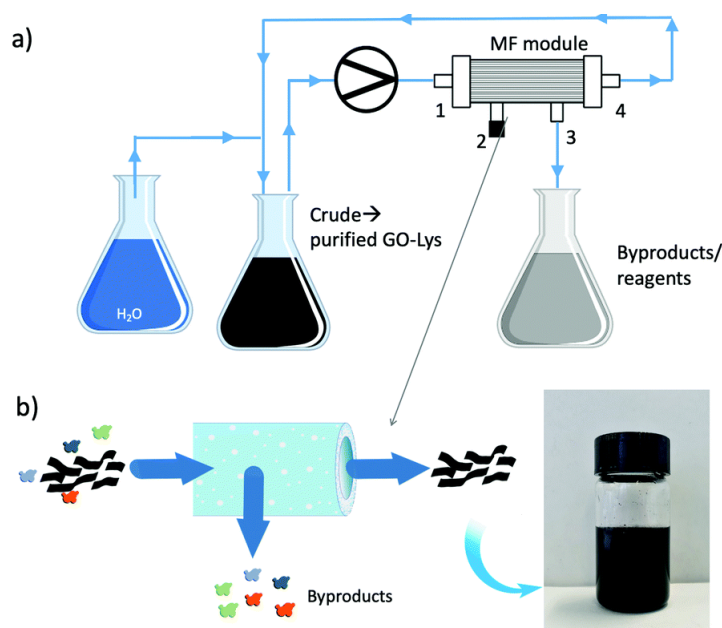

Figure 4.6: **(a)** Sketch of the purification of GO-Amino acids by microfiltration, and **(b)** zoomed-in view of the microfiltration procedure and image of the suspension (2 mg/mL after 30 h from sonication).

The overall procedure resulted in (i) less water/time consumption than centrifugation, (ii) less energy demand, and (iii) less mechanical detriment for the modules than those of

the previously reported microfiltration procedure. Moreover, the cartridges being commercially available with larger size and higher filtering surface, the process could be easily upscaled.

The chemical structure and the amino acid loading ratio for the new modified GO was estimated by XPS. The survey spectra of amino acid modified GOs are reported in Fig. 4.7 and their atomic composition is reported in Tab 4.1. The analysed materials were consistent with the typical structure of modified graphene and were mainly composed of carbon, oxygen, and nitrogen, associated with i) the aromatic sp^2 regions of GO, ii) C–O/C=O functional groups, and iii) the nitrogen functional groups (C–N) present in the amino acids. Since C and O are both present in GO and amino acids, the most significant information about the products was obtained from the N_{1s} signal. The N_{1s} binding energies of NH_2 and NH_3^+ were found in the literature [90]: for each amino acid used in this work, the values were contained within the intervals 399.3–399.6 eV and 401.0–401.4 eV. Unfortunately, it was not possible to univocally discriminate between R–NH–R and R–NH$_2$. As a matter of fact, the corresponding binding energies are overlapping, i.e. the R–C(O)–NH–R group in polyamic acid at 400.5 eV [91] or in Nylon 6 at 399.9 eV. The N_{1s} signal was fitted by two peaks (400.7 eV and 399.4 eV) and one (400.2 eV) peak for GO-Met and GO-Glu, respectively; these binding energies were closer to the R–NH$_2$ or R–NH–R chemical state reported by the literature than to the R–NH$_3^+$ group.

The presence of R–NH$_3^+$ was unfavourable because our reaction was performed under basic conditions. The increase of the N_{1s} signal (from 0.2% for the reference material GO-NaOH to 0.9% and 0.7% for GO-Glu and GO-Met, respectively) was mainly due to the grafting of the amino acids.

It was possible to (roughly) estimate the relative loading of each amino acid from the N_{1s} peak of GO-Lys, GO-Glu and GO-Met. This is possible because most of the N_{1s} signal arises from the bound amino acid, and because the atomic ratios between N and all other atoms visible by XPS are known from their chemical structure (C, N, O, S). Hydrogen is not detectable by XPS. As further proof of the estimated values, we considered the S (S_{2p} signal with a S–C chemical shift at 163.4 eV, Fig. 4.8) in GO-Met and estimated the same loading values obtained by N content estimation.

Materials	Atmoic Composition %							Loading%
	C	O	N	Na	Cl	S	Ca	
GO	70.4	27	0.7	_	0.8	1.0	_	
GO-NaOH	70.4	25.6	0.2	0.2	0.3	_	3.3	
GO-Lys	81.5	13.9	3.1	1.2	0.2	_	_	15
GO-Met	81.2	15.6	0.9	0.7	_	0.8	_	5
GO-Glut	77.1	19.7	0.7	0.2	_	_	2.3	6

Table 4.1: Atomic composition of GO, GO-NaOH, GO-Lys, GO-Glu and GO-Met, expressed in %.
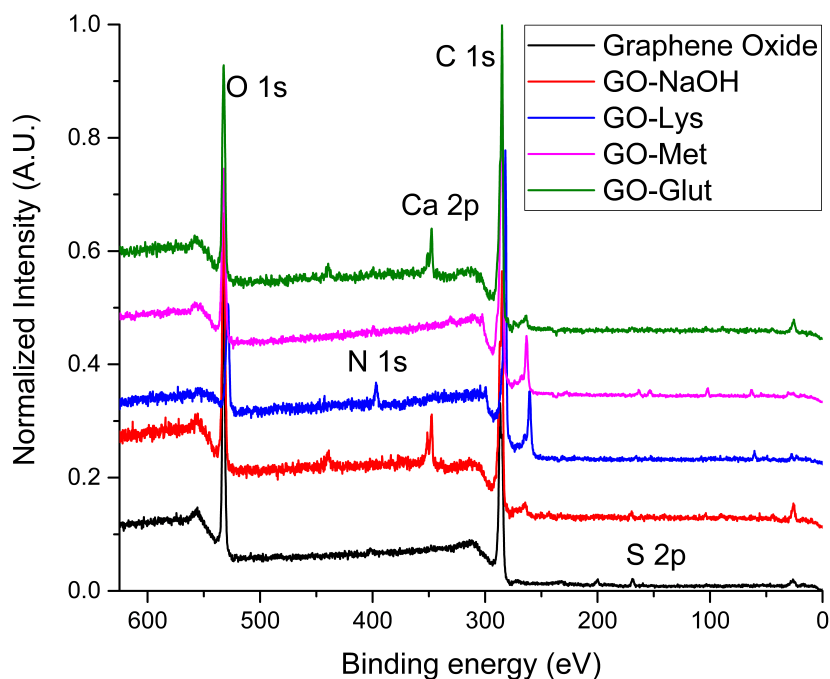
Figure 4.7: XPS survey spectra of GO (black), GO-NaOH (red), GO-Met (purple), GO-Glu (green), and GO-Lys (blue).

It is noteworthy that sulfur was also present in the pristine GO in its typical oxidized form (R–SO$_x$), but the treatment with NaOH removes this group, as confirmed by our experimental evidence (absence of the S$_{2p}$ signal associated with R–SO$_x$ in GO-Met in Fig. 4.8 or any other functionalised GO) and some previous dedicated study by Eigler [29]. GO-Glu and GO-Met showed comparable loading, i.e. 5% and 6%, respectively. The estimated loading for GO-Lys was significantly higher being, about 15%.

Furthermore, the C$_{1s}$ peaks of GO-Lys, GO-Glu and GO-Met were deconvoluted into their component peaks (Table 4.2). From the deconvolution of the C$_{1s}$ signal of GO-Glu, it is possible to observe the increase in the relative amount of carbon sp^2 (43%) compared to the starting GO (31%) as well as for the reference material GO-NaOH (51%). Similarly, the relative amount of carbon sp^2 for GO-Met (46%) is also increased. XPS revealed the presence of a small percentage of residual Na (reaction in NaOH) and Ca (washing procedure).

Elemental analysis (EA) on pristine amino acid and on modified GOs was performed to analyse the bulk composition. The atomic composition (H, C, O, S) of each material was

37
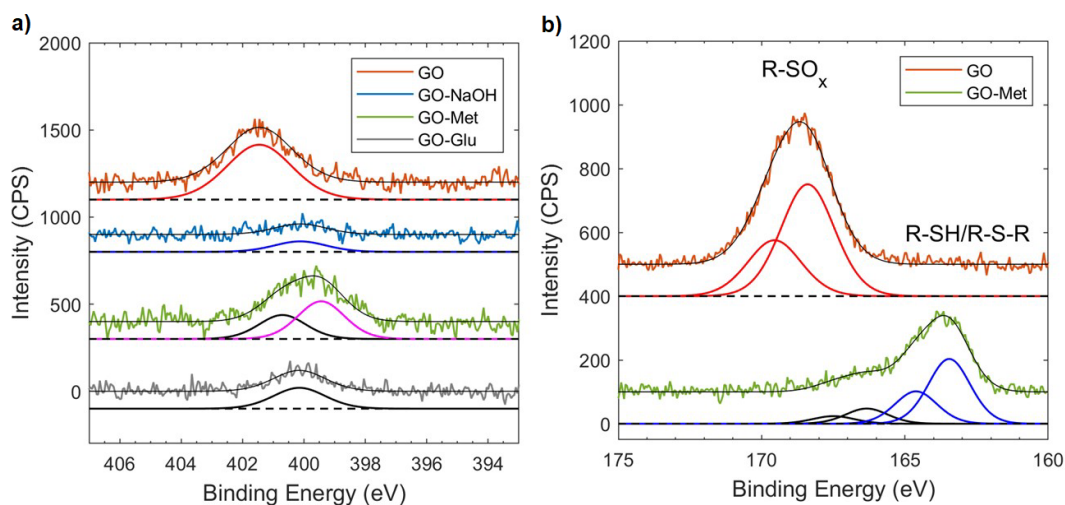
Figure 4.8: **a)**N_{1s} XPS signal of GO, GO-NaOH, GO-Met and GO-Glu. The fitted peaks were at: 401.5 eV for GO, 400.1 eV for GO-NaOH, 400.7 eV and 399.4 eV for GO-Met and 400.2 eV for GO-Glu. **b)** S_{2p} XPS signal of GO and GO-Met. The fitted $S_{2p}^{3/2}$ were at 168.4 eV for GO, 163.4 eV and 166.3 eV for GO-Met.

in good accordance with that estimated by XPS, and is reported in Tab. 5.2, 5.3 and 5.4, Chapter 5.

Materials	C_{1s} fit						
	Csp^2	Csp^3	C=C*	C-OH/C-N	C-O-C	C=O	O-C=O
GO	31.2	7.9	4.8	14.3	33.7	5.0	3.2
GO-NaOH	51.2	8.0	2.6	10.1	19.9	6.0	2.1
GO-Lys	52.6	22.0	1.8	8.7	5.0	7.3	2.5
GO-Met	45.6	14.0	0.3	16.6	13.9	6.6	3.1
GO-Glut	43.3	20.8	1.4	9.0	15.3	6.7	3.4

Table 4.2: C_{1s} deconvolution of GO, GO-NaOH, GO-Lys, GO-Glu and GO-Met, expressed in %. Some groups present possible overlaps (i.e. C-OH and C-N).

In the free amino acid references, atomic ratio (and S/C in Met) was exactly the expected one from the molecular structure, while the O/C and H/C ratios were higher, due to the residual water content. After functionalization of GO, the amount of N increases with respect to GO-NaOH, which was taken as a reference instead of GO, since it was subjected to the same reaction conditions and further purification used for amino acid-modified GOs. The observed O/C ratio was systematically overestimated by elemental analysis with respect to XPS, being 0.77 (EA) vs. 0.38 (XPS) for GO, 0.92 (EA) vs. 0.36 (XPS)

for GO-NaOH, 0.49 (EA) vs. 0.19 (XPS) for GO-Met, 0.67 (EA) vs. 0.26 (XPS) for GO-Glu, and 0.62 (EA) vs. 0.14 (XPS) for GO-Lys.

The observed difference can be ascribed to the different environmental conditions during the measurements of EA and XPS. Indeed, XPS is performed in an ultra-high vacuum, with almost no residual water, while EA is carried out under ambient room conditions; and XPS is surface sensitive (a few nm), while EA is bulk sensitive.

The N/C trend (Tab. 5.2 and 5.3, Chapter 5), which is not affected by water residuals, was in good accordance with that observed by XPS and confirmed the amino acid loading ratio measured by XPS. Overall, the good accordance between XPS (surface) and EA (bulk) data suggested that the reaction between the amino acids and GO nanosheet surface has occurred. The O/C ratio of pristine amino acids was similar to or higher than GO, while, after the functionalization, we observed a systematic decrease of the oxidation degree (XPS O%, XPS and EA O/C ratio); thus, the net loss of oxygen after the functionalization has further changed the surface chemistry of GO, which can be summarised as i) the presence of pendant molecules (the amino acid) and ii) the general decrease of C–O/C=O groups. To distinguish the two effects we have taken into consideration reduced GO (rGO), which has a comparable oxidation degree with the amino acid-functionalised GOs (Table 4.1).

The zeta potentials (ζ potentials) of GO and modified GO nanosheets were measured in deionized water. The obtained values,-35.2 $\pm$ 0.8 mV for GO-Lys, -42.4 $\pm$ 1.2 mV for GO-Glu and -49.6 $\pm$ 1.4 mV for GO-Met, were comparable to the ones measured for pristine GO (-43.1 $\pm$ 2.4 mV), meaning that the surface charge cannot explain the observed different adsorption properties. The morphology of the modified graphene was investigated by scanning electron microscopy (SEM) showing the typical GO nanosheet morphology for GO-Lys, GO-Glu and GO-Met, with a lateral size of a few micrometres, but more aggregated and multilayer nanosheets (Fig. 4.9).

Adsorption selectivity and kinetic studies were carried out on GO, GO-NaOH, GO-Lys, GO-Met, and GO-Glu by measuring the removal of each contaminant from the mixture in the tap water matrix (Fig. 4.10), at different contact times (1 h, 4 h, and 24 h). GO and modified GOs were sonicated for 2 h to exfoliate the bulk material into monolayer nanosheets [92]. Most of the adsorption occurred during the first hours of treatment since no significant differences in removal efficiency were observed between 4 h and 24 h.
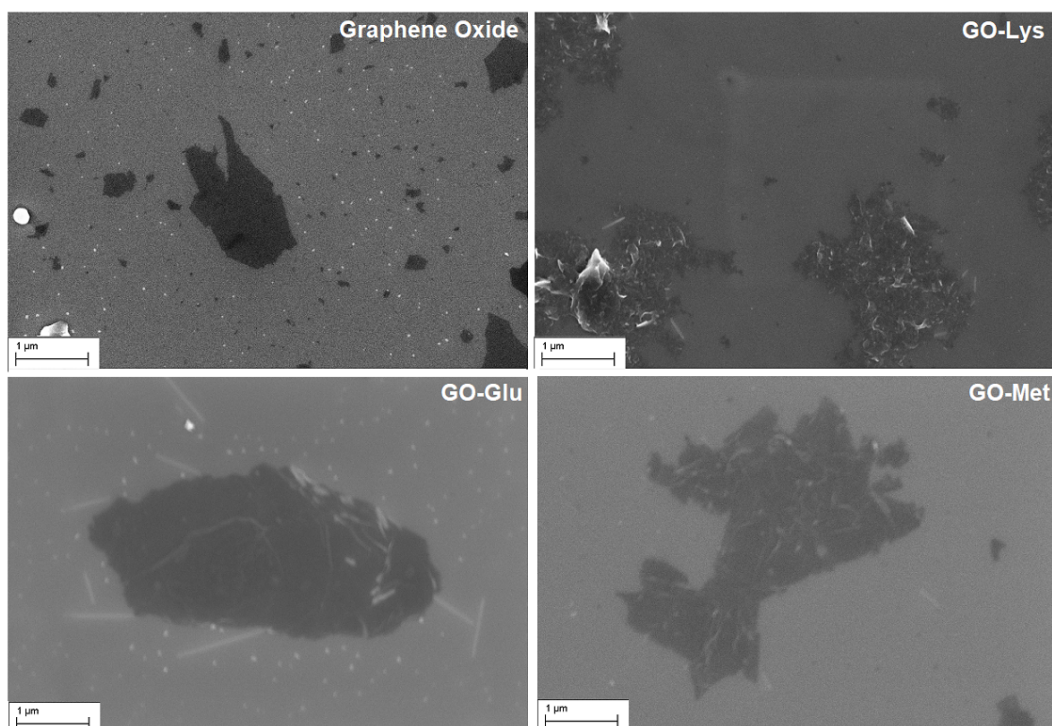
Figure 4.9: SEM images of GO (top left), GO-Lys (top right) GO-Glu (bottom left), and GO-Met (bottom right).
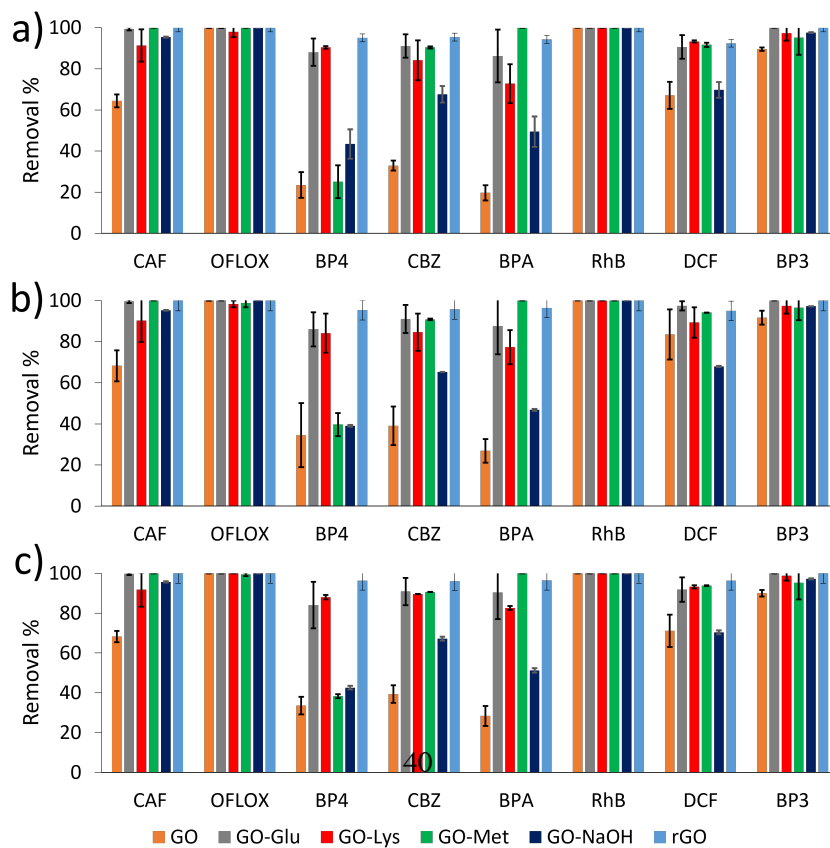
Figure 4.10: Removal at different contact time of each contaminant from the mixture in tap water (total volume=10 mL, sorbent amount= 25 mg, C_{IN}=5 mg/L of each contaminant) by GO (orange), GONaOH (dark blue), GO-Glu (grey), GO-Met (green) and GO-Lys (red). **a)** contact time 1 h, **b)** contact time 4h and **c)** contact time 24 h.

Under the selected conditions, GO showed lower performance for caffeine (CAF), benzophenone-4 (BP4), carbamazepine (CBZ), bisphenol A (BPA), and diclofenac (DCF). The amino acid functionalization changes the surface chemistry of the nanosheets and increases the adsorption selectivity toward the selected contaminants. In fact, modified GOs showed better performance than unmodified GO in the removal of the contaminants that were not completely adsorbed from GO-NaOH (i.e. CAF, BP4, CBZ, BPA and DCF).

The full discussion, modelling of isotherms and molecular dynamics simulation are reported in the articles pubblished on this works [88] [89].

4.3 CO$_2$ capturing and valorization

4.3.1 Recyclable GO-Arginine Hybrids for CO$_2$ Fixation into Cyclic Carbonates

In this work we envisioned the possibility to realize a robust and recoverable metal-free material for the interconversion of CO$_2$ into cyclic carbonates. In order to maximize the efficiency of the process we targeted the simultaneous activation of oxiranes and CO$_2$ by designing a multifunctionalized GO-based composite. In particular, we decided to exploit the GO surface synergistically as a strong H-donor platform (epoxide activation)[93][94][95] and to bind guanidine-like groups for the nucleophilic activation of carbon dioxide (Scheme 4.3) [96] [97] [98].
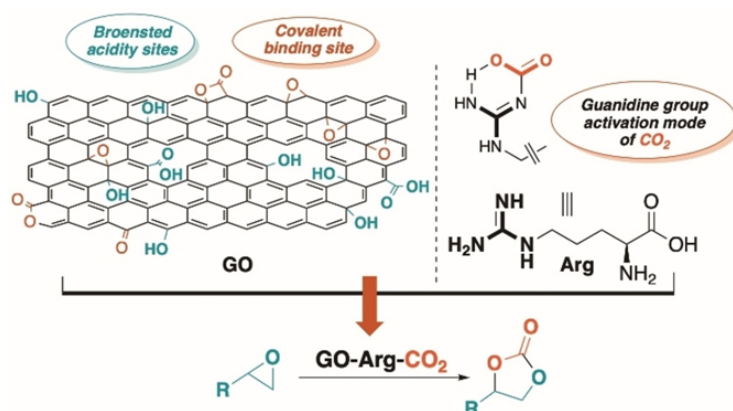
Scheme 4.3: The working idea behind the present methodology.

Focusing on cheap and largely abundant guanidine containing chemical sources, our attention dropped on the naturally occurring amino acid L-Arginine (Arg) that has been reported as a valuable CO$_2$ trapping agent through the formation of arginine-arginine carbamate ion pairs [99]. Additionally, L-Arginine has already found applications as derivatizing agent of inert matrix for the CO$_2$ trapping/valorization; however, harsh reaction conditions (high temperature and pressure) were required to access synthetically convenient efficiency [100] [101] [102]. Accordingly, a new gram-scale synthesis of a GO-Arg composite will be described with application in the chemoselective ring opening of epoxides to cyclic carbonates. Spectroscopic and experimental investigations enabled a full characterization of the material along with a description of the reaction machinery involved.

The model GO-Arg hybrid was obtained on gram-scale (2.3 g/batch) via aminative grafting on GO surface under basic conditions (Fig. 4.11a) [103].

Mechanistically, the ring-opening of the epoxide moieties on GO surface is accounted as most likely during the tagging process. For purification, we exploited the same procedure for microfiltration described before (Fig. 4.11b).
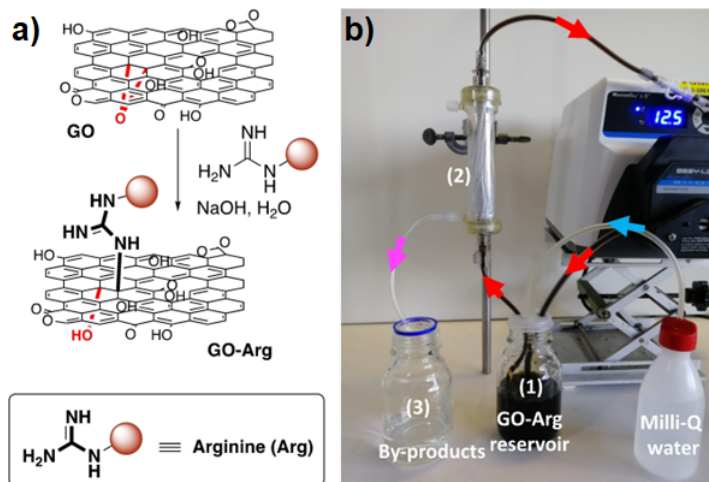
Figure 4.11: **a)** Synthetic route to GO-Arg, for simplicity only one molecule of arginine was represented. **b)** Purification method of GO-Arg by microfiltration in loop-dead end modality [(1): GO-Arg reservoir, (2): purification column via microfiltration on PES modules, (3): impurity accumulation].

The obtained GO-Arg material was characterized by XPS and attenuated total reflectance infrared spectroscopy (ATR-IR), and its properties compared to those of pristine GO and pristine L-Arginine (Fig. 4.12). XPS analysis of GO-Arg is consistent with the typical structure of this material and is mainly composed of carbon, oxygen and nitrogen, associated to: i) the aromatic sp^2 regions of GO; ii) C-O/C=O functional groups; and iii) the nitrogen functional groups (C-N/C=N) present in L-Arginine. Since the increase N_{1s} signal (from 0.7% for pristine GO to 4.9% for GO-Arg) is mainly due to the presence of L-Arginine, it is possible to estimate a relative loading of 14% in GO-Arg by considering the atomic ratios of L-Arginine (C:N:O = 6:4:2).

Furthermore, the C_{1s} and N_{1s} signals of GO-Arg were deconvoluted into its component peaks (see Tab. 5.6). From the deconvolution of C_{1s} signal it is possible to observe the slight increase in the relative amount of carbon sp^2 (40%) compared to the starting graphene oxide (31%). Unfortunately, most of the nitrogen functional groups (C=N or C-N) present in the GO-Arg are in the same binding energy regions of the oxygenated functional groups. The deconvolution of N_{1s} signal of GO-Arg presents four distinct components: i) 401.5 eV (6% of N_{1s}) associated to nitrogen already present in GO; ii) 399.8 eV and iii) 400.5 eV associated to different types of nitrogen atoms present in L-Arginine (86% of N_{1s}) as reported by Artemenko[90] and iv) 398.0 eV (8% of N_{1s}) C that was also associated to L-Arginine (C=N-C group reported at 398.6 eV) [104].

ATR-FTIR spectrum of GO-Arg shows the typical O-H stretching of graphene oxide as a broad peak between 3700 and 2500 cm^{-1} (Fig. 4.12b). In this region there are also present two peaks at 2924 and 2854 cm^{-1}; these can be ascribed to the asymmetric and symmetric stretching of -CH$_2$ of the aliphatic chain of arginine.

Diagnostic signals appeared also at lower wavenumbers (1650- 1550 cm^{-1}, broad peak) that could be associated to the C=C stretching of the graphitic surface and a sharp signal at 1641 cm^{-1} to the –CO$_2$H stretching of the tagged arginine [105].
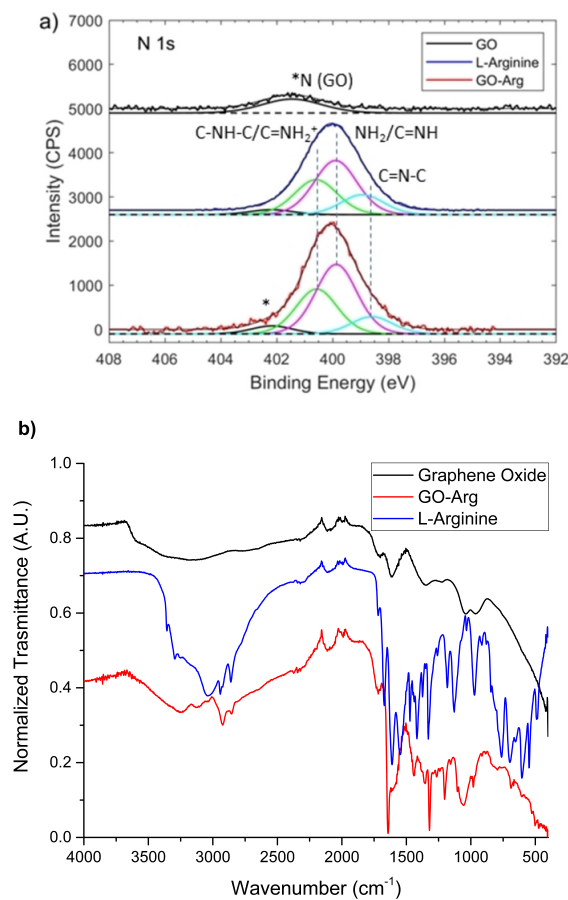

Figure 4.12: **a)** High-resolution deconvoluted XPS spectra of the N$_{1s}$ peak. **b)** ATR-IR spectra of GO, GO-Arginine and L-Arginine.

The GO-Arg material was then employed in the optimization of the reaction conditions through a survey of parameters by adopting the ring-expansion of racemic styrene oxide (**1a**) as a model protocol (Tab. 4.3). Temperatures lower than 100 °C were selected in order to prevent the partial GO reduction via thermal releasing of small molecules (i.e. CO, CO_2, H_2O) and by degradation of low molecular weight fragments from the carbonaceous matrix.
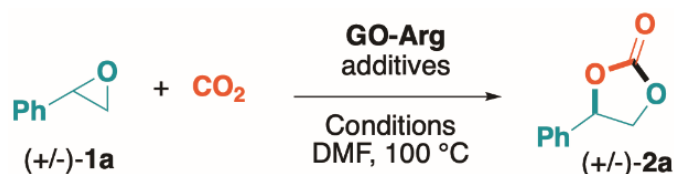
Entry[a]	GO-Arg ($wt\%$)	Additives (30 mol%)	Conditions	Yield of **2a**%[b]
1	160	TBAI	24h	77
2	160	TBAI	48 h	86
3[c]	160	TBAI	24h	62
4	60	TBAI	48 h	73
5	25	TBAI	48 h	83
6	10	TBAI	48 h	75
7[c]	25	TBAI[c]	48 h	84
8	25	TBAI[d]	48 h	75
9	25	//	48 h	//
10[e]	25	TBAI	48 h	//
11	//	TBAI	48 h	12
12	25	TBAI	DMSO, 48h	67
13	25	TBAI	CH_3CN, 48h	//
14	25	TBAI	Dioxane, 48h	20
15[f]	60 (GO)	TBAI	48 h	60
16[g]	60 (Arg)	TBAI	48 h	37

Table 4.3: Optimization of the reaction conditions (TBAI= Tetra butylammonium iodide). [a] All reactions were carried out in dry solvents (0.2 mM, **1a**), additives (30 mol%), unless otherwise specified. [b] isolated yields after flash chromatography. [c] A concentration of 1a = 0.1 mM was used. [d] 20 mol%. [e] The reaction was carried out under nitrogen atmosphere. [f] GO instead of GOArg. [g] L-Arginine instead of GO-Arg. TBAI: tetrabutylammonium iodide.

Delightly, the GO-Arg hybrid (160 wt% to **1a**) proved efficiency in promoting the epoxide ring-expansion and delivered the corresponding carbonate **2a** in 77% isolated yield after 24 h at 100 °C (entry 1) [106]. With the aim to optimize the reaction conditions targeting the minimization of material loading, we were pleased to verify that GO-Arg could promote the titled CO_2 fixation in synthetically useful extent (83%) with loading as low as 25 wt% (entry 5). Furthermore, attempts to improve the reaction performance by:

i) diluting the reaction mixtures ([**1a**] = 0.1 mM, entry 3) and ii) lowering the GO-Arg loading (10 wt%, entry 6), led to comparable or unsatisfying chemical outcomes with respect to the optimal conditions. Blank reactions demonstrated that both TBAI (30 mol%, entry 9) CO_2 atmosphere (entry 10) and GO-Arg (entry 11) were pivotal for the isolation of **2a** (see below for mechanistic interpretations).

Additionally, DMF was elected as the optimal reaction medium via comparison with other polar organic solvents (entries 12-14).

The present composite GO-Arg proved superior competence with respect to the single components (i.e. L-Arg and GO) that provided **2a** in lower extents when utilized independently (yields: 37-60%, entries 15-16). Finally, the genuinely heterogeneous catalysis was circumstantiated by a hot-filtration test that displayed not further advancement in the reaction conversion upon removal of the GO-Arg material after 16 h reaction time (see Chapter 5).

The generality of the methodology was then evaluated by subjecting a range of aromatic (**1b-j**) as well as aliphatic epoxides (**1l-o**) to the ring-expansion protocol, by means of the optimal conditions described in Tab.4.3, entry 5 (Scheme 4.4). Within the series of aromatic epoxides, we recorded the good to excellent yields (up to 82%) on the corresponding cyclic carbonates regardless both electronic properties and position of the substituents. In addition, aliphatic epoxides turned out to be highly reactive on the optimal conditions yielding the desired cyclic carbonates **2l-o** in good to high isolated yields (up to 79%).
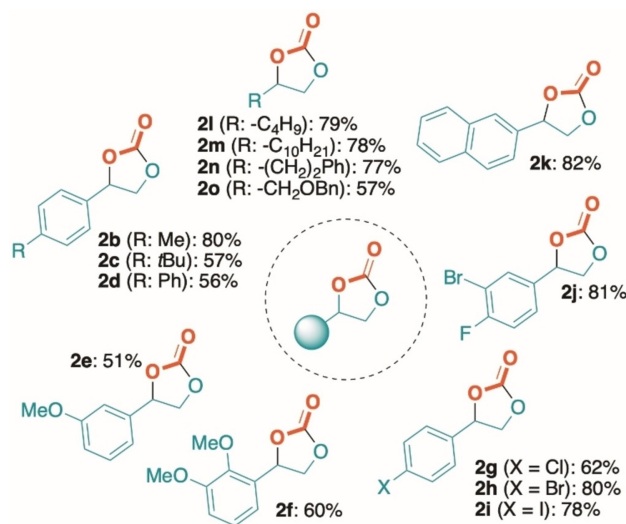
Scheme 4.4: Scope of the present CO_2 fixation into cyclic carbonates.

The robustness of the functionalized GO was then considered by assessing both recoverability and reusability of the heterogeneous promoter. In particular, the carbonaceous

material was easily separated by the reaction products via centrifugation. Repeated washings with a EtOAc/DMF mixtures enabled the effective removal of the TBAI residues from the solid materials that were finally recovered via dispersion into water and subjected to lyophilization before re-use. With this simple protocol, we were able to recover quantitatively the GO-Arg employed in every run and reuse the material up to 5 consecutive CO_2 fixations providing substantially similar performance both in terms of overall chemical yield (Tab. 4.4 Top) and kinetic profiles (see Fig. 5.11). The chemical integrity of the GO-Arg surface before and upon after a catalytic cycle was also verified by C_{1s}, O_{1s} and N_{1s} XPS-analyses (Figure 4.4 Bottom and Chapter 5 Fig. 5.9).

Cycle	I	II	III	IV	V
2a	82	78	75	75	74
GO-Arg*	98	98	98	98	98
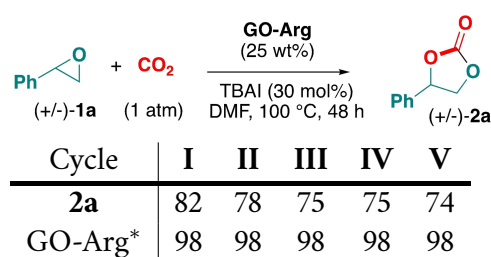
GO-Arg	C%	O%	N%
Pristine	73.7	19.6	4.9
I Cycle	79.4	15.2	4.4
II Cycle	79.8	15.2	4.1
III Cycle	80.8	14.3	3.9

Table 4.4: **Top**: Recycling experiments on the model reaction **1a** $\rightarrow$ **2a**. **Bottom**:Proving the morphological integrity of the GO-Arg composite along the recovering/reuse tests (XPS atomic %). The % of GO-Arg recovered is referred to the amount employed in the previous run.

In particular, the overall chemical surface composition of GO-Arg changed only marginally over the five catalytic cycles accounting for the chemical robustness of the carbo-material in our conditions. Here, the slight reduction observed after the first cycle could be ascribed to an unavoidable partial de-oxygenation of GO upon repeated thermal treatments [106]. This loss did not seem to involve the arginine pendant, given the unchanged nitrogen content recorded. Additionally, no traces of residual TBAI were identified in the recovered GO-Arg material upon the catalytic iterations.

Therefore, we addressed our efforts towards the comprehension of the activation mode exerted by the polyfunctionalized amino acid pendants (i.e., guanidine unit, primary amine) once covalently tagged to the surface of the GO layers. To this purpose, we synthetized N-alkylated guanidine **5a** by condensing S-methylisothiourea hemisulfate (**4a**) with n-pentyl amine **3a** [107]. The guanidine derivate **5a** was then implemented in the covalent derivatization of GO,following the synthetic methodology described in Scheme4.5.
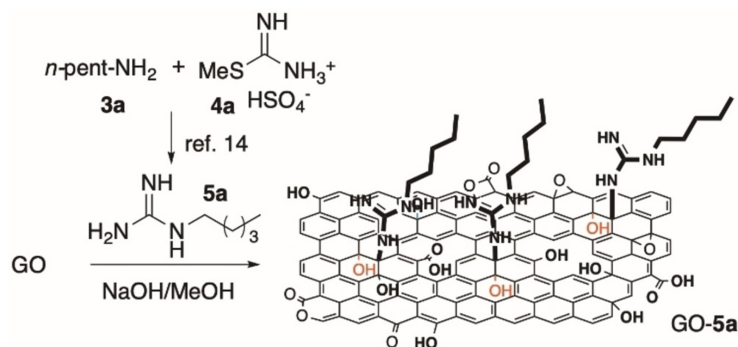
Scheme 4.5: Synthesis of N-alkylated guanidine **5a** and implementation in the realization of the composite GO-**5a**.

The GO-**5a** obtained in this way was characterized by XPS and ATR-IR, and its properties were compared to those of pristine GO and GO-Arg (Fig.4.13). XPS of GO-**5a** presented a similar structure compared to GO-Arg. Here, an increase of nitrogen content was observed (3.5%, N_{1s} at 400.0 eV). Accordingly, a a 12% loading of **5a** was estimated by considereing the atomic composition of **5a**.
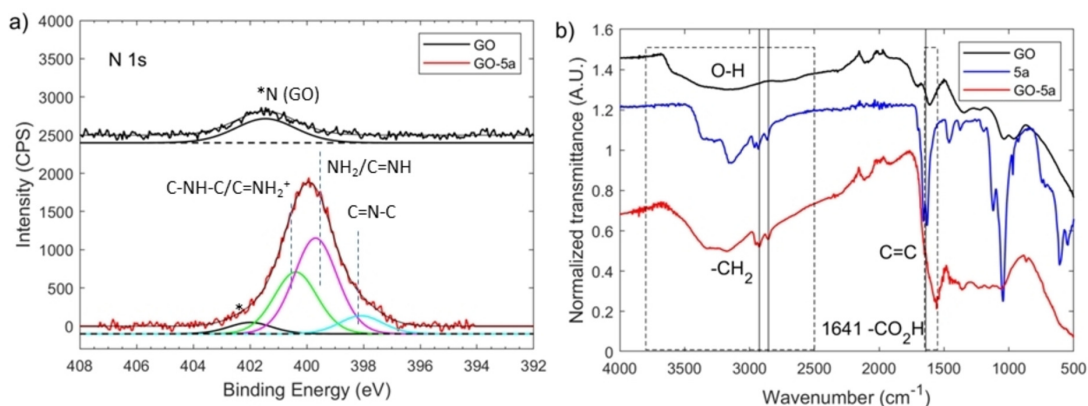
Figure 4.13: **a)** High-resolution deconvoluted XPS spectra of the N_{1s} peak of GO-**5a**. **b)** ATR-IR spectra of pristine GO, GO-**5a**, and **5a**.

ATR-FTIR spectrum of GO-**5a** shows the typical O-H stretching vibration peaks of GO (3700 and 2500 cm^{-1}) and two diagnostic peaks at 2924 and 2854 cm^{-1} (absent in GO) that can be ascribed to the stretching of the -CH$_2$ units of the aliphatic chain of **5a**. Finally, the sharp peak at 1641 cm^{-1}, attribute to the carboxylic group stretching in GO-Arg (Fig 4.12b), here was absent.

Interestingly, when GO-**5a** was utilized in the optimized fixation of CO$_2$ (Tab. 4.3, entry 5), the corresponding cyclic carbonate **2a** was isolated in comparable yield to GO-Arg (88% yield) supporting the pillar "double" role exerted by the guanidyl unit in the present methodology. As a matter of fact, the superbase core is proven to participate in the covalent linking of the GO surface and in the transient activation of CO$_2$. On the contrary, the present experimental and spectroscopy evidence indicate the concomitant involvement of the -NH$_2$ group of L-Arg on the catalytic process unlikely or at least non predominant. Finally, some preliminary control experiments were carried out on enantiomerically pure styrene oxide (S)-**1a**, providing important insights to formulate a tentative reaction picture (Scheme 4.6). In particular, when the methodology was adapted to enantiomerically pure styrene oxide (S)-**1a** the corresponding carbonate **2a** was isolated with substantial racemization (ee = 77%, Scheme 4a-i). Intrigued by this partial loss of stereochemical information, some dedicated experiments in the absence of CO2 were carried out to locate the racemizing step on the mechanistic profile. Here, while GO-Arg and TBAI alone led to the recovery of (S)-**1a** with negligible racemization (ee = 94% and 93%, respectively), stirring (S)-**1a** in the presence of a mixture of GO-Arg and TBAI (DMF, 100 °C, 16 h) caused a significant drop in the enantiomeric excess of the oxirane (ee = 51%).
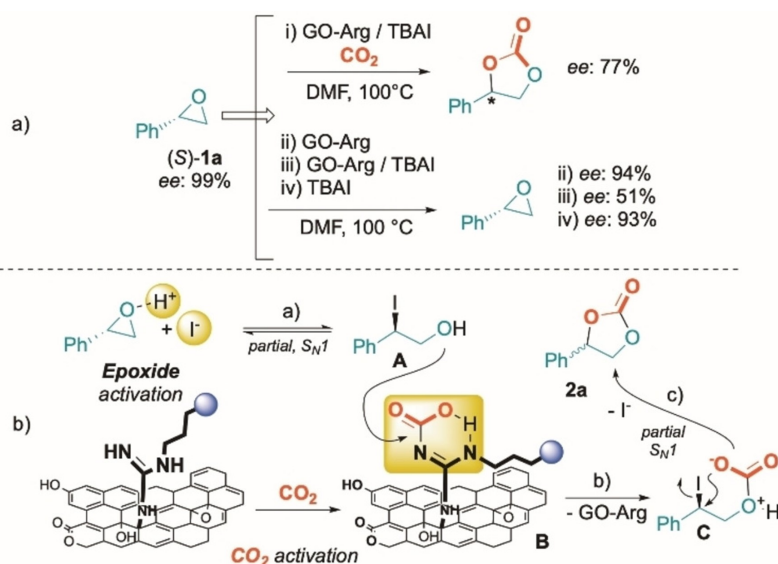
Scheme 4.6: **a)** Mechanistic control experiments on enantiopure styrene oxide. **b)** Pictorial mechanistic sketch of the present CO$_2$ fixation reaction.

49

With this information in hand, some mechanistic conclusions can be drawn. In particular, both the iodide anion and the Brønsted acidity released by GO in solution are involved in the initial ring-opening stage a) Scheme 4.6b. This step resulted reversible through a partial S_N1 profile, as testified by the observed racemization of 1a under CO_2-free conditions. Therefore, the resulting a-iodo-alkoxide intermediate A can trap one molecule of CO_2 previously activated by the guanidyl group of the GO-Arg composite B. Finally, the carbonate releasing by intermediate C will occur by means of an intramolecular iodo displacement reaction. The partial racemization recorded with enantiopure **1a** suggests that either steps a) and or c) could feature a not negligible S_N1 profile. Although the activation of CO_2 by physisorption phenomena could likely parallel the herein proposed covalent interaction (B), previously reported covalent activation modes of carbon dioxide on similar amino functionalized materials prompted us to propose the formation of transient carbonates as key intermediates of the process [108].

4.3.2 Graphene Oxide-Arginine Composites: Efficient Materials for Integrated CO_2 Capture and Conversion - ICCC

Here, we continue with our recent finding in GO-Arg composite in the interconversion of epoxides to cyclic carbonates via CO_2 insertion [109] [110]. The electrophilic activation of carbon dioxide by the guanidinium unit of the amino acid [96] [97] [98] was documented as the pivotal chemical event for the final ring-expansion step. In addition, the effectiveness of organic amines as "sponges" in CO_2 capture methodologies is well consolidated [111]. Therefore, we envisioned the possibility to combine these findings for the realization of an unprecedented ICCC process with the synthesis of synthetically valuable cyclic carbonates as final valorized form of CO_2 [112]. Remarkably, this proof-of-concept protocol would address all the afore described open tasks, by introducing a single metal free composite capable, an "on-demand", of both CO_2 trapping and its chemical activation. Additionally, the application of ICCC to C-O bond forming reactions would open new horizons in the preparation of added-value and structurally elaborated chemical compounds via direct CO_2 capture/fixation procedures.

The GO-Arg composites (GO-Arg 1:1; 1:3 and 1:5) were promptly synthetized by means of variant of known aminative procedures on GO surface [102]. In particular, aqueous suspensions of GO (100 mg, pH = 12 adjusted with NaOH) were treated with 100 mg, 300 mg and 500 mg of L-arginine (Arg), respectively. Under these conditions, a covalent grafting of the amino groups of arginine on GO via epoxide ring-opening is postulated [103] [27]. Conceptually, based on the side where the nucleophile approaches the GO surface, the reaction can generate a syn- or an anti-β-amino alcohol framework. In this context, we investigated the two stereodivergent mechanisms by means of quantum mechanical and molecular mechanical (QM/MM) computations and the resulting potential energy surfaces (PESs) have been collected in Fig. 4.14. Interestingly, both kinetic and thermodynamic parameters converge towards election of the anti-attack as the most likely one. In details, comparing the kinetics of the two mechanisms, the activation barrier for TS_{syn} is slightly higher than TS_{anti}, being 12.6 kcal/mol vs 9.1 kcal/mol in the case of the anti-attack. Analogously, from a thermodynamic point of view, the formation of the anti-GO-Arg resulted strongly favored (-34.4 $kcal/mol$) respect to the syn-GO-Arg (-4.5 kcal/mol). Steric hindrance issues in the ring-opening product and large accessibility of the anti-face of GO during the ring-opening events account for the aforementioned computations.
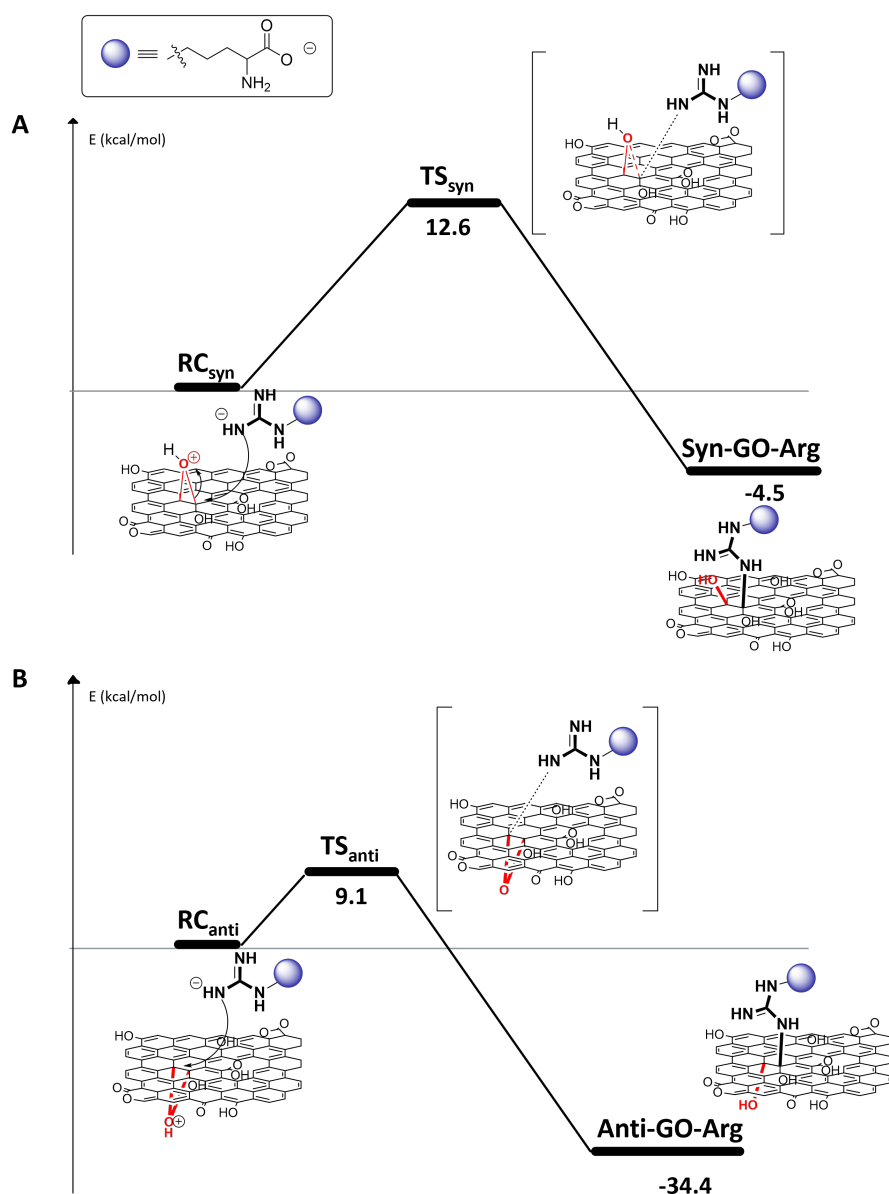
Figure 4.14: PES obtained for the two possible stereodivergent mechanisms of β-amino alcohol formation upon *syn* (A) or *anti* (B) covalent grafting of arginine on GO via epoxide ring-opening. 2D-representation of the critical points are also inserted as insets.

Therefore, the superficial loading of arginine was experimentally determined via XPS analysis and in particular, the degree of surface decoration of GO was evaluated by monitoring the N_{1s} signals. As can be seen in Fig. 4.15 and Table 4.5, The materials GO-Arg 1:1, GO-Arg 1:3 and GO-Arg 1:5 presents a significantly higher amount of N respect to the pristine GO. In particular, for GO-Arg 1:1 an atomic nitrogen content of 1.6% was recorded

that lifted up to 4.5% for GO-Arg 1:3. Differently, by further increasing the GO:Arg ratio up to 1:5 no significant variation on nitrogen content was recorded (5.9%) Based on these outcomes, the estimated arginine loadings were 5%, 14% and 18%, respectively. Since the increase N_{1s} signal is mainly due to the presence of L-Arginine, it is possible to estimate a relative loading by considering the atomic ratios of L-Arginine (C:N:O = 6:4:2). The overall oxidation (O_{1s}/C_{1s}) was lower than GO due to the presence of aliphatic chains of arginine. The presence of Ca_{2p} (347.5 eV) in the samples can be ascribed to the presence of Ca ions in the washing water used during purification.
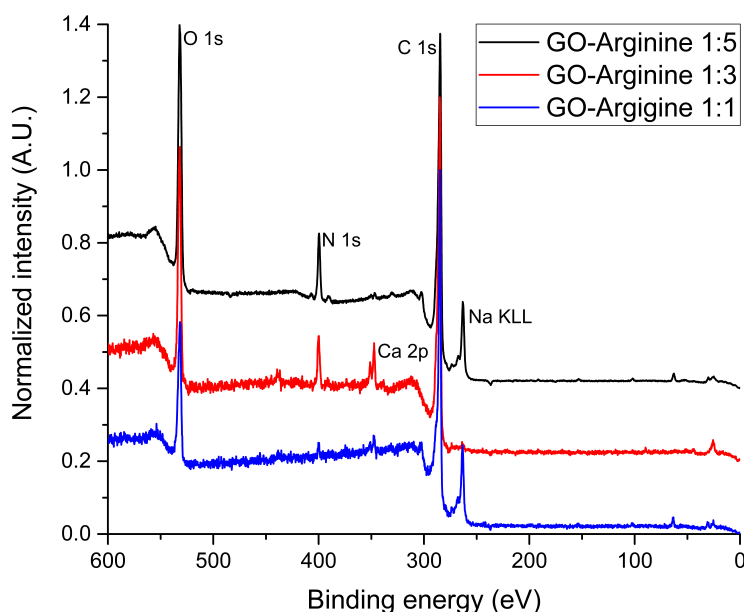
Figure 4.15: Survey spectra of **GO-Arg 1:1** (blue line), **GO-Arg 1:3** (red line) and **GO-Arg 1:5** (black line).

Materials	C%	O%	N%	Na %	Ca %	Loading %
GO-Arg (1:1)	84.3	14.4	1.6	<1	<1	5
GO-Arg (1:3)	73.7	19.6	4.5	<1	<1	14
GO-Arg (1:5)	73.1	21.1	5.9	<1	1.5	18

Table 4.5: Atomic compositions of the materials calculated by XPS analysis.

The CO_2 adsorption capacity of the dry Arginine-functionalized GO samples with different arginine amounts was measured by registering the mass change of the samples via

TGA analysis. The adsorption/desorption curves are shown in Fig. 4.16a. The first part of the curve shows the cleaning cycle at 90 °C and the temperature decreasing to 40 °C in pure N_2. The second part of the curve is the absorption of CO_2/N_2 1:2 % v/v mixture, while the third one shows the CO_2 desorption at 90 °C in N_2. Each sample responds rapidly to the adsorption process due to the reaction between the arginine linked to GO and the carbon dioxide.
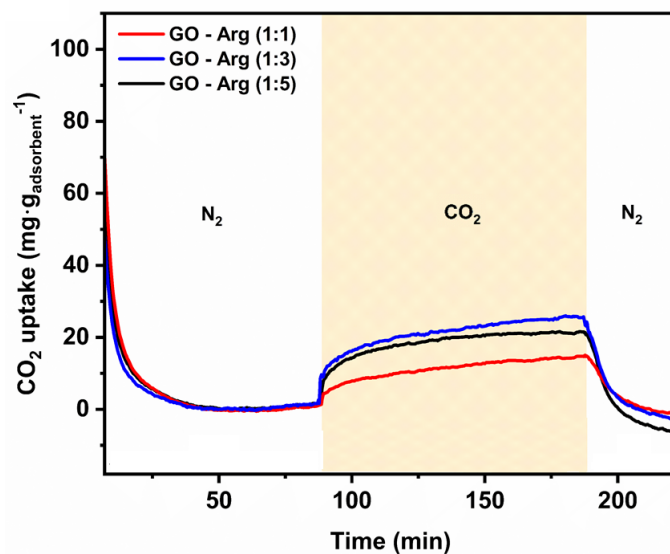
Figure 4.16: CO_2 adsorption/desorption curves (1 cycle) of the Arg-functionalized GO samples with different Arginine amounts.

Materials	CO_2 uptake ($mg_{CO_2}/g_{adsorber}$)	CO_2 uptake static ($mg_{CO_2}/g_{adsorber}$)
GO-Arg (1:1)	16.3 ± 0.8	20.1 ± 1.0
GO-Arg (1:3)	23.1 ± 1.1	26.5 ± 1.3
GO-Arg (1:5)	28.2 ± 1.4	39.3 ± 1.9

Table 4.6: CO_2 adsorption capacity of the arginine-functionalized GO.

The extrapolated CO_2 uptake mean values for 1:1, 1:3, and 1:5 samples are reported in Tab. 4.6. These values increase with Arginine loading from 1:1 ($18.8 \pm 3.5\,mg/g$) to 1:5 sample (highest adsorption capacity of $28.2 \pm 1.4\,mg/g$) due to the increased active sites of the material. The same trend of adsorption was registered under pure static CO_2 absorption conditions (2 h, Tab. 4.6, see Chapter 5 for details). The uptakes recorded using this

method are higher than the ones reported for conventional TGA analysis in flow due to the different operating conditions (i. e. GO-Arg 1:5, 39.3 ± 1.9 mg$_{CO_2}$/g$_{adsorber}$). Interestingly, the recorded CO_2 adsorption capacity of the GO-Arg 1:5 composite (ca. 1 mmol of CO_2 per g of adsorbent) are in line with the reported adsorption values of amine-based materials for CO_2 trapping and utilization [113].

GO-Arg 1:5 sample was also considered to determine the CO_2 absorption in open air at room temperature. The adsorption capacities measured using TG analysis after 1, 2, 3, 4 and 6 days were reported in Fig.4.17 and Tab.4.7. The data show a nearly exponential increasing of the CO_2 uptake until the 4th day. After this time, a stabilization of the uptake was observed at values of mg$_{CO_2}$/g$_{adsorber}$ similar to the ones registered for the static absorption of the sample. It is important to note that the desorption occurred at the same temperature of the previous experiments as confirmation of the selective CO_2 absorption. Remarkably, these results emphasize the ability of the GO-Arg materials to selectively absorb the CO_2 present in the environment nevertheless its lower concentration. Due to the higher similarity between the analytical and experimental operative conditions for the successive transformation step, the static CO_2 uptake was considered as the most reliable experiment for the calculation of the theoretical amount of CO_2 absorbed, to determine the conversions in the carbocatalytic processes.
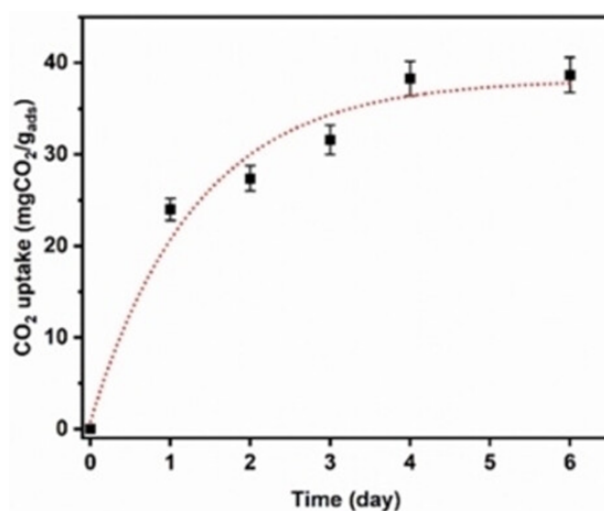
Figure 4.17: Graph of the CO_2 absorption capacity of the GO-Arg 1:5 in open air (rt) over time. The dotted red line represents the nearly exponential trend curve of the experimental data.

The combination of our previous findings focused on the nucleophilic activation of CO_2 by GO-Arg and the previously established capability of GO-Arg to effectively trap carbon dioxide, led us to test this adduct as an "on-demand" smart material for the integrated CO_2 capture and chemical conversion. In this direction, we focused our attention on the synthesis of cyclic organic carbonate via CO_2-based ring opening of epoxides as

Time CO$_2$ uptake (days)	CO$_2$ uptake (mg$_{CO_2}$/g$_{adsorber}$)[a]
1	24 ± 1.2
2	27.4 ± 1.4
3	31.6 ± 1.9
4	38.3 ± 1.9
3	38.7 ± 1.9

Table 4.7: CO$_2$ adosorption capcacity of the GO-Arg 1:5 sample left in open air (at room temperature). [a] CO$_2$ desorption measured by TG analysis after. The samples before adsorption (day 0) were subjected to a cleaning cycle at 90°C for 30 min in pure N$_2$ flux to remove any gaseous adsorbed species

benchmark reaction by using dry GO-Arg materials as an adsorbent. The synthesis of organic expoxides via CO$_2$ insertion, procedure represents an important synthetic strategy for large-scale production of long-vector organic scaffolds via a world-wide volume exceeding 100 ton/year. In this direction we set up a sequential one-pot CO$_2$ absorption – CO$_2$ conversion into cyclic carbonates always under the assistance of the GO-Arg composite.
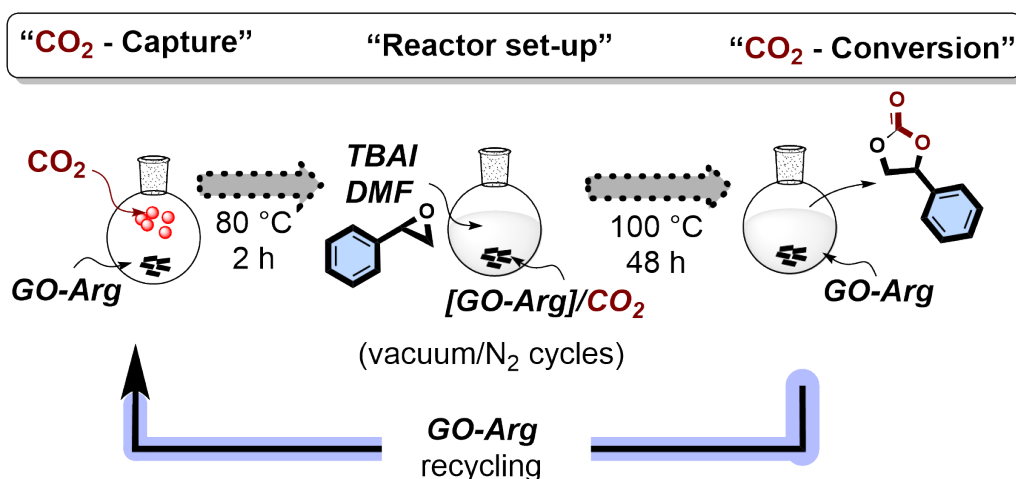
Figure 4.18: Schematic representation of the integrated an iterative "capture-CO$_2$-conversion" strategy (TBAI: tetrabutylammonium iodide). During the capture stage, GO-based materials were exposed to ∼ 0.7 mmol of CO$_2$ (99.9% purity).

In particular, an absorption period of CO$_2$ on dry GO-Arg was operated at 100°C for 2h. Then, a judicious removal of the excess of CO$_2$ was operated via consecutive N$_2$/vacuum cycles. The resulting [GO-Arg]/CO$_2$ derivative was then exposed to a solution of styrene epoxide (**1**) and TBAI in DMF under rigorous nitrogen atmosphere. Satisfyingly, under optimal conditions, the [GO-Arg]/CO$_2$ served as an effectively reservoir of activated

"solid" CO_2 enabling the effective synthesis of **2** (Fig. 4.18).

Run[a]	GO-Arg (x:x)	CO_2 adsorption parameters	CO_2 conversion parameters	Yield of **2**(%)[b]
1	1:3	60°C	Optimal	27
2	1:3	Optimal	16h	29
3	1:3	Optimal	60°C	56
4	1:1	Optimal	Optimal	60
5	1:3	Optimal	Optimal	83
6	1:5	Optimal	Optimal	86
7	1:3	24h, rt, open air	Optimal	75
8	1:3	2h, 50°C, vacuum	Optimal	20
9	1:3	Optimal	DMSO	62
10	GO	Optimal	Optimal	Traces
11	Arg	Optimal	Optimal	23[c]
12	1:3	Optimal	Optimal	NR[d]
13	//	Optimal	Optimal	NR[e]

Table 4.8: Combined trapping and carbocatalytic conversion of CO_2 by GO-Arg composites. [a] All attempts were carried out on/with a) adsorption stage: 40 mg of GO-Arg and 0.7 mmol of CO_2 (99.9% purity); b) conversion stage: 0.1 mmol of **1** (0.1 M) in reagent grade DMF. [b] Determined via ^{1}H-NMR analysis of the reaction crude by means of the internal standard methodology (mesitylene). [c] Calculated on styrene oxide as the limiting reagent. The reaction was carried out with 6 mg of Arg (estimated amount of Arg present in the GO-Arg 1:3 composite). [d] Without TBAI. [e] Without GO-Arg.

The chemical yield (internal standard on NMR crude mixture) of the final cyclic carbonate **2** was determined by considering the maximal loading of CO_2 on the GO-Arg compounds determined by thermal analysis (see Tab. 4.6) and a collection of the resulting outcomes has been reported in the Tab. 4.8. Interestingly, the previously reported GO-Arg (1:3) material proved efficiency in the two-stage one-pot approach by converting the 83% of the captured CO_2 into **2** (entry 5). As expected, the CO_2 capture/fixation performance was narrowly related to the amount of Arg present in the material. As a matter of fact, while the 1:1 adducts delivered **2** in 60% yield (entry 4), the 1:5 analogous 86% (entry 6). Always in this direction, by running the model process in the presence of only 0.1 mmol of **1** and double the quantity of GO-Arg (1:3) (simulation of higher "trapped/activated" CO2:**1** ratio) an increase on the production of **2** (93%, entry 10) was recorded.

By electing the GO-Arg (1:3) as the model material, a range of different reaction parameters (i.e. time, temperature) were also screened, (entries 1-3). However, both lower temperatures (stages 1 and 2) and shorter reaction time (stage 2) resulted in lower isolated yield of **2** than that, optimal conditions (entry 5). Moreover, based on the intriguing insights collected with the adsorption analyses carried out with air (Fig.4.17), we attempted an ICCC experiment simply exposing the GO-Arg for 24 h to a regular atmospheric mix-

ture (adsorption stage). Interestingly, the material worked smoothly also under these conditions (yield of **2**=75%), highlighting the potential applicability of the protocol towards selective CO_2 trapping/valorization of gas streams (entry 7).

To corroborate the previous result, a black experiment was performed by avoiding any CO_2 contamination of the material (entry 8). Here, a residual amount of CO_2 in the pristine GO-Arg material was recorded (yield of **2** = 20%). Furthermore, the genuine effectiveness and synergistic roles of both GO and Arg components in the sequential process was proved by running the carbonate synthesis in the presence of GO and arginine as single promoters (entries 10 and 11). Here, while commercially available GO proved to modestly activate CO_2 towards incorporation into **2**, its implementation in a sequential protocol furnished disappointing outcomes (traces of **2**, entry 10) emphasizing an unsatisfactory CO_2-trapping attitude. Interestingly, the use of unsupported arginine yielded **2** in 23% yield, proving the central role of the amino acid for the chemical activation of carbon dioxide. Finally, the synergistic action of both components GO-Arg and TBAI in promoting the ring-expansion of the epoxide (vide infra for mechanistic investigation) was stressed by the blank reactions exemplified in entries 12 and 13 in which implemented in absence of TBAI and GO-Arg respectively.

In our previous study, we postulated the covalent grafting of CO_2 on the GO-Arg surface (guanidine unit) though the formation of a carbamate group. To get more insights into this crucial aspect, XPS analyses were performed on the GO-Arg sample (GO:Arg 1:3 ratio), on the same composite upon pre-treatment for CO_2 absorption ([GO-Arg]/CO_2) and pristine GO at 100°C for 2h (for pristine GO, Tab. 5.13, Chapter 5). The resulting photoemission peaks of C_{1s}, N_{1s} and O_{1s} have been summarized in Fig. 4.19 and the Tab. 4.9 reports the binding energies and the percentages of the different contributions used to fit the photoemissions. In particular, the C_{1s} region was fitted including contributions from C=C sp^2, C-C sp^3, C-O+C-N, C-O-C, C=O+C=N, and O-C=O (for GO-Arg) and O-C=O + N-COO (for [GO-Arg]/CO_2). A contribution at lower and a peak at higher BE, account for GO defects and $\pi - \pi^*$ satellite, respectively. O_{1s} region was fitted including four contributions deriving from C=O, C-O, adsorbed water and Arg carboxylic group and N-COO group for [GO-Arg]/CO_2. The BE (530.8 eV ca.) of latter contribution agrees with previous findings and with a pure Arg sample used as reference compound. Moreover, pristine GO does not show this contribution at lower BE. It is important to note that both in C_{1s} and O_{1s} regions of [GO-Arg]/CO_2, it is not possible to distinguish the peak of the carbamate group formed after the reaction with CO_2 since its binding energy is very similar to that of the carboxylic group of Arg.
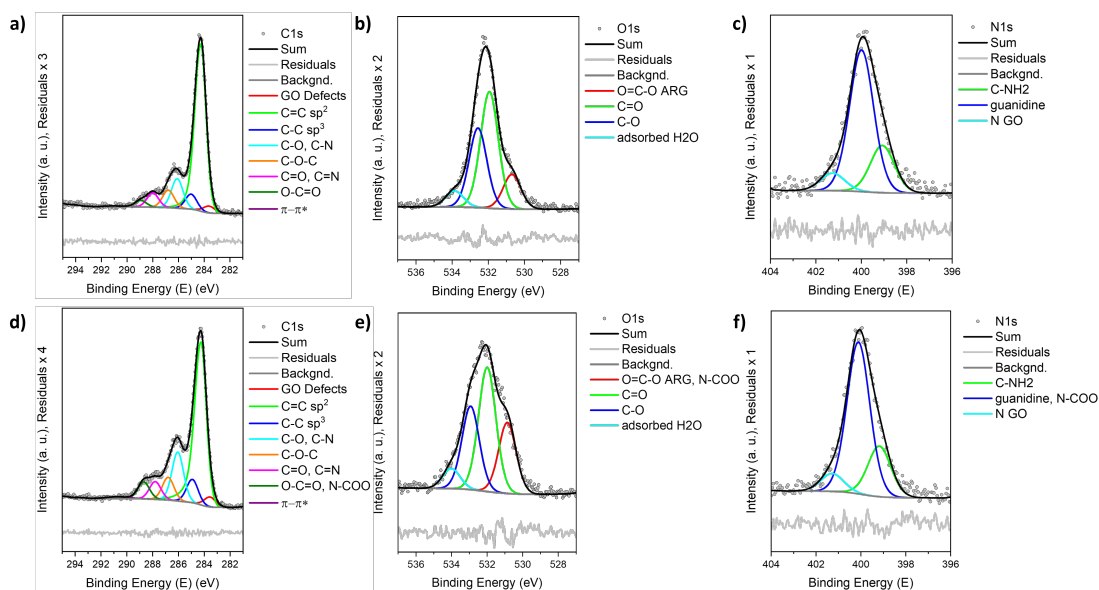
Figure 4.19: C_{1s}, O_{1s} and N_{1s} photoemission peaks and their fitting for GO-Arg (a, b, c) and for [GO-Arg]/CO_2 (d, e, f).

On the other hand, C_{1s} and O_{1s} photoemission peaks show some relevant differences looking at the relative amounts of the different contributions used to fit the raw data. In fact, O_{1s} of [GO-Arg]/CO_2 (Fig.4.19e) shows a larger amount (double) of the peak at 530.8 eV ca. attributable to the O-C=O group of Arg and to the N-COO group formed after CO_2 treatment. Also, in C_{1s} photoemission peak, the reaction with CO_2 implies a greater amount for the peak at 289 eV ca. that accounts for the O-C=O and N-COO groups (Fig.4.19d). Hence, XPS analyses strongly support the hypothesis that CO_2 is trapped by GO-Arg thanks to the formation of a carbamate group as depicted in Fig. 4.20, **Int3**. Finally, N_{1s} photoemission peak was deconvoluted using two peaks with a ratio 1:3 as previously described (C-NH_2 and guanidinium group) and a third peak at higher BE due to GO nitrogen. Here, a comparison between the sample before (Fig.4.19c) and after CO_2 treatment (Fig.4.19f) shows no appreciable differences. This is probably due to the fact that guanidinium and carbamate group have very similar BE and XPS cannot resolve the two contributions [90] [114].

GO-Arg		[GO-Arg]/CO$_2$	
BE (eV)	at. %	BE (eV)	at. %
C$_{1s}$			
283.9	2.0	283.8	2.3
284.5	47.4	284.5	39.8
285.1	4.4	285.0	5.3
286.4	8.6	286.3	11.4
287.1	6.6	287.1	5.1
288.3	4.2	288.1	4.2
289.1	1.9	288.9	3.3
291.2	0.5	291.0	0.8
O$_{1s}$			
530.7	2.5	530.8	5.1
531.9	6.0	531.9	5.9
532.7	8.2	532.9	8.9
533.9	1.2	534.0	1.4
N$_{1s}$			
399.3	1.1	399.4	1.2
400.2	3.4	400.4	3.7
401.5	0.4	401.5	0.4

Table 4.9: BE and atomic percentage of the fitted C$_{1s}$, O$_{1s}$ and N$_{1s}$ photoemission peaks.

To elucidate the details of the reaction mechanism of the CO$_2$ activation and fixation reaction on the arginine-grafted GO, we carried out QM/MM computations. In this direction, we decided to investigate the reaction mechanism of CO$_2$ activation starting from the anti-complex to the formation of the carbonate **2a** (**Pc**). Optimization of physisorbed styrene oxide, iodine and CO$_2$ molecules generated the reactant complex (**Rc**), which correspond to the asymptotic limit (**AL**) of the reaction. The PES reported in Fig. 4.20 and the representation of the critical points of the MEP (minimum energy path) are shown as insets. The overall reaction path that generates the final product can be divided into three main steps: 1) epoxide activation, 2) CO$_2$ activation, and 3) carbonate formation.

Epoxide activation. The formation of the α-iodo-alkoxide intermediate A (**INT2**) can follow either a S$_N$2 or a S$_N$1 mechanism. While the concerted mechanism requires 28.1 kcal/mol to occur, the transition state for the carbocation formation is located as 22.7 kcal/mol, suggesting that the reaction of epoxide-opening follows preferentially a S$_N$1 mechanism. The carbocation **Int1** (5.8 kcal/mol above **AL**) is generated by the opening of the styrene oxide and encountering the negative charged iodine collapses, via a barrierless process, to the stable **INT2** (-30.0 kcal/mol).

In both mechanisms (S_N2 and S_N1) the guanidinium group of the grafted arginine acts as an acid catalysis, protonating the epoxide on the styrene oxide.
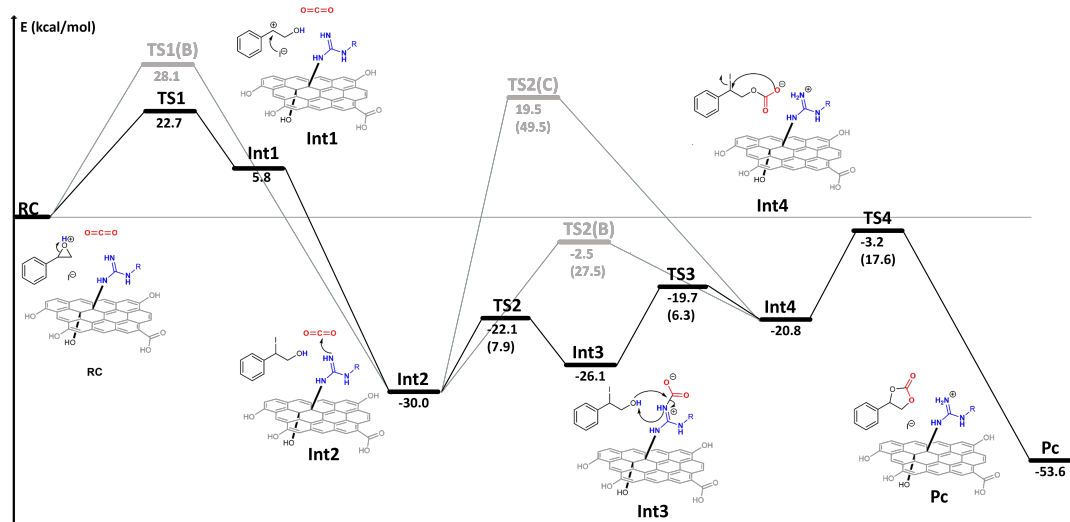
Figure 4.20: PES obtained for the CO_2 activation and fixation reaction catalyzed by arginine-grafted GO. Representation of some of the critical points obtained for the CO_2 activation and fixation, are also inserted as insets.

CO_2 activation. **Int2** can be converted into intermediate **C** (**Int4**) by distinct reactive pathways depending on the role of the guanidium group of the grafted arginine: i) an acid-base promoted mechanism, ii) an electrostatic catalysis and iii) the covalent CO2 activation.

i When the guanidium is not involved in any interaction with CO_2 (**TS2(C)**), it simply acts as a base (see Fig. 4.21), deprotonating the hydroxyl group of α-iodo-alkoxide, activating the nucleophile for the CO_2 attack. This process has an intrinsic activation barrier of 49.5 kcal/mol, i.e., 19.5 kcal/mol above **AL**.

ii In **TS2(B)** (Fig. 4.21), the guanidium interacts with CO_2 forming a salt bridge-like interaction, anchoring the carbon dioxide by forming two hydrogen bonds with its NH groups. In this geometry, CO_2 is slightly bent (O-C-O =160.5°) and more susceptible to the nucleophilic attach by the α-iodo-alkoxide: respect to **TS2(C)**, the intrinsic activation energy lowers to 27.5 kcal/mol, laying at -2.5 kcal/mol below **AL**.

iii The guanidium group can also bind carbon dioxide by forming a covalent bond. By overcoming **TS2**, which is very fast process (7.9 kcal/mol), the stable intermediate

Int3 is formed (-26.1 kcal/mol), which presents a completely formed bond between the guanidium and the CO_2 (N-C = 1.53 Å). On such intermediate, α-iodo-alkoxide easily attacks the electrophilic carbon of the activated CO_2, **TS3(C)** requiring only 6.3 $kcal/mol$ to form **Int4**.

Considering the three possible reaction mechanisms that lead to the formation of **Int4**, the guanidinium group is crucial for the formation of an activated (i.e. bent) CO_2, that can undergo α-iodo-alkoxide nucleophilic attack. This activation can take place via an electrostatic (**TS2(B)**) or a covalent (**TS2(C)**, **Int3**, **TS3**) catalysis, both performed by the presence of the guanidium group grafted onto the GO surface. Regardless the type of mechanism, concomitantly with the formation of the carbamate-like intermediate **Int4**, the catalyst is restored in its positively charged form.

Carbonate formation. The last step of the reaction mechanism foresees the intramolecular closure of the carbonate into the cyclic carbonate product **Pc**. The negatively charged portion of **Int4** attacks intramolecularly the electrophilic carbon, bearing the iodine atom, with an activation barrier of 17.6 kcal/mol, so that **TS4** results to be only 3.2 kcal/mol below **AL**. Overall, the reaction generates a highly stable product (- 53.6 kcal/mol).
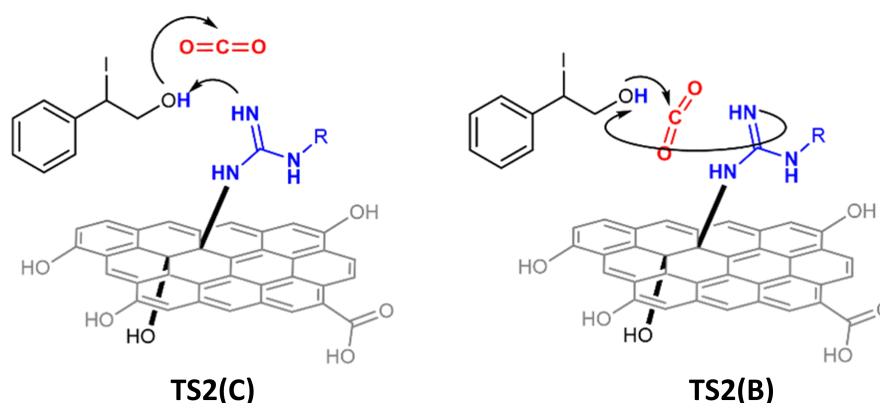
Figure 4.21: Representation of electron movement for the acid-base mechanism (**TS2(C)**) and electrostatic catalysis (**TS2(B)**).

5. Materials and Methods

General

Branched PEI (average Mw ~25,000 Da by LS, average Mn ~10,000); ethanol, 96% (EtOH); dichloromethane (DCM) were purchased from Sigma Aldrich and used without further purification. GO powder was purchased from LayerOne, Norwey. Microwave assisted reactions were performed by a CEM Matthews, NC (USA) DISCOVER-SP (Freq. 2,45 GHz; Max Pwr. 1100 W). Absorbance spectra were obtained with Carry 3500 UV-vis spectrophotometer (Agilent Technologies, Australia). Photoluminescence spectra were obtained with a LS50 spectrofluorometer (PerkinElmer, Waltham, MA, USA).

Chromatographic purification was done with 240-400 mesh silica gel. Other anhydrous solvents were supplied by Sigma Aldrich in Sureseal® bottles and used without any further purification. Commercially available chemicals were purchased from Sigma Aldrich, Stream and TCI and used without any further purification. Anhydrous DMF was purchased from Merck and used as received. All other commercially available starting materials and (non-anhydrous) solvents were purchased from Merck, TCI chemicals, Fluorochem or Alfa Aesar and were used as such without further purification. $CO_2 \geq 99.5\%$ purity, purchased from SIAD, was used in the Arg-GO CO_2 fixation.

High-resolution XPS spectra were acquired by using a Phoibos 100 hemispherical energy analyser (Specs GmbH, Berlin, Germany), equipped with Mg Ka radiation source ($\hbar\omega$ 1253.6 eV; power = 125W). Analyser were set in the Constant Analyser Energy (CAE) mode, with pass energy of 40 eV. An overall resolution of 1.5 eV was measured and the analyser was calibrated by the Ag_{3d} 5/2 (368.3 eV) and Au_{4f} 7/2 (84.0 eV) signals from freshly Ar+ sputtered samples. Charging effects were corrected by calibration of Binding Energy on C_{1s} (285.0 eV) for all spectra.

Z potential was measured in ultrapure water, using NanoBrook Omni Particle Size Analyzer Brookhaven Instruments Corporation, USA.

Elemental analysis was performed on modified GO powders by using an Elementar Unicube Elemental analyser, method GRAPHITE.

Scanning electron microscopy (SEM) analyses were performed with a ZEISS LEO 1530 FEG. The samples were deposited on a cleaned silicon wafer by dropping 100 μL of suspension at 0.1 mg/mL concentration in dimethylformamide (DMF). The energy of electrons was 5 keV and the signal was acquired using an inLens detector at a working distance of 3–5 mm.

GOPEI

Microfiltration module structure

The models used for microfiltration were: Plasmart 25, SF 0.01 m^2 (about 275 fibers), cut off 1000 KDa, pore size 100-200 nm, dead volume 2.5 mL, maximum graphene loading (LayerOne, Norwey, powder sonicated for 4 hours) estimated about 500 mg. Plasmart 100, SF 0.1 m^2, (about 850 fibers), cut off 1000 KDa, pore size 100-200 nm, dead volume 15 mL, maximum graphene loading (LayerOne, powder sonicated for 4 hours) estimated about 1.5 g. The choice was dictated by the reaction scale. For amount of initial GO lower than 1 g we used the Plasmart 25 model.
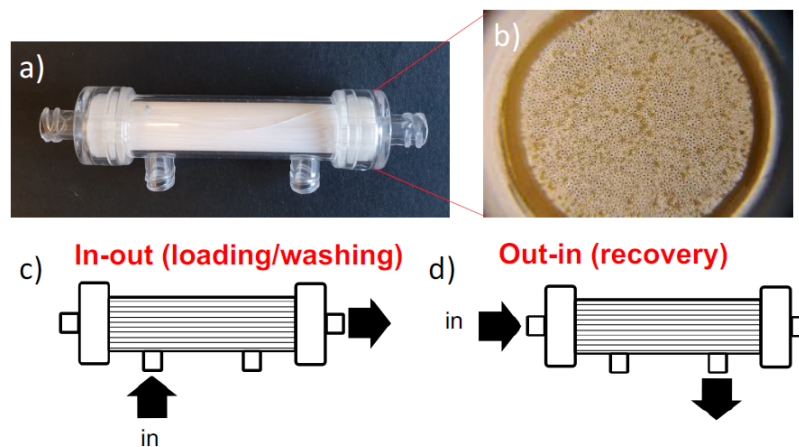
Figure 5.1: Dead-end Microfiltration and recovery procedures. **a)** image of a PES cartridge (Plasmart 25 model, 11 mm length, ϕ_{int}= 60 mm), about 275 hollow fibers, 700 mg weight (ϕ_{int}= 50 μm, ϕ_{ext}=300 μm, cut-off= 0.1-0.2 μm), **b)** zoom of the edge of the cartridge with the epoxy resin closing the interspace between the fibers, **c)** sketch of the in-out filtration mode used to load the reaction crude and to wash it and **d)** sketch of the out-in filtration mode used to recover the GO-PEI.

Synthesis of PEIdye

The thiophene dye (2,5-dioxopyrrolidin-1-yl 5'-(methylthio)-[2,2'-bithiophene]-5-carboxylate [115], 5 mg, Mw=353) was dissolved in 5 mL of DCM and added to 100 mg of PEI dissolved in 20 mL DCM at room temperature. The mixture was stirred overnight, the solvent evaporated under vacuum and the product was used without further purification.

Synthesis of GOPEIdye

GO (LayerOne, suspension 4 mg/mL, 25 mL) was dispersed in 25 mL of EtOH and the resulting mixture was sonicated for 30 min; then the PEIdye, previously synthetized, dissolved in 25 mL EtOH was added to the suspension and the mixture was irradiated with MW as for the synthesis of GOPEI and the crude purified by microfiltration (110 mg recovered). Fig. 5.2 shows the evolution of the absorbance decay in fractions eluted by the microfiltration of GOPEIdye as well as the fluorescence intensity decrease of the same fractions under UV-vis illumination. The comparison of the absorption intensity with a calibration curve of PEIdye absorption allow us to estimate a PEI loading of about 36%, in good accordance with that estimated by Cu-binding experiments and weighting of evaporated recovered PEI fractions, as described above.
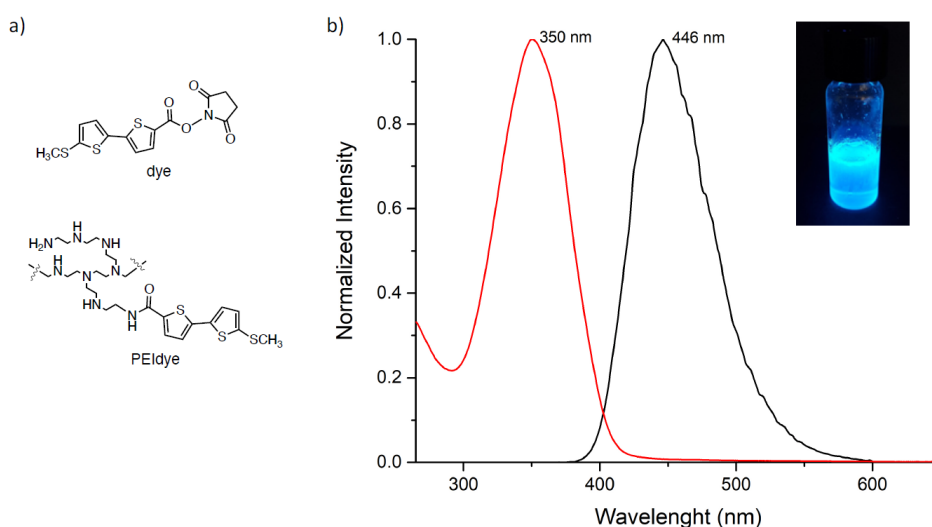
Figure 5.2: **a)** molecular structure of the thiophene dye and PEIdye, **b)** UV-vis and PL emission spectra of the PEIdye in CH$_2$Cl$_2$ (0,2 mg/ml) and image of the solution under illumination at 365 nm.

PEI loading estimation

The monitoring of PEI amount in the washing water fractions was performed by UV-vis spectroscopy after complexation with copper salts (Fig. 5.3). Briefly, a solution of copper salt was prepared dissolving 100 mg of CuCl2 in 100 mL of DI water. In parallel, a solution of PEI was prepared dissolving 20 mg of PEI in 100 mL DI water and mixed to copper solution at different ratio in order to obtain five standard solution of Cu-PEI complex and to create the calibration curve. To evaluate the amount of unreacted PEI in each fraction, 0.5 mL of eluted sample was mixed with 0.5 mL of a solution of $CuCl_2$ (concentration 1.0 mg/mL) and 2.0 mL of DI water, then the adsorption spectrum was collected.

Washing with water-ethanol of immobilized GOPEI was carried out until no (absorbance) peak at 277 nm (ascribed to PEI-Cu complex, Fig. 5.3) was observed. Then by collecting the eluted fraction, complexing them as described above, and using a calibration curve (R2= 0,99985) it was possible to estimate a PEI loading of about 40%. This value was confirmed also by weighting the evaporated recovered PEI fractions. In parallel, we also estimate the evolution of the purification and the PEI loading by monitoring the evolution of the fluorescence intensity which decrease of the eluted fractions during the microfiltration under UV-vis illumination as well as the absorbance decay of the same fractions (Fig. 5.4b). The comparison of the absorption intensity with a calibration curve of PEIdye absorption allow us to estimate a PEI loading of about 37%, in good accordance with that estimated by Cu-binding experiments. A total volume of water required for complete removal of PEIdye of about 2.8 L/g of GOPEIdye (crude of reaction).
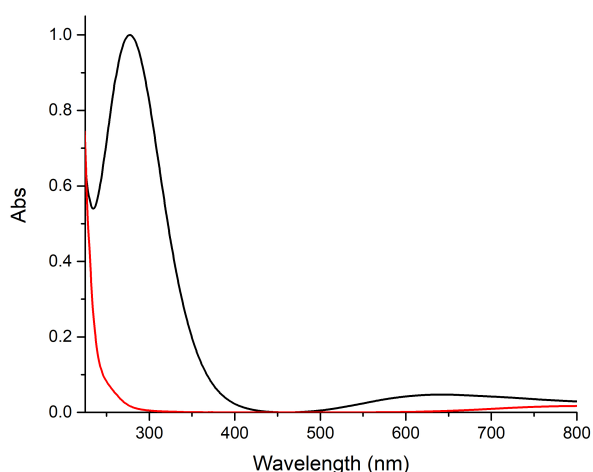
Figure 5.3: Absorbance spectra of Cu-PEI (black line) and CuCl2 (red line).
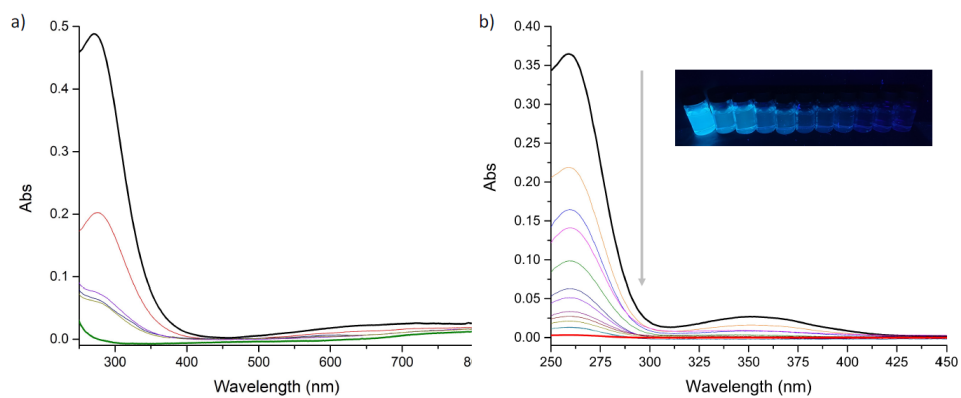
Figure 5.4: **a)** UV-vis absorption spectra of eluted fractions upon Cu complexation. **b)** UV-vis absorption spectra of the eluted fractions. (Black line: first fraction; Red line: last fraction).

Thermal Gravimetric Analysis

GOPEI profile displays a weight loss of ca. 20% in the range of 150–300 °C caused by decomposition of oxygen functional groups of GO [116]. The weight loss of about 35% in the range 250°C-350°C is typical of PEI thermal degradation [74]. This value is in good accordance with the PEI loading estimated by microfiltration post experiments and XPS data.
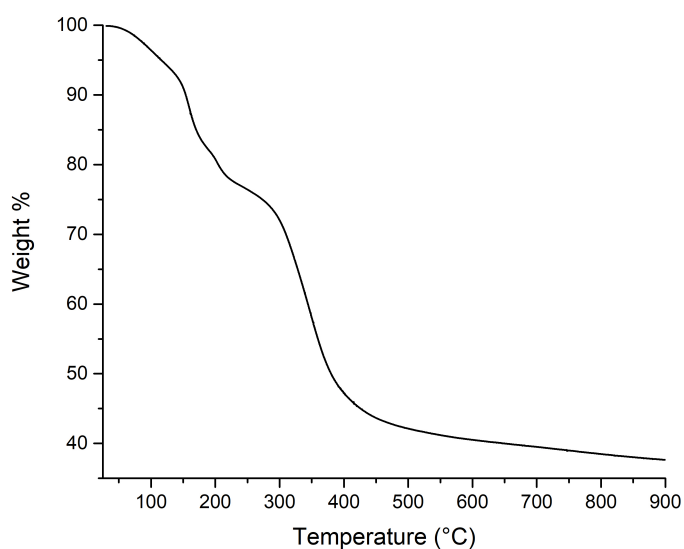
Figure 5.5: TGA profile of GOPEI.

ATR-FTIR spectroscopy
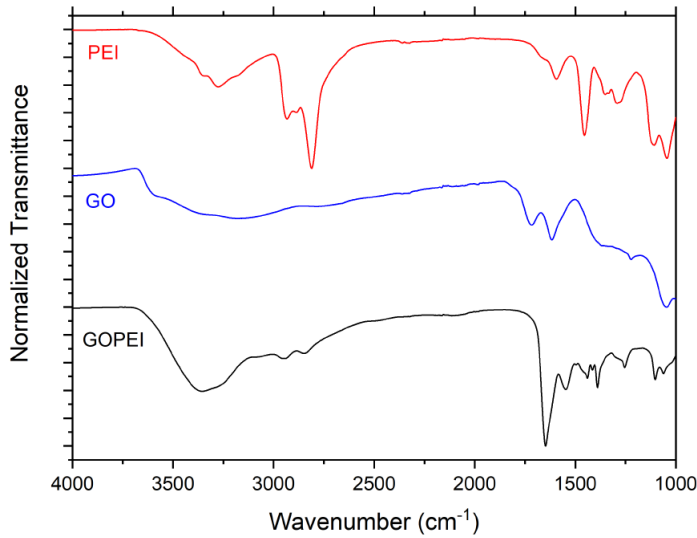
Figure 5.6: ATR-FTIR spectra of GO, PEI and GOPEI.

X-Ray Photoelectron spectroscopy (XPS)

XPS samples were prepared by fixing the tablets prepared from the dry powders of each material on the sample, holed by conductive carbon tape. Base pressure in the analysis chamber during analysis was maintained at 10^{-9} mbar. Data analysis and fitting were performed with CasaXPS software, after Shirley background subtraction.

	C_{1s}	O_{1s}	N_{1s}	S_{2p} S-O	Si_{2p} Si-O	Cl_{2p}
Binding Energy (eV)	285.0	531	401	168	101	196.9
GO	69.1±0.9	27.8±0.6	0.9±0.1	1.2±0.1	0.3±0.1	0.8±0.1
GO-PEI	71.2±0.9	13.4±0.4	10.4±0.5	0.4±0.1	3.1±0.3	1.5±0.2

Table 5.1: Binding energy and atomic percentage of GO, and GOPEI.

X-Ray Diffraction (XRD)
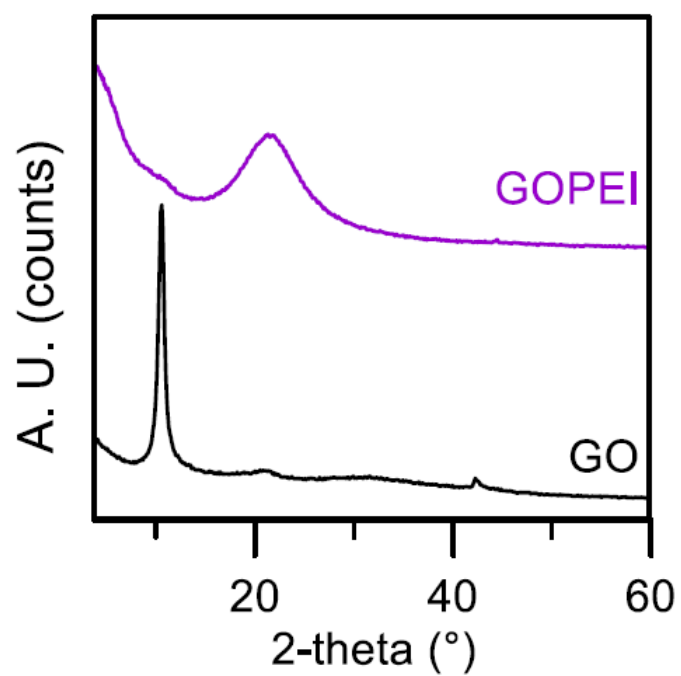
Figure 5.7: XRD profiles of GO and GOPEI powders.

Aminoacids

Synthesis

A basic solution of amino acid (L-Lysine, L-glutamic acid or L-methionine methyl ester) was prepared by adding 930 mg of amino acid and 381 mg of NaOH to ultrapure water (13 mL). The solution was then added to 62 mL of GO suspension (5 mg/mL in ultrapure water, sonicated for 2 h). The mixture was irradiated with microwaves for 3 h (Tmax = 80 °C; Pmax = 120 W), and then 5 mL of EtOH was added. The crude was purified by microfiltration on commercial Versatile PES modules, (Plasmart 100 module, Medica s.p.a.) according to previously reported conditions. A total volume of about 2 L of water was required to purify the crude obtained by using 0.5 g of GO as a starting material. The control material, GO-NaOH, was prepared by performing the same reaction but without the addition of the amino acids. 270 mg of GO-Lys, 263 mg of GO-Met and 260 mg of GO-Glu were obtained after purification.

Characterization

Material	N/C	S/C	O/C
GO	0.01	0.014	0.38
GO-NaOH	0.003	//	0.36
GO-Lys	0.04	//	0.14
GO-Glu	0.009	//	0.26
GO-Met	0.003	0.01	0.19

Table 5.2: Atomic ratios of modified GO compounds obtained by XPS.

Amino Acid	Formula	H/C	N/C	S/C	O/C
Lys	$C_6H_{14}N_2O_2$	2.5 (2.3)	0.33(0.33)	<0.001	0.43 (0.33)
Glu	$NaC_5H_8NO_4$	2.0 (1.6)	0.2 (0.2)	<0.002	1.01 (0.8)
Met	$C_6H_{13}NO_2S$	2.4 (2.7)	0.17 (0.17)	0.17 (0.17)	0.43 (0.33)

Table 5.3: Atomic ratios of amino acids obtained by elemental analysis. Expected values between parentheses.

Material	H/C	N/C	S/C	O/C
GO	0.71	0.002	0.01	0.77
GO–NaOH	1.07	0.001	0.003	0.92
GO–Lys	0.96	0.06	//	0.62
GO–Glut	0.95	0.008	//	0.67
GO–Met	0.74	0.02	0.012	0.49

Table 5.4: Atomic ratios of modified GO materials obtained by elemental analysis.

Adsorption selectivity and kinetic experiments

A stock solution of eight emerging contaminants (CAF, OFLOX, BP4, CBZ, BPA, RhB, DCF, BP3) at 10 mg/L each was prepared in tap water. In a typical experiment, 25 mg of tested adsorbents (GO-Lys, GO-Glu and GO-Met) were sonicated for 2 h in 5 mL of ultrapure water. After that time, 5 mL of the stock solution described above was added, to reach a final concentration of 5 mg/L for each contaminant. The solutions were gently stirred in the dark for 1 h, 4 h, and 24 h and then centrifuged at 15000 rpm for 10 min. GO, GONaOH, and rGO were tested under the same conditions.

High performance liquid chromatography (HPLC-UV VIS)

Analyses of the treated water samples were performed by HPLC on a Dyonex Ultimate 3000 system equipped with a diode array detector. 0.5 mL samples were used as sources for the automated injection. The chromatographic separation was performed on a reverse phase analytical column (Agilent Eclipse XDB-C8 4.6 × 150 mm, 5 μm) at a flow rate of 1.0 mL/min, linear gradient TFA 0.05% aqueous solution/ acetonitrile from 80 : 20 to 0 : 100, detection at λ_{max} of each analyte. In the case of the adsorption experiments on the selected emerging contaminants in the mixture, the percentage removal of the analytes was determined by comparison with that of the initial untreated solution. The results are expressed as the mean of two independent experiments ±SD.

Recyclable GO-Arginine Hybrids for CO_2 Fixation into Cyclic Carbonates

Starting materials **1a**, **1g**, **1h**, **1l**, and **1m** are commercially available: these were purchased from Merck and used as received. Starting materials **1b**, **1c**, **1d**, **1e**, **1f**, **1i**, **1j**, and **1k** were synthesized through Corey-Chaykovsky epoxidation starting from the respective benzaldehydes, following an unmodified literature procedure [117]. Spectral data match with the ones reported. Starting materials **1n** and **1o** were synthesized through m-CPBA epoxidation of the corresponding olefins following an unmodified literature procedure [118]. Spectral data match with the ones reported.

Synthesis and purification of GO-Arg

A basic solution of L-Arginine (i.e. L-Arg) was prepared by adding 6.0 g of L-Arg (34.4 mmol) and 1.05 g of NaOH (26.3 mmol) in ultra pure water (50 mL). The solution was then added to 400 mL of GO suspension (5 mg/mL in ultra pure water, sonicated for 2 h). The mixture was kept under stirring and at 80 °C for 24 h then 5 mL of EtOH were added. The crude product was purified by MF (Plasmart 100, Medica SpA) in loop filtration modality by using a peristaltic pump at 100 mL/min. Pure water was progressively added to the feed solution (tot. volume= 3.2 L). The process was stopped when a neutral pH was measured in the permeated water. 2.3 g of GO-Arg were obtained after freeze drying.

Synthesis and purification of GO-5a

Graphene oxide (LayerOne (S-126/36)), was homogeneously dispersed in 40 mL of distilled water through sonication for 2 h to prepare GO aqueous suspensions (5 mg/mL). Then 60 mg of n-pentylguanidine and 210 mg of NaOH were dissolved in 10 mL (6 mg/mL for n-pentylguanidine; 21 mg/mL for NaOH) of ultra pure water. These two dispersions were mixed, and the solution was kept under stirring at 80 °C for 24 h. Once the reaction was completed the crude was purified by centrifugation and dried by freeze drying.

XPS-analyses

The pristine GO presents C_{1s} (285.0 eV), O_{1s} (532.6 eV), N_{1s} (401.5 eV), Cl_{2p} (200.2 eV) and S_{2p} (168.6 eV) signals. GO-Arg present a significantly higher amount of N respect to the pristine GO. The overall oxidation (O_{1s}/C_{1s}) was lower than GO due to the presence of aliphatic chains of Arginine. The presence of Ca_{2p} (347.5 eV) in the Arg-GO and GO-**5a** can be ascribed to the presence of Ca ions in the washing water used during purification. The parameters used for the fitting of C_{1s} and N_{1s} signal are reported in more details

in our previous work.[8] Pure L-Arginine presents roughly the expected atomic composition (C:N:O = 6:4:2), moreover, the C_{1s} deconvolution is in good agreement with the data reported in literature, along with the main position of N_{1s} signal at 400.0 eV. The deconvolution of N_{1s} core level signal reported in Figure 2 of L-Arginine (and GO-Arg) is based on literature results (the Artemenko et al. work cited in main text) that associated to L-Arginine two components at 399.3 (NH_2 and C=NH) and 400.0 eV (C-NH-C and $C=NH_2^+$). The binding energies of L-Arginine obtained in our fit was found slightly shifted to higher binding energies respect to the literature (c.a. +0.5 eV), such mismatch is compatible with C=C sp2 and C-C sp3 relative shift, as a matter of fact, these two carbons are the main one in GO and L-Arginine respectively, thus it is probably due to the selection of C 1s calibration value: we have chosen 285.0 eV for GO, that is a compromise between 284.6 eV of C=C sp2 and 285.4 eV for C-C sp3 (red and green peak in Figure S3a), than we calibrated GO-Arg in the same way, given the similar sp2-sp3 amounts. The calibration of L-Arginine was chosen as 285.4 eV in accordance with C-C sp3 peaks in GO and GO-Arg calibration but was slightly different from the one reported in literature (285.0 eV). 1s – C1s (400-285.4=114.6eV) and O 1s - N 1s (531.4-400=131.4 eV)) relative shifts are the same of those reported in literature (399.5-285=114.6 eV and 530.8-399.5=131.3eV) and it is above the aim of these paper to provide an absolute XPS reference values for pristine L-Arginine.
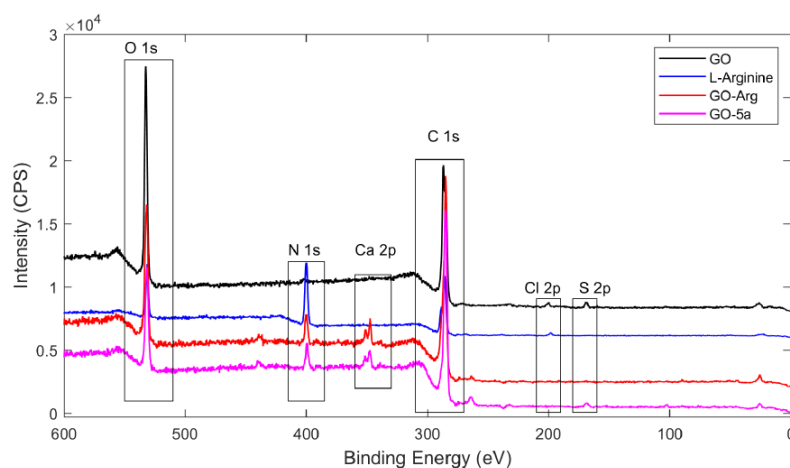
Figure 5.8: Survey spectra of graphene oxide (black line), L-Arginine (blue line), GO-Arg (red line) and GO-**5a** (magenta line).

Materials	C	O	N	Cl	S	Ca
GO	70.4	27	0.7	0.8	1.0	_
Arginine	58.4	13.7	27.0	0.9	_	_
GO-Arg	73.6	19.6	4.9	< 0.2	< 0.2	1.8
GO-**5a**	79.1	14.7	3.5	< 0.2	0.9	1.7

Table 5.5: XPS atomic composition.
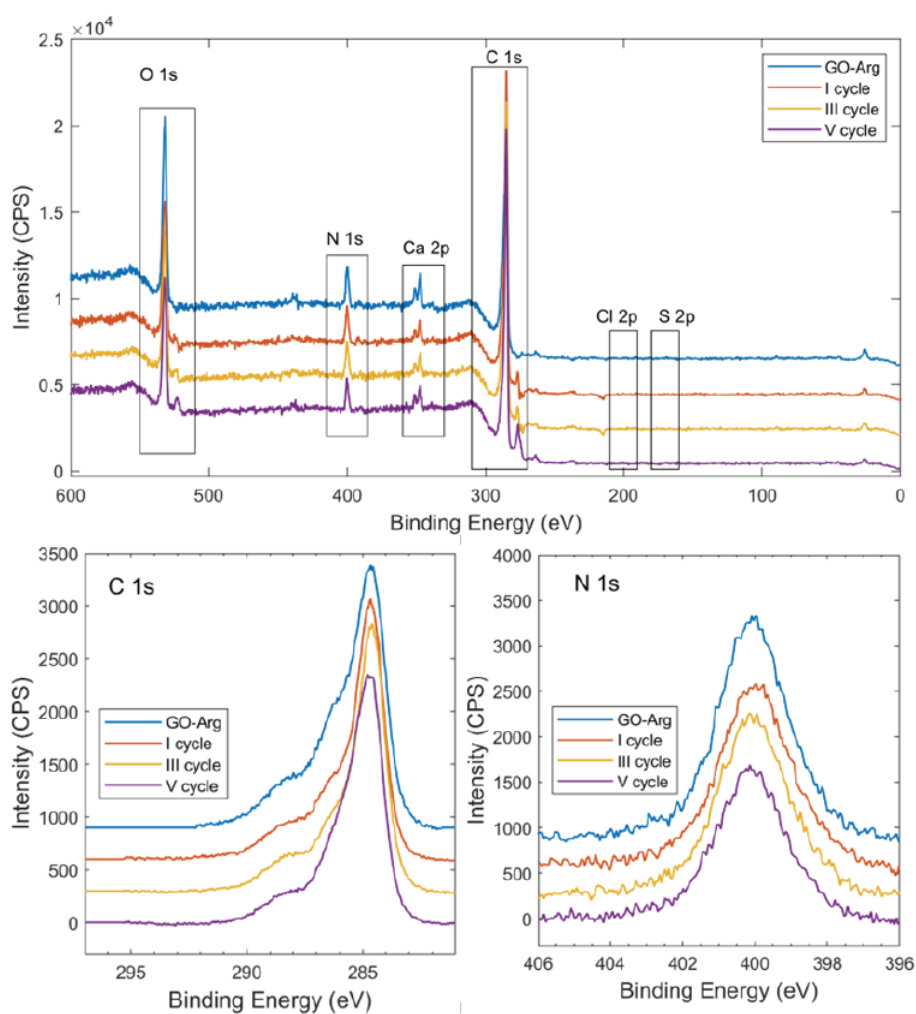
Figure 5.9: **Top**: Survey spectra of pristine GO-Arg and GO-Arg after 1, 3 and 5 cycle of catalysis. **Bottom**: C_{1s} and N_{1s}.
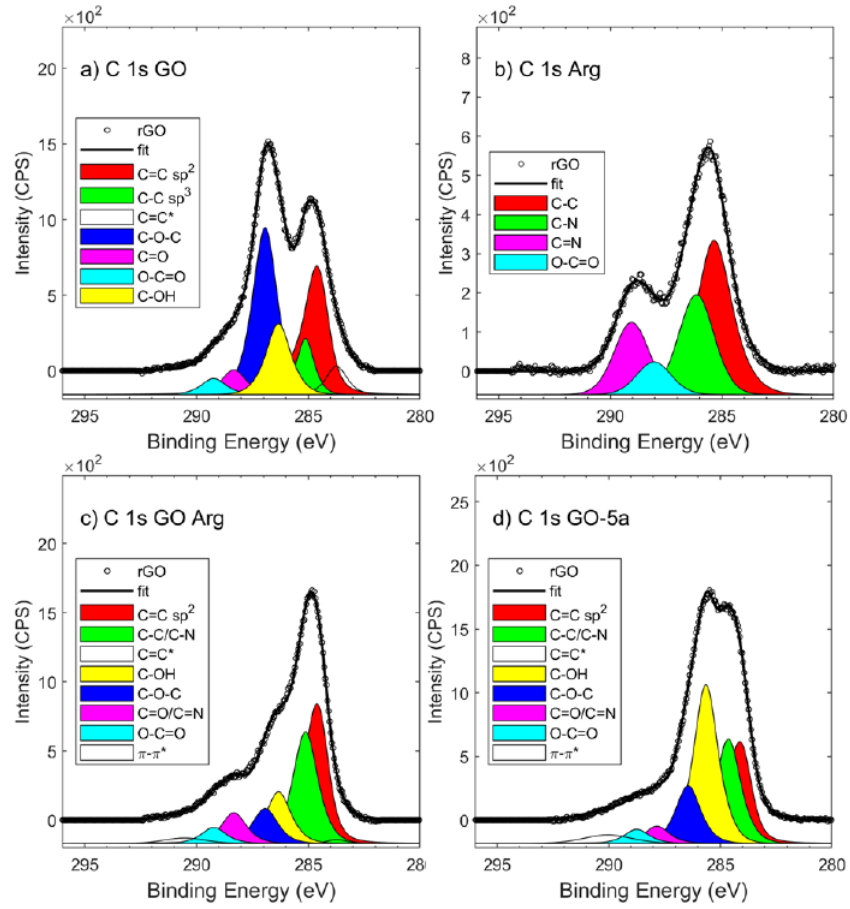
Figure 5.10: C_{1s} deconvolution of **a)** graphene oxide, **b)** Arginine, **c)** GO-Arg and **d)** GO-**5a**.

Material	C_{1s} Deconvolution						
	Csp^2	Csp^3	C=C*	C-OH	C-O-C	C=O	O-C=O
GO	31.2	7.9	4.8	14.3	33.7	5.0	3.2
GO-Arg pristine	39.8	27.1	0.7	12.6	8.5	7.5	3.8
GO-Arg I Cycle	68.4	8.7	0.6	7.8	5.3	6.4	2.8
GO-Arg III Cycle	67.6	10.5	0.6	7.6	4.5	6.4	2.8
GO-Arg V Cycle	50.8	24.0	0.4	12.9	3.0	6.2	2.8

Table 5.6: C_{1s} deconvolution of GO, GO-Arg and GO-Arg after several cycle.

Kinetic Profile
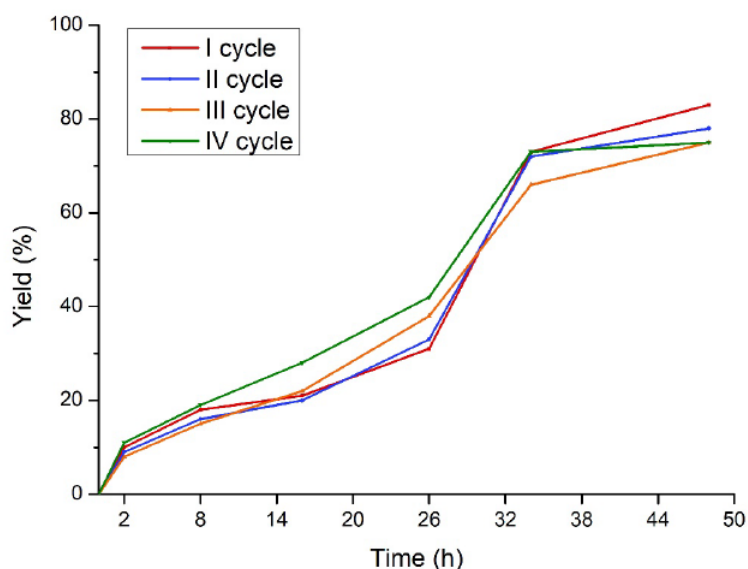
Figure 5.11: Kinetic profile of the reaction.

General procedure for the Arg-GO catalyzed CO_2 fixation.

In a heat-gun dried screw-capped Schlenk flask, equipped with a magnetic stirring bar and under N_2 atmosphere, Arg-GO (5.0 mg) was added. The tube was evacuated and backfilled with CO_2 (three times). Anhydrous DMF (1.0 mL) was then added and bubbled for 1 minute under a flow of CO_2. Then, **1** (0.2 mmol, 1 equiv.) and TBAI (22.0 mg, 0.06 mmol, 30 mol%) were added. The tube was then sealed and placed in an oil bath at 100 °C where it was vigorously stirred for 48 h. After cooling to room temperature, the reaction mixture was filtered through a Celite pad to remove Arg-GO, washing with EtOAc (3 x 5 mL). The solvents were removed under reduced pressure (rotary evaporator then high-vacuum pump to remove DMF) and the residue was purified by flash column chromatography (FC) on silica gel (nhexane/ EtOAc mixtures) to afford pure products **2**. NOTE: Products **2l** and **2m** were found to be somewhat volatile and loss of material was observed during evaporation of DMF under high vacuum. Thus, the work-up was adjusted by DMF removal through aqueous extraction (3 x 20 mL) followed by careful evaporation of EtOAc under reduced pressure and flash chromatography. All of the characterization of the obtained products are reported in [109].

General procedure for the GO-5a catalyzed CO_2 fixation

In a heat-gun dried screw-capped Schlenk flask, equipped with a magnetic stirring bar and under N_2 atmosphere, GO-**5a** (5.0 mg) was added. The tube was evacuated and backfilled with CO_2 (three times). Anhydrous DMF (1.0 mL) was then added and bubbled for 1 minute under a flow of CO_2. Then, **1** (0.2 mmol, 1 equiv.) and TBAI (22.0 mg, 0.06 mmol, 30 mol%) were added. The tube was then sealed and placed in an oil bath at 100 °C where it was vigorously stirred for 48 h. After cooling to room temperature, the reaction mixture was filtered through a Celite pad to remove GO-**5a**, washing with EtOAc (3 x 5 mL). The solvents were removed under reduced pressure (rotary evaporator then high-vacuum pump to remove DMF) and the residue was purified by flash column chromatography (FC) on silica gel (n-hexane/EtOAc mixtures) to afford pure product **2a**.

General procedure for the recovering/reuse test

Recycling experiments were conducted similarly to the previously mentioned reactions. After the completion of each reaction cycle, the mixture was centrifuged with EtOAc, to separate the product from the catalyst. Then, GO-Arg was washed through reiterative centrifugation with DMF (removal of TBAI), and freeze dried, after which it was ready to be re-utilized. A total of 5 consecutive recycling runs were conducted.

GO-Arg catalyzed CO_2 fixation on enantiopure 1a

In a heat-gun dried screw-capped Schlenk flask, equipped with a magnetic stirring bar and under N_2 atmosphere, GO-Arg (15.0 mg) was added. The tube was evacuated and backfilled with CO_2 (three times). Anhydrous DMF (1.0 mL) was then added and bubbled for 1 minute under a flow of CO_2. Then, **1a** (0.6 mmol, 1 equiv.) and TBAI (66.0 mg, 0.18 mmol, 30 mol%) were added. The tube was then sealed and placed in an oil bath at 100 °C where it was vigorously stirred for 48 h. After cooling to room temperature, the reaction mixture was filtered through a Celite pad to remove the catalyst and the enantiomeric excess of **2a** was determined by chiral HPLC measurement using HPLC with chiral column (ChiralCel OD, 10% IPA/nHex, $1\ mL/min$, 25 °C). Racemization tests were carried out by stirring enantiopure (S)-**1a** in DMF at 100 °C with the desired additive (i.e. TBAI, GO-Arg and TBAI/GO-Arg). The enantiomeric excess of the resulting **1a** was determined via chiral HPLC on one aliquot of solution upon cooling at rt. (ChiralPak AD, 2% IPA/nHex, 1 mL/min, 25 °C).

General procedure for the hot filtration test

In a heat-gun dried screw-capped Schlenk flask, equipped with a magnetic stirring bar and under N_2 atmosphere, Arg-GO (5.0 mg) was added. The tube was evacuated and backfilled with CO_2 (three times). Anhydrous DMF (1.0 mL) was then added and bubbled for 1 minute under a flow of CO_2. Then, **1** (0.2 mmol, 1 equiv.) and TBAI (22.0 mg, 0.06 mmol, 30 mol%) were added. The tube was then sealed and placed in an oil bath at 100 °C where it was vigorously stirred for 16 h. Then the reaction mixture was filtered, without cooling, through a Celite pad to remove the catalyst. A small amount of the filtered solution was analysed by ^{1}H-NMR, observing a conversion of 37%, while the remaining was placed again in the oil bath at 100 °C in a new heat-gun dried screw-capped Schlenk flask for further 16h. After cooling to room temperature, the DMF was removed with a high-vacuum pump and the residue was analysed with ^{1}H-NMR using an internal standard, observing a conversion of 36%, so no progressing formation of carbonate occurred.

Graphene Oxide-Arginine Composites: Efficient Materials for Integrated CO_2 Capture and Conversion - ICCC

The CO_2 adsorption/desorption capability of samples was determined via Thermogravimetric Analysis (TGA, STA449 F3 Jupiter Thermo-Microbalance, Netzsch-Gerätebau). The samples, weighed into a Al_2O_3 crucible, were subjected to an initial cleaning cycle at 90°C for 30 min (heating rate: 10 $°C/min$) in a high-purity nitrogen atmosphere (99.999%, 250 mL/min) before the absorption of CO_2. A 100 minutes-long CO_2 isothermal adsorption cycle under a CO_2/N_2 mixture (1:2 % v/v, 185 mL/min) was set after cooling sample at 40°C (cooling rate: 1 $°C/min$, N_2). Finally, the temperature was increased to 90°C (heating rate: 10 $°C/min$) in pure N_2 for the final desorption step. In addition to the single-cycle measurements (i.e., absorption/desorption), five-cycles processes were also carried out to determine the cyclability of the samples. By measuring the mass change during the TGA analysis, CO_2 uptake values were calculated and expressed as $mg_{CO_2}/g_{adsorbent}$.

Synthesis and purification of the materials

Initially, 100 mg of graphene oxide (Abalonyx (S-126/36)) is uniformly dispersed in 80 mL of distilled water through sonication for 2 hours to obtain an aqueous suspension of GO (5 mg/mL). Subsequently, a variable ratio of L-arginine (100, 300, or 500 mg) and 420 mg of NaOH is dissolved in 20 mL (21 mg/mL for NaOH) of distilled water. The two dispersions are mixed together, and the solution is refluxed at 80 °C for 24 hours. When the reaction is complete, the crude mixture is purified by centrifugation (9000 RPM), 15 minutes each time, with tap water until the supernatant solution reaches a neutral pH. The product is washed with a total of $2L/g$ of H_2O. Finally, the purified product is lyophilized.

XPS-analyses

The parameters used for the fitting of C_{1s} and N_{1s} signal are reported in more details below.

The following X-ray photoelectron spectroscopy (XPS) measurements were performed with a Thermo Scientific ESCALAB QXi spectrometer employing a monochromatic Al Kα X-ray source (1486.6 eV) operating at 15 kV and 200 W, a concentric hemispherical analyser, and a spot size of 400 μm × 200 μm. The pressure in the analysis chamber was better than 10^{-7} mbar. Few mg of sample powder were mounted with a double adhesive conductive carbon tape on a sample holder grounded to the instrument. Charge compensation was applied by beams of combined low energy ion (Ar$^+$) and electron beams. Survey scans were measured in a binding energy range of 0–1350 eV with a constant pass energy of 100 eV, at 1.0 eV/step, with a dwell time of 50 ms, accumulating 3 scans. High-resolution spectra were recorded using a constant pass energy (3 eV for C_{1s} and 10 eV for O_{1s} and N_{1s}), at 0.05 eV/step, with a dwell time of 100 ms, accumulating 5 scans for each element. The high-resolution XPS spectra were used for assessment of the elemental state as well as for quantification using the sensitivity factors provided by the manufacturer by means of the Avantage software and after background correction with the smart-background function implemented in the same software. Peak fittings were performed in the framework of the Avantage software after background correction with the smart-background function implemented in the same software using pseudo-Voigt functions for the synthetic peaks. In the C_{1s} photoemission peak generated from graphene oxide, the asymmetric tail of the sp^2 carbon forms a pseudo-background that superimposes to the signal from carbon species bound to oxygen and nitrogen (laying in the range 285-290 eV). Hence, a meaningful fit must consider in a complementary way the C_{1s}, O_{1s} and N_{1s} peaks by comparing the atomic percentages of the C bound to O and C bound to N moieties present in the three peaks. The asymmetric tail of the sp^2 carbon have been modelled in order to have a maximum mismatch of 1 at. % among the total carbon bound to oxygen and nitrogen from C_{1s} and the sum of oxygen bound to carbon from O_{1s} and the nitrogen bound to carbon from N_{1s}. Full details of peak fitting are given in their relative table.

Name	Peak BE (eV)	Area	FWHM (eV)	L/G Mix %Product	Tail Mix (%)	Tail Height (%)	Tail Exponent
C_{1s} Defect	283.9	100.45	1.1	30	100	0	0
	283.5 : 283.9		K * 1	K*1	Fixed	Fixed	Fixed
C_{1s} Graphite	284.5	2457.22	0.97	30	45	0	0.09
	284.2 : 284.6		0.7 : 1.1	FIxed	Fixed	Fixed	Fixed
C_{1s} C-C	285.1	221.22	1.1	30	100	0	0
	284.7 : 285.3		0.8 : 1.2	Fixed	Fixed	Fixed	Fixed
C_{1s} C-O, C-N	286.4	433.7	1.1	30	100	0	0
	286.0 : 286.5		K*1	K*1	Fixed	Fixed	Fixed
C_{1s} C-O-C	287.1	257.58	1.1	30	100	0	0
	286.6 : 287.2		K*1	K*1	Fixed	Fixed	Fixed
C_{1s} C=O, C=N	288.3	209.81	1.1	30	100	0	0
	287.8 : 288.4		K*1	K*1	Fixed	Fixed	Fixed
C_{1s} O-C=O	289.1	95.87	1.1	30	100	0	0
	288.6 : 290.0		K*1	K*1	Fixed	Fixed	Fixed
C_{1s} Satellite	291.2	24.68	1.91	30	100	0	0
	290.7 : 291.3		1.0 : 2.3	K*1	Fixed	Fixed	Fixed

Table 5.7: Fitting parameters for C_{1s} of sample GO-Arg.

Name	Peak BE (eV)	Area	FWHM (eV)	L/G Mix %Product	Tail Mix (%)	Tail Height (%)	Tail Exponent
C_{1s} Defect	283.9	122.59	1.1	30	100	0	0
	283.5 : 283.9		K * 1	K*1	Fixed	Fixed	Fixed
C_{1s} Graphite	284.5	2156.88	0.99	30	45	0	0.09
	284.2 : 284.6		0.7 : 1.1	FIxed	Fixed	Fixed	Fixed
C_{1s} C-C	285.0	286.23	1.1	30	100	0	0
	284.7 : 285.2		0.8 : 1.2	Fixed	Fixed	Fixed	Fixed
C_{1s} C-O, C-N	286.3	599.53	1.1	30	100	0	0
	286.0 : 286.5		K*1	K*1	Fixed	Fixed	Fixed
C_{1s} C-O-C	287.1	278.45	1.1	30	100	0	0
	286.6 : 287.2		K*1	K*1	Fixed	Fixed	Fixed
C_{1s} C=O, C=N	288.1	217.91	1.1	30	100	0	0
	287.8 : 288.4		K*1	K*1	Fixed	Fixed	Fixed
C_{1s} O-C=O, N-COO	288.1	207.89	1.1	30	100	0	0
	288.6 : 290.0		K*1	K*1	Fixed	Fixed	Fixed
C_{1s} Satellite	291.2	45.41	2.12	30	100	0	0
	290.7 : 291.3		1.0 : 2.3	K*1	Fixed	Fixed	Fixed

Table 5.8: Fitting parameters for C_{1s} of sample [GO-Arg]/CO_2.

Name	Peak BE (eV)	Area	FWHM (eV)	L/G Mix %Product	Tail Mix (%)	Tail Height (%)	Tail Exponent
C=O	532	13841.98	1.2	30	100	0	0
			0.8 : 1.2	Fixed	Fixed	Fixed	Fixed
O=C-O Arg	530.7	4215.05	1.2	30	100	0	0
			I*1	I*1	Fixed	Fixed	Fixed
C-O	532.6	10362.74	1.2	30	100	0	0
			I*1	I*1	Fixed	Fixed	Fixed
Adsorbed H_2O	533.9	2063.98	1.2	30	100	0	0
			I*1	I*1			

Table 5.9: Fitting parameters for O_{1s} of sample GO-Arg.

Name	Peak BE (eV)	Area	FWHM (eV)	L/G Mix %Product	Tail Mix (%)	Tail Height (%)	Tail Exponent
C=O	531.9	8458.98	1.2	30	100	0	0
			0.8 : 1.2	Fixed	Fixed	Fixed	Fixed
O=C-O Arg	530.8	4834.3	1.2	30	100	0	0
			I*1	I*1	Fixed	Fixed	Fixed
C-O	532.9	5679.17	1.2	30	100	0	0
			I*1	I*1	Fixed	Fixed	Fixed
Adsorbed H_2O	534.0	1364.86	1.2	30	100	0	0
			I*1	I*1			

Table 5.10: Fitting parameters for O_{1s} of sample [GO-Arg]/CO_2.

Name	Peak BE (eV)	Area	FWHM (eV)	L/G Mix %Product	Tail Mix (%)	Tail Height (%)	Tail Exponent
C-NH_2	399.3	913.95	1.3	30	100	0	0
			0.7 : 1.3	Fixed	Fixed	Fixed	Fixed
N in GO	401.5	341.14	1.3	30	100	0	0
			I*1	0.7 : 1.3	Fixed	Fixed	Fixed
Guanidinium	400.2	2741.84	1.3	30	100	0	0
			I*1	Fixed	Fixed	Fixed	Fixed

Table 5.11: Fitting parameters for N_{1s} of sample GO-Arg.

Name	Peak BE (eV)	Area	FWHM (eV)	L/G Mix %Product	Tail Mix (%)	Tail Height (%)	Tail Exponent
C-NH_2	399.4	1015.07	1.25	30	100	0	0
			0.7 : 1.25	Fixed	Fixed	Fixed	Fixed
N in GO	401.5	362.03	1.3	30	100	0	0
			I*1	0.7 : 1.3	Fixed	Fixed	Fixed
Guanidinium	400.4	3045.22	1.25	30	100	0	0
			I*1	Fixed	Fixed	Fixed	Fixed

Table 5.12: Fitting parameters for N_{1s} of sample [GO-Arg]/CO_2.

	BE (eV)	at. %
C_{1s}		
defects	283.7	4.8
C=C	284.5	22.4
C-C	285.1	2.1
C-O, C-N	286.4	20.8
C-O-C	287.0	7.7
C=O, C=N	288.1	4.0
O-C=O	289.1	2.0
$\pi - \pi^*$	290.9	0.9
O_{1s}		
C-O	532.0	20.5
C=O, C-O-C	532.6	14.3
N_{1s}		
N in GO	401.5	0.5

Table 5.13: BE and atomic percentage of the fitted C_{1s}, O_{1s} and N_{1s} photoemission peaks for pristine GO.

CO_2 fixation experiments

General procedure of CO_2 fixation

In a vacuum-dried and nitrogen-filled Schlenk flask, 40 mg of one of the materials is added. The nitrogen flow is switched to a CO2 flow, by performing 3 cycles of vacuum-CO_2, and the dry material is allowed to stir in a CO_2 atmosphere for 2 hours at 100°C. Then, the Schlenk flask is simply opened and left under nitrogen at room temperature before adding the reagents for carbocatalysis: 1 mL of anhydrous DMF, 12.5 μL of compound 1 (0.01 mmol), and 37 mg of TBAI (0.01 mmol). The reaction is carried out at 100°C. After 48 hours, the reaction mixture is filtered through cotton with celite, washed with ethyl acetate, and dried. Any remaining DMF is removed using a high-vacuum pump. An NMR analysis is performed on the crude mixture, and the yield of the reaction is calculated using an internal standard (4.4 mg of ethylene carbonate - 9.3 μL of mesitylene – 3.6 mg of dimethyl sulphone). Product **2** was purified by flash column chromatography (FC) on silica gel (nHex/EtOAc mixtures=2:1).
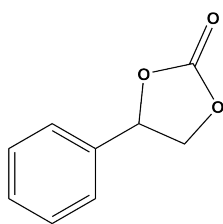
2. White solid. FC eluent: nHex/EtOAc: 2:1. ^{1}H-NMR (400 MHz, CDCl$_3$) δ=7.49–7.39 (m, 3H), 7.38–7.33 (m, 2H), 5.68 (t, J=8.0 Hz, 1H), 4.80 (t, J=8.4 Hz, 1H), 4.34 (dd, J=8.6, 7.8 Hz, 1H);
^{13}C NMR (101 MHz, CDCl$_3$) δ 154.9, 136.9, 135.9, 129.8, 129.3, 125.9, 78.1, 71.3.

General procedure for recovery of the GO-Arg

Recycling experiments were conducted similarly to the previously mentioned reactions. After the completion of each reaction cycle, the mixture was centrifuged several times with EtOAc, to separate the product, the DMF and TBAI from the material. Then, the material was washed one final time with DI water and freeze dried, after which it was ready to be re-utilized.

General procedure for atmospheric CO$_2$ adsorption experiment

40 mg of GO-Arg (1:3) was left exposed to the air overnight. The next morning the material was transferred in to a Schlenk flask. The atmosphere inside the vessel was changed with nitrogen and the reagents for carbocatalysis were added (1 mL of anhydrous DMF, 0.01 mmol of compound 1 and 0.01 mmol of TBAI). The reaction was carried out at 100 °C for 48 hours. After that, the reaction mixture is filtered through cotton with celite, washed with ethyl acetate, and dried. Any remaining DMF is removed using a high-vacuum pump. An NMR analysis is performed on the crude mixture, and the yield of the reaction is calculated using an internal standard (4.4 mg of ethylene carbonate - 9.3 μL of mesitylene – 3.6 mg of dimethyl sulphone). Product **2** was purified by flash column chromatography (FC) on silica gel (nHex/EtOAc mixtures=2:1). In parallel, the same amount of the same material was left under vacuum at 50 °C overnight. The next morning the material was transferred in to a Schlenk flask, treated and then used as motioned before.

Thermal Analysis

6. Conclusion

In this thesis we reported several modification of graphene oxide (GO) and their application in different fields.

In Chapter 4.1, we reported the synthesis of GOPEI nanosheets, a fast and easy scalable procedure involving MW assisted amination of GO and purification through hollow fiber membrane modules by microfiltration, not requiring tedious and time consuming reiterated washing-centrifugation steps. The hollow fibers filter here proposed allowed to retain GOPEI nanosheets, wash and recover them by flow direction inversion. This procedure minimizes the work-up steps generally required for modified GO purification and ensures high purity reproducibility, thanks to the standard and commercial availability of the cartridges. Altogether, these peculiarities make the MF method highly suitable for future modified-GO upscaling for real exploitation in practical applications including drinking water purification requiring high and reproducible purity. The adsorption properties of GOPEI towards two dangerous metal contaminants, lead cations and arsenic anions simultaneously, were also demonstrated. Different from unmodified GO, GOPEI nanosheets adsorbed both As and Pb ions with a removal rate higher than 90%. This was ascribed to the combined positive surface charge (promoting As interactions) and primary amine promoted complexation of Pb ions.

In Chapter 4.2, we reported the functionalization of graphene oxide (GO) with L-Lysine, L-glutamic acid and L-methionine by a fast and efficient microwave-assisted protocol. Furthermore, we improved the previously reported worked up protocol based on microfiltration on commercial modules. The synthetic approach allowed high purity of the reaction products, with a high batch to batch reproducibility, thanks to the standard microfiltration module features. Furthermore, the improved microfiltration allowed to accelerate further the purification process compared to the standard reiterated washing-centrifugation-separation method while using less water for gram of crude utilized. Structure analysis revealed amino acid loadings in the range of 5–15%, with partial reduction of GO (from 27% down to 14–20% of oxygen). Adsorption of a mixture of eight contaminants in tap water was studied for amino acid-modified GOs and compared to unmodified GO and rGO. As a further control sample, we considered also GO subjected to the reaction

conditions but treated in the absence of any amino acid, called GO-NaOH. This systematic study allowed us to unambiguously unravel the role of the amino acid binding in the adsorption properties of GO.

The removal of most of the targeted contaminants occurred in the first hour of treatment, with a significant improvement of the removal of BPA, CBZ, and BP4 observed for the modified materials. Adsorption isotherms show that the Langmuir model describes the adsorption mechanism better than the BET model, except for the pairs BP4–GO-Glu, BP4–GO, and BPA–GO. In addition, the maximum adsorption capacities (Qm) for the amino acid modified GOs were found to be in the range of 77–292 mg/g for BP4, 147–295 mg/g for BPA, and 121–172 mg/g for CBZ, with GO-Lys expressing the best performance in each case. This results, at the moment of publication were on par or even better the maximum adsorption capacity reported in literature of the same molecules on carbon sorbents, such as activated carbon [119], carbon nanotubes [120], graphene base adsorbent [121] [122] and related materials [123] [124]. Qm was found to be strictly dependent on the amino acid loading, which suggests an active role in the removal of contaminant molecules by the grafting procedure.

Accordingly, molecular dynamics simulations revealed higher interaction energies for amino acid-modified GOs rather than unmodified GO, which may be ascribed to the higher van der Waals and hydrophobic interactions between the amino acid hydrophobic chain and the contaminant molecules.

In Chapter 4.3, we documented a convenient synthesis of GO-Arginine hybrids to be implemented in the valorization of CO_2 into cyclic carbonates. A range of aliphatic as well as aromatic carbonates were successfully isolated in good yield (up to 85%) under relatively mild conditions. The robustness of the arginine-containing GO was proved by reiterative runs and by spectroscopic analysis on the recovered materials. Dedicated control experiments gave insight into the key role of the guanidine group both as a tagging unit and a CO_2 activator. Additionally, the observed partial racemization when using enantiopure starting material styrene oxide (S)-**1a** implies an epoxide ring-opening step at the more substituted site of the oxirane through a sequence of partial S_N1-type events. Studies towards the implementation of these preliminary findings into CO_2-capture-and-utilization (CCU) modalities are currently under way in our laboratory and will be presented in due course.

In Chapter 4.3.2 we focused on the application of this material in an ICCC (Integrated CO_2 Capture and Conversion) process. It has been demonstrated that the material is able to capture CO_2 both from high purity atmospheres but also from low concentration mixtures (such as atmospheric one) and to convert it when exposed to dedicated reaction conditions (i.e. synthesis of cyclic carbonates). The entire process has been completely studied and rationalized using chemical-physical, spectroscopic (XPS, BET, TGA, ect), and dedicated computational analyses.

Bibliography

[1] B. Brodie, "Note sur un nouveau procédé pour la purification et la désagrégation du graphite," *Ann. Chim. Phys*, vol. 45, pp. 351–353, 1855.

[2] B. C. Brodie, "XIII. On the atomic weight of graphite," *Philosophical transactions of the Royal Society of London*, no. 149, pp. 249–259, 1859.

[3] F. Gottschalk, "Beitràge zur kenntniss der graphitsäure," *Journal fùr Praktische Chemie*, vol. 95, no. 1, pp. 321–350, 1865.

[4] M. Berthelot, "Recherches sur les états du carbone," *Ann. Chim. Phys.*, vol. 19, pp. 392–417, 1870.

[5] G. Charpy, "Sur la formation de l'oxyde graphitique et la dèfinition du graphite," *CR Hebd. Seances Acad. Sci*, vol. 148, no. 5, pp. 920–923, 1909.

[6] H. P. Boehm, M. Eckel, and W. Scholz, "Untersuchungen am graphitoxid v. Über den bildungsmechanismus des graphitoxids," *Zeitschrift für anorganische und allgemeine Chemie*, vol. 353, no. 5-6, pp. 236–242, 1967.

[7] U. Hofmann and A. Frenzel, "Quellung von graphit und die bildung von graphitsäure," *Berichte der deutschen chemischen Gesellschaft (A and B Series)*, vol. 63, no. 5, pp. 1248–1262, 1930.

[8] L. Staudenmaier, "Verfahren zur darstellung der graphitsäure," *Berichte der deutschen chemischen Gesellschaft*, vol. 31, no. 2, pp. 1481–1487, 1898.

[9] W. S. Hummers and R. E. Offeman, "Preparation of Graphitic Oxide," *Journal of the American Chemical Society*, vol. 80, pp. 1339–1339, Mar. 1958.

[10] H. Thiele, "Graphit und Graphitsäure," *Zeitschrift für anorganische und allgemeine Chemie*, vol. 190, no. 1, pp. 145–160, 1930.

[11] T. Nakajima and Y. Matsuo, "Formation process and structure of graphite oxide," *Carbon*, vol. 32, no. 3, pp. 469–475, 1994.

[12] T. Nakajima, A. Mabuchi, and R. Hagiwara, "A new structure model of graphite oxide," *Carbon*, vol. 26, no. 3, pp. 357–361, 1988.

[13] U. Hofmann, "Über graphitsäure und die bei ihrer zersetzung entstehenden kohlenstoffarten," *Berichte der deutschen chemischen Gesellschaft (A and B Series)*, vol. 61, no. 2, pp. 435–441, 1928.

[14] U. Hofmann, A. Frenzel, and E. Csalán, "Die konstitution der graphitsäure und ihre reaktionen," *Justus Liebigs Annalen der Chemie*, vol. 510, no. 1, pp. 1–41, 1934.

[15] M. Mermoux and Y. Chabre, "Formation of graphite oxide," *Synthetic metals*, vol. 34, no. 1-3, pp. 157–162, 1989.

[16] M. Mermoux, Y. Chabre, and A. Rousseau, "FTIR and ^{13}C NMR study of graphite oxide," *Carbon*, vol. 29, no. 3, pp. 469–474, 1991.

[17] A. M. Dimiev and S. Eigler, eds., *Graphene Oxide*. Wiley, sep 2016.

[18] A. Lerf, H. He, M. Forster, and J. Klinowski, "Structure of Graphite Oxide revisited," *The Journal of Physical Chemistry B*, vol. 102, pp. 4477–4482, may 1998.

[19] H.-P. Boehm, "Graphene—How a laboratory curiosity suddenly became extremely interesting," *Angewandte Chemie International Edition*, vol. 49, no. 49, pp. 9332–9335, 2010.

[20] A. K. Geim and K. S. Novoselov, "The rise of graphene," *Nature Materials*, vol. 6, pp. 183–191, mar 2007.

[21] S. F. Kiew, L. V. Kiew, H. B. Lee, T. Imae, and L. Y. Chung, "Assessing biocompatibility of graphene oxide-based nanocarriers: A review," *Journal of Controlled Release*, vol. 226, pp. 217–228, mar 2016.

[22] V. Georgakilas, J. N. Tiwari, K. C. Kemp, J. A. Perman, A. B. Bourlinos, K. S. Kim, and R. Zboril, "Noncovalent functionalization of graphene and graphene oxide for energy materials, biosensing, catalytic, and biomedical applications," *Chemical Reviews*, vol. 116, pp. 5464–5519, mar 2016.

[23] R. J. Young, I. A. Kinloch, L. Gong, and K. S. Novoselov, "The mechanics of graphene nanocomposites: A review," *Composites Science and Technology*, vol. 72, pp. 1459–1476, jul 2012.

[24] J. Xu, Y. Wang, and S. Hu, "Nanocomposites of graphene and graphene oxides: Synthesis, molecular functionalization and application in electrochemical sensors and biosensors. a review," *Microchimica Acta*, vol. 184, pp. 1–44, nov 2016.

[25] R. Joshi, S. Alwarappan, M. Yoshimura, V. Sahajwalla, and Y. Nishina, "Graphene oxide: the new membrane material," *Applied Materials Today*, vol. 1, pp. 1–12, nov 2015.

[26] P. L. Yap, M. J. Nine, K. Hassan, T. T. Tung, D. N. H. Tran, and D. Losic, "Graphene-based sorbents for multipollutants removal in water: A review of recent progress," *Advanced Functional Materials*, vol. 31, dec 2020.

[27] I. A. Vacchi, C. Spinato, J. Raya, A. Bianco, and C. Ménard-Moyon, "Chemical reactivity of graphene oxide towards amines elucidated by solid-state NMR," *Nanoscale*, vol. 8, no. 28, pp. 13714–13721, 2016.

[28] S. Guo, Y. Nishina, A. Bianco, and C. Ménard-Moyon, "A flexible method for covalent double functionalization of graphene oxide," *Angewandte Chemie International Edition*, vol. 59, pp. 1542–1547, dec 2019.

[29] S. Eigler, Y. Hu, Y. Ishii, and A. Hirsch, "Controlled functionalization of graphene oxide with sodium azide," *Nanoscale*, vol. 5, no. 24, p. 12136, 2013.

[30] M.-C. Hsiao, S.-H. Liao, M.-Y. Yen, P.-I. Liu, N.-W. Pu, C.-A. Wang, and C.-C. M. Ma, "Preparation of covalently functionalized graphene using residual oxygen-containing functional groups," *ACS Applied Materials and Interfaces*, vol. 2, pp. 3092–3099, oct 2010.

[31] H. Yang, C. Shan, F. Li, D. Han, Q. Zhang, and L. Niu, "Covalent functionalization of polydisperse chemically-converted graphene sheets with amine-terminated ionic liquid," *Chemical Communications*, no. 26, p. 3880, 2009.

[32] X. Zhang, Y. Huang, Y. Wang, Y. Ma, Z. Liu, and Y. Chen, "Synthesis and characterization of a graphene-C_{60} hybrid material," *Carbon*, vol. 47, pp. 334–337, jan 2009.

[33] Y. Xu, Z. Liu, X. Zhang, Y. Wang, J. Tian, Y. Huang, Y. Ma, X. Zhang, and Y. Chen, "A graphene hybrid material covalently functionalized with porphyrin: Synthesis and optical limiting property," *Advanced Materials*, vol. 21, pp. 1275–1279, mar 2009.

[34] Z. Liu, J. T. Robinson, X. Sun, and H. Dai, "PEGylated nanographene oxide for delivery of water-insoluble cancer drugs," *Journal of the American Chemical Society*, vol. 130, pp. 10876–10877, jul 2008.

[35] J. Xu, M. Xu, J. Wu, H. Wu, W.-H. Zhang, and Y.-X. Li, "Graphene oxide immobilized with ionic liquids: facile preparation and efficient catalysis for solvent-free cycloaddition of CO_2 to propylene carbonate," *RSC Advances*, vol. 5, no. 88, pp. 72361–72368, 2015.

[36] I. E. M. Carpio, J. D. Mangadlao, H. N. Nguyen, R. C. Advincula, and D. F. Rodrigues, "Graphene oxide functionalized with ethylenediamine triacetic acid for heavy metal adsorption and anti-microbial applications," *Carbon*, vol. 77, pp. 289–301, oct 2014.

[37] T. Gao, H. Wu, L. Tao, L. Qu, and C. Li, "Enhanced stability and separation efficiency of graphene oxide membranes in organic solvent nanofiltration," *Journal of Materials Chemistry A*, vol. 6, no. 40, pp. 19563–19569, 2018.

[38] G. Srinivas, J. W. Burress, J. Ford, and T. Yildirim, "Porous graphene oxide frameworks: Synthesis and gas sorption properties," *Journal of Materials Chemistry*, vol. 21, no. 30, p. 11323, 2011.

[39] E. Pourazadi, E. Haque, W. Zhang, A. T. Harris, and A. I. Minett, "Synergistically enhanced electrochemical (ORR) activity of graphene oxide using boronic acid as an interlayer spacer," *Chemical Communications*, vol. 49, no. 94, p. 11068, 2013.

[40] T. Szabó, O. Berkesi, and I. Dékány, "DRIFT study of deuterium-exchanged graphite oxide," *Carbon*, vol. 43, no. 15, pp. 3186–3189, 2005.

[41] F. Farivar, P. L. Yap, K. Hassan, T. T. Tung, D. N. Tran, A. J. Pollard, and D. Losic, "Unlocking thermogravimetric analysis (TGA) in the fight against 'Fake graphene' materials," *Carbon*, vol. 179, pp. 505–513, jul 2021.

[42] F. Farivar, P. L. Yap, R. U. Karunagaran, and D. Losic, "Thermogravimetric analysis (TGA) of graphene materials: Effect of particle size of graphene, graphene oxide and graphite on thermal parameters," *C*, vol. 7, p. 41, apr 2021.

[43] T. Kuila, S. Bose, A. K. Mishra, P. Khanra, N. H. Kim, and J. H. Lee, "Chemical functionalization of graphene and its applications," *Progress in Materials Science*, vol. 57, pp. 1061–1105, sep 2012.

[44] J. W. Kim, D. Kang, T. H. Kim, S. G. Lee, N. Byun, D. W. Lee, B. H. Seo, R. S. Ruoff, and H. S. Shin, "Mosaic-like monolayer of graphene oxide sheets decorated with tetrabutylammonium ions," *ACS Nano*, vol. 7, pp. 8082–8088, aug 2013.

[45] M. C. Biesinger, B. P. Payne, A. P. Grosvenor, L. W. Lau, A. R. Gerson, and R. S. Smart, "Resolving surface chemical states in XPS analysis of first row transition metals, oxides and hydroxides: Cr, Mn, Fe, Co and Ni," *Applied Surface Science*, vol. 257, pp. 2717–2730, jan 2011.

[46] L. Stobinski, B. Lesiak, A. Malolepszy, M. Mazurkiewicz, B. Mierzwa, J. Zemek, P. Jiricek, and I. Bieloshapka, "Graphene oxide and reduced graphene oxide studied by the XRD, TEM and electron spectroscopy methods," *Journal of Electron Spectroscopy and Related Phenomena*, vol. 195, pp. 145–154, aug 2014.

[47] A. Kovtun, D. Jones, S. Dell'Elce, E. Treossi, A. Liscio, and V. Palermo, "Accurate chemical analysis of oxygenated graphene-based materials using X-ray photoelectron spectroscopy," *Carbon*, vol. 143, pp. 268–275, mar 2019.

[48] A. Ganguly, S. Sharma, P. Papakonstantinou, and J. Hamilton, "Probing the thermal deoxygenation of graphene oxide using high-resolution in situ X-ray-based spectroscopies," *The Journal of Physical Chemistry C*, vol. 115, pp. 17009–17019, aug 2011.

[49] R. Larciprete, S. Fabris, T. Sun, P. Lacovig, A. Baraldi, and S. Lizzit, "Dual path mechanism in the thermal reduction of graphene oxide," *Journal of the American Chemical Society*, vol. 133, pp. 17315–17321, sep 2011.

[50] R. Benoit, "XPS chemical data."

[51] A. Barinov, O. B. Malcioğlu, S. Fabris, T. Sun, L. Gregoratti, M. Dalmiglio, and M. Kiskinova, "Initial stages of oxidation on graphitic surfaces: Photoemission study and density functional theory calculations," *The Journal of Physical Chemistry C*, vol. 113, pp. 9009–9013, apr 2009.

[52] P. Wick, A. E. Louw-Gaume, M. Kucki, H. F. Krug, K. Kostarelos, B. Fadeel, K. A. Dawson, A. Salvati, E. Vázquez, L. Ballerini, M. Tretiach, F. Benfenati, E. Flahaut, L. Gauthier, M. Prato, and A. Bianco, "Classification framework for graphene-based materials," *Angewandte Chemie International Edition*, vol. 53, pp. 7714–7718, jun 2014.

[53] A. Bianco, H.-M. Cheng, T. Enoki, Y. Gogotsi, R. H. Hurt, N. Koratkar, T. Kyotani, M. Monthioux, C. R. Park, J. M. Tascon, and J. Zhang, "All in the graphene family – a recommended nomenclature for two-dimensional carbon materials," *Carbon*, vol. 65, pp. 1–6, dec 2013.

[54] E. Commission, "Drinking water directive," 2017.

[55] A. Malakar, B. Das, S. Islam, C. Meneghini, G. D. Giudici, M. Merlini, Y. V. Kolen'ko, A. Iadecola, G. Aquilanti, S. Acharya, and S. Ray, "Efficient artificial mineralization route to decontaminate arsenic(III) polluted water - the tooeleite way," *Scientific Reports*, vol. 6, May 2016.

[56] P. Smedley and D. Kinniburgh, "A review of the source, behaviour and distribution of arsenic in natural waters," *Applied Geochemistry*, vol. 17, pp. 517–568, May 2002.

[57] G. Ersan, O. G. Apul, F. Perreault, and T. Karanfil, "Adsorption of organic contaminants by graphene nanosheets: A review," *Water Research*, vol. 126, pp. 385–398, Dec. 2017.

[58] R. Mailler, J. Gasperi, Y. Coquet, S. Deshayes, S. Zedek, C. Cren-Olivé, N. Cartiser, V. Eudes, A. Bressy, E. Caupos, R. Moilleron, G. Chebbo, and V. Rocher, "Study of a large scale powdered activated carbon pilot: Removals of a wide range of emerging and priority micropollutants from wastewater treatment plant effluents," *Water Research*, vol. 72, pp. 315–330, apr 2015.

[59] S. Khaliha, D. Jones, A. Kovtun, M. L. Navacchia, M. Zambianchi, M. Melucci, and V. Palermo, "The removal efficiency of emerging organic contaminants, heavy metals and dyes: intrinsic limits at low concentrations," *Environmental Science: Water Research and Technology*, vol. 9, no. 6, pp. 1558–1565, 2023.

[60] C. J. Madadrang, H. Y. Kim, G. Gao, N. Wang, J. Zhu, H. Feng, M. Gorring, M. L. Kasner, and S. Hou, "Adsorption behavior of edta-graphene oxide for pb(II) removal," *ACS Applied Materials Interfaces*, vol. 4, pp. 1186–1193, Feb. 2012.

[61] Y. Shen and B. Chen, "Sulfonated graphene nanosheets as a superb adsorbent for various environmental pollutants in water," *Environmental Science and Technology*, vol. 49, pp. 7364–7372, June 2015.

[62] C.-Z. Zhang, Y. Yuan, and Z. Guo, "Experimental study on functional graphene oxide containing many primary amino groups fast-adsorbing heavy metal ions and adsorption mechanism," *Separation Science and Technology*, vol. 53, pp. 1666–1677, Feb. 2018.

[63] D. Dinda, A. Gupta, and S. K. Saha, "Removal of toxic Cr(vi) by UV-active functionalized graphene oxide for water purification," *Journal of Materials Chemistry A*, vol. 1, no. 37, p. 11221, 2013.

[64] C. Liu, D. Zhang, L. Zhao, X. Lu, P. Zhang, S. He, G. Hu, and X. Tang, "Synthesis of a thiacalix[4]arenetetrasulfonate-functionalized reduced graphene oxide adsorbent for the removal of lead(II) and cadmium(II) from aqueous solutions," *RSC Advances*, vol. 6, no. 114, pp. 113352–113365, 2016.

[65] Z. Shao and H. Zhang, "Combining transition metal catalysis and organocatalysis: a broad new concept for catalysis," *Chemical Society Reviews*, vol. 38, no. 9, p. 2745, 2009.

[66] Z. Du and Z. Shao, "Combining transition metal catalysis and organocatalysis – an update," *Chem. Soc. Rev.*, vol. 42, no. 3, pp. 1337–1378, 2013.

[67] S. Navalon, A. Dhakshinamoorthy, M. Alvaro, and H. Garcia, "Carbocatalysis by graphene-based materials," *Chemical Reviews*, vol. 114, pp. 6179–6212, May 2014.

[68] D. Haag and H. H. Kung, "Metal free graphene based catalysts: A review," *Topics in Catalysis*, vol. 57, pp. 762–773, Nov 2013.

[69] Y. Pan, S. Wang, C. W. Kee, E. Dubuisson, Y. Yang, K. P. Loh, and C.-H. Tan, "Graphene oxide and rose bengal: oxidative C-H functionalization of tertiary amines using visible light," *Green Chemistry*, vol. 13, no. 12, p. 3341, 2011.

[70] Y. Kim, S. Some, and H. Lee, "Graphene oxide as a recyclable phase transfer catalyst," *Chemical Communications*, vol. 49, no. 50, p. 5702, 2013.

[71] D. R. Dreyer, K. A. Jarvis, P. J. Ferreira, and C. W. Bielawski, "Graphite oxide as a dehydrative polymerization catalyst: A one-step synthesis of carbon-reinforced poly(phenylene methylene) composites," *Macromolecules*, vol. 44, pp. 7659–7667, sep 2011.

[72] D. R. Dreyer, K. A. Jarvis, P. J. Ferreira, and C. W. Bielawski, "Graphite oxide as a carbocatalyst for the preparation of fullerene-reinforced polyester and polyamide nanocomposites," *Polymer Chemistry*, vol. 3, no. 3, p. 757, 2012.

[73] M. Zhang, K. Guan, Y. Ji, G. Liu, W. Jin, and N. Xu, "Controllable ion transport by surface-charged graphene oxide membrane," *Nature Communications*, vol. 10, Mar. 2019.

[74] D. Pakulski, W. Czep, S. Witomska, A. Aliprandi, P. Pawluc, V. Patroniak, A. Ciesielski, and P. Samori, "Graphene oxide-branched polyethylenimine foams for efficient removal of toxic cations from water," *Journal of Materials Chemistry A*, vol. 6, no. 20, pp. 9384–9390, 2018.

[75] S. Deng, G. Zhang, S. Chen, Y. Xue, Z. Du, and P. Wang, "Rapid and effective preparation of a (HPEI) modified biosorbent based on cellulose fiber with a microwave irradiation method for enhanced arsenic removal in water," *Journal of Materials Chemistry A*, vol. 4, no. 41, pp. 15851–15860, 2016.

[76] S. Mantovani, S. Khaliha, L. Favaretto, C. Bettini, A. Bianchi, A. Kovtun, M. Zambianchi, M. Gazzano, B. Casentini, V. Palermo, and M. Melucci, "Scalable synthesis and purification of functionalized graphene nanosheets for water remediation," *Chemical Communications*, vol. 57, no. 31, pp. 3765–3768, 2021.

[77] M. ping Wei, H. Chai, Y. li Cao, and D. zeng Jia, "Sulfonated graphene oxide as an adsorbent for removal of Pb^{2+} and methylene blue," *Journal of Colloid and Interface Science*, vol. 524, pp. 297–305, aug 2018.

[78] J. D. Ziebarth and Y. Wang, "Understanding the protonation behavior of linear polyethylenimine in solutions through monte carlo simulations," *Biomacromolecules*, vol. 11, pp. 29–38, dec 2009.

[79] A. Sherlala, A. Raman, M. Bello, and A. Asghar, "A review of the applications of organo-functionalized magnetic graphene oxide nanocomposites for heavy metal adsorption," *Chemosphere*, vol. 193, pp. 1004–1017, feb 2018.

[80] A. O. Abdelhalim, V. V. Sharoyko, A. A. Meshcheriakov, M. D. Luttsev, A. A. Potanin, N. R. Iamalova, E. E. Zakharov, S. V. Ageev, A. V. Petrov, L. V. Vasina, I. L. Solovtsova, A. V. Nashchekin, I. V. Murin, and K. N. Semenov, "Synthesis, characterisation and biocompatibility of graphene–l-methionine nanomaterial," *Journal of Molecular Liquids*, vol. 314, p. 113605, sep 2020.

[81] H. Ge and W. Zou, "Preparation and characterization of L-glutamic acid-functionalized graphene oxide for adsorption of Pb(II)," *Journal of Dispersion Science and Technology*, vol. 38, pp. 241–247, mar 2016.

[82] S. Yadav, A. Asthana, A. K. Singh, R. Chakraborty, S. Vidya, A. Singh, and S. A. C. Carabineiro, "Methionine-functionalized graphene oxide/sodium alginate bio-polymer nanocomposite hydrogel beads: Synthesis, isotherm and kinetic studies for an adsorptive removal of fluoroquinolone antibiotics," *Nanomaterials*, vol. 11, p. 568, feb 2021.

[83] J. Xiao, W. Lv, Z. Xie, Y. Song, and Q. Zheng, "L-cysteine-reduced graphene oxide/poly(vinyl alcohol) ultralight aerogel as a broad-spectrum adsorbent for anionic and cationic dyes," *Journal of Materials Science*, vol. 52, pp. 5807–5821, jan 2017.

[84] M. Yan, Q. Liang, W. Wan, Q. Han, S. Tan, and M. Ding, "Amino acid-modified graphene oxide magnetic nanocomposite for the magnetic separation of proteins," *RSC Advances*, vol. 7, no. 48, pp. 30109–30117, 2017.

[85] G. Rambabu and S. D. Bhat, "Amino acid functionalized graphene oxide based nanocomposite membrane electrolytes for direct methanol fuel cells," *Journal of Membrane Science*, vol. 551, pp. 1–11, apr 2018.

[86] W. Qiao, L. Wang, B. Ye, G. Li, and J. Li, "Electrochemical behavior of palmatine and its sensitive determination based on an electrochemically reduced L-scp-methionine functionalized graphene oxide modified electrode," *The Analyst*, vol. 140, no. 23, pp. 7974–7983, 2015.

[87] K. Spyrou, M. Calvaresi, E. K. Diamanti, T. Tsoufis, D. Gournis, P. Rudolf, and F. Zerbetto, "Graphite oxide and aromatic amines: Size matters," *Advanced Functional Materials*, vol. 25, pp. 263–269, nov 2014.

[88] S. Mantovani, S. Khaliha, T. D. Marforio, A. Kovtun, L. Favaretto, F. Tunioli, A. Bianchi, G. Petrone, A. Liscio, V. Palermo, M. Calvaresi, M. L. Navacchia, and M. Melucci, "Facile high-yield synthesis and purification of lysine-modified

graphene oxide for enhanced drinking water purification," *Chemical Communications*, vol. 58, no. 70, pp. 9766–9769, 2022.

[89] S. Mantovani, T. D. Marforio, S. Khaliha, A. Pintus, A. Kovtun, F. Tunioli, L. Favaretto, A. Bianchi, M. L. Navacchia, V. Palermo, M. Calvaresi, and M. Melucci, "Amino acid-driven adsorption of emerging contaminants in water by modified graphene oxide nanosheets," *Environmental Science: Water Research and Technology*, vol. 9, no. 4, pp. 1030–1040, 2023.

[90] A. Artemenko, A. Shchukarev, P. Štenclová, T. Wågberg, J. Segervald, X. Jia, and A. Kromka, "Reference XPS spectra of amino acids," *IOP Conference Series: Materials Science and Engineering*, vol. 1050, p. 012001, jan 2021.

[91] J. Russat, "Characterization of polyamic acid/polyimide films in the nanometric thickness range from spin-deposited polyamic acid," *Surface and Interface Analysis*, vol. 11, pp. 414–420, may 1988.

[92] A. Liscio, K. Kouroupis-Agalou, X. D. Betriu, A. Kovtun, E. Treossi, N. M. Pugno, G. D. Luca, L. Giorgini, and V. Palermo, "Evolution of the size and shape of 2D nanosheets during ultrasonic fragmentation," *2D Materials*, vol. 4, p. 025017, feb 2017.

[93] D. Deng, K. S. Novoselov, Q. Fu, N. Zheng, Z. Tian, and X. Bao, "Catalysis with two-dimensional materials and their heterostructures," *Nature Nanotechnology*, vol. 11, pp. 218–230, mar 2016.

[94] L. Lombardi and M. Bandini, "Graphene oxide as a mediator in organic synthesis: a mechanistic focus," *Angewandte Chemie International Edition*, vol. 59, pp. 20767–20778, oct 2020.

[95] A. Jiříčková, O. Jankovský, Z. Sofer, and D. Sedmidubský, "Synthesis and applications of graphene oxide," *Materials*, vol. 15, p. 920, jan 2022.

[96] H. M. Lee, I. S. Youn, M. Saleh, J. W. Lee, and K. S. Kim, "Interactions of CO_2 with various functional molecules," *Physical Chemistry Chemical Physics*, vol. 17, no. 16, pp. 10925–10933, 2015.

[97] J. Ma, X. Zhang, N. Zhao, A. S. Al-Arifi, T. Aouak, Z. A. Al-Othman, F. Xiao, W. Wei, and Y. Sun, "Theoretical study of TBD-catalyzed carboxylation of propylene glycol with CO_2," *Journal of Molecular Catalysis A: Chemical*, vol. 315, pp. 76–81, jan 2010.

[98] S. Huang, J. Ma, J. Li, N. Zhao, W. Wei, and Y. Sun, "Efficient propylene carbonate synthesis from propylene glycol and carbon dioxide via organic bases," *Catalysis Communications*, vol. 9, pp. 276–280, feb 2008.

[99] C. yuan Cheng, H. Shen, N.-N. Shen, C. Castro, V. Dubovoy, D. Wu, R. Subramanyan, X.-Y. Huang, C. E. Pitsch, X. Wang, and L. Pan, "Carbon dioxide capture by amino acids through an arginine–arginine carbamate ion pair," *Industrial and Engineering Chemistry Research*, vol. 60, pp. 17745–17749, nov 2021.

[100] V. B. Saptal, T. Sasaki, K. Harada, D. Nishio-Hamane, and B. M. Bhanage, "Hybrid amine-functionalized graphene oxide as a robust bifunctional catalyst for atmospheric pressure fixation of carbon dioxide using cyclic carbonates," *ChemSusChem*, vol. 9, pp. 644–650, feb 2016.

[101] X. Zhang, K.-H. Chen, Z.-H. Zhou, and L.-N. He, "Reduced graphene oxide supported ag nanoparticles: An efficient catalyst for CO_2 conversion at ambient conditions," *ChemCatChem*, vol. 12, pp. 4825–4830, aug 2020.

[102] N. Hsan, P. K. Dutta, S. Kumar, and J. Koh, "Arginine containing chitosan-graphene oxide aerogels for highly efficient carbon capture and fixation," *Journal of CO_2 Utilization*, vol. 59, p. 101958, may 2022.

[103] S. Khabnadideh, E. Mirzaei, and L. Amiri-Zirtol, "L-arginine modified graphene oxide: A novel heterogeneous catalyst for synthesis of benzo[b]pyrans and pyrano[3,2-c]chromenes," *Journal of Molecular Structure*, vol. 1261, p. 132934, aug 2022.

[104] B. Wu, L. Zhang, B. Jiang, Q. Li, C. Tian, Y. Xie, W. Li, and H. Fu, "Ultrathin porous carbon nitride bundles with an adjustable energy band structure toward simultaneous solar photocatalytic water splitting and selective phenylcarbinol oxidation," *Angewandte Chemie International Edition*, vol. 60, pp. 4815–4822, jan 2021.

[105] S. Zhang, H. Zhang, F. Cao, Y. Ma, and Y. Qu, "Catalytic behavior of graphene oxides for converting CO_2 into cyclic carbonates at one atmospheric pressure," *ACS Sustainable Chemistry and Engineering*, vol. 6, pp. 4204–4211, feb 2018.

[106] S. Eigler, C. Dotzer, A. Hirsch, M. Enzelberger, and P. Müller, "Formation and decomposition of CO_2 intercalated graphene oxide," *Chemistry of Materials*, vol. 24, pp. 1276–1282, Mar. 2012.

[107] F. Z. Liu, H. Fang, and W. F. Xu, "An efficient way to coupling amine with derivatives of steric N-Boc-pyrrolidine-2-carboxylic acid," *Chinese Chemical Letters*, vol. 18, pp. 393–396, apr 2007.

[108] W.-H. Xie, X. Yao, H. Li, H.-R. Li, and L.-N. He, "Biomass-based N-rich porous carbon materials for CO_2 capture and in-situ conversion," *ChemSusChem*, vol. 15, aug 2022.

[109] A. Pintus, S. Mantovani, A. Kovtun, G. Bertuzzi, M. Melucci, and M. Bandini, "Recyclable GO-arginine hybrids for CO_2 fixation into cyclic carbonates," *Chemistry – A European Journal*, vol. 29, nov 2022.

[110] S. Mantovani, A. Pintus, A. Kovtun, A. Gondolini, S. Casadio, A. Sanson, T. D. Marforio, M. Calvaresi, M. Rancan, L. Armelao, G. Bertuzzi, M. Melucci, and M. Bandini, "Graphene oxide-arginine composites: Efficient dual function materials for integrated co2 capture and conversion," *ChemSusChem*, Jan. 2024.

[111] Y. Mao, X. Yang, and T. V. Gerven, "Amine-assisted simultaneous CO_2 absorption and mineral carbonation: Effect of different categories of amines," *Environmental Science and Technology*, vol. 57, pp. 10816–10827, jul 2023.

[112] P. P. Pescarmona, "Cyclic carbonates synthesised from CO_2: Applications, challenges and recent research trends," *Current Opinion in Green and Sustainable Chemistry*, vol. 29, p. 100457, jun 2021.

[113] L. B. Hamdy, C. Goel, J. A. Rudd, A. R. Barron, and E. Andreoli, "The application of amine-based materials for carbon capture and utilisation: an overarching view," *Materials Advances*, vol. 2, no. 18, p. 5843–5880, 2021.

[114] J. S. Stevens, A. C. de Luca, M. Pelendritis, G. Terenghi, S. Downes, and S. L. M. Schroeder, "Quantitative analysis of complex amino acids and rgd peptides by X-ray photoelectron spectroscopy (XPS)," *Surface and Interface Analysis*, vol. 45, pp. 1238–1246, apr 2013.

[115] G. Barbarella, M. Zambianchi, A. Ventola, E. Fabiano, F. D. Sala, G. Gigli, M. Anni, A. Bolognesi, L. Polito, M. Naldi, and M. Capobianco, "Bright oligothiophenen-succinimidyl esters for efficient fluorescent labeling of proteins and oligonucleotides," *Bioconjugate Chemistry*, vol. 17, no. 1, pp. 58–67, 2006.

[116] M. Melucci, E. Treossi, L. Ortolani, G. Giambastiani, V. Morandi, P. Klar, C. Casiraghi, P. Samorì, and V. Palermo, "Facile covalent functionalization of graphene oxide using microwaves: bottom-up development of functional graphitic materials," *Journal of Materials Chemistry*, vol. 20, no. 41, p. 9052, 2010.

[117] M. Muehlbacher and C. D. Poulter, "Regioselective opening of simple epoxides with diisopropylamine trihydrofluoride," *The Journal of Organic Chemistry*, vol. 53, pp. 1026–1030, Mar. 1988.

[118] S. Li, Y. Shi, P. Li, and J. Xu, "Nucleophilic organic base DABCO-mediated chemospecific meinwald rearrangement of terminal epoxides into methyl ketones," *The Journal of Organic Chemistry*, vol. 84, pp. 4443–4450, Feb. 2019.

[119] M. H. Dehghani, M. Ghadermazi, A. Bhatnagar, P. Sadighara, G. Jahed-Khaniki, B. Heibati, and G. McKay, "Adsorptive removal of endocrine disrupting bisphenol a from aqueous solution using chitosan," *Journal of Environmental Chemical Engineering*, vol. 4, pp. 2647–2655, sep 2016.

[120] W. Libbrecht, K. Vandaele, K. De Buysser, A. Verberckmoes, J. Thybaut, H. Poelman, J. De Clercq, and P. Van Der Voort, "Tuning the pore geometry of ordered mesoporous carbons for enhanced adsorption of bisphenol-a," *Materials*, vol. 8, p. 1652–1665, apr 2015.

[121] J. Xu, L. Wang, and Y. Zhu, "Decontamination of bisphenol a from aqueous solution by graphene adsorption," *Langmuir*, vol. 28, may, pages = 2012.

[122] A. Nezhadali, S. E. Koushali, and F. Divsar, "Synthesis of polypyrrole – chitosan magnetic nanocomposite for the removal of carbamazepine from wastewater: Adsorption isotherm and kinetic study," *Journal of Environmental Chemical Engineering*, vol. 9, p. 105648, Aug. 2021.

[123] D. A. Borisova, M. D. Vedenyapina, E. D. Strel'tsova, V. L. Maslov, K. H. Rosenwinkel, D. Weichgrebe, P. Stopp, and A. A. Vedenyapin, "Adsorption of carbamazepine from aqueous solutions on expanded graphite," *Solid Fuel Chemistry*, vol. 47, p. 298–302, Sept. 2013.

[124] X. Zhou, Y. Yang, C. Li, Z. Yang, W. Yang, Z. Tian, L. Zhang, and T. Tao, "Environmental-friendly one-step fabrication of tertiary amine-functionalized adsorption resins for removal of benzophenone-4 from water," *Journal of Cleaner Production*, vol. 203, p. 655–663, Dec. 2018.